Construction and Analysis of a Lightweight UAV Wing Prototype

Mário Hernâni Silva Ramos

Thesis to obtain the Master of Science Degree in

Aerospace Engineering

Supervisor: Prof. André Calado Marta

Examination Committee

Chairperson: Prof. Filipe Szolnoky Ramos Pinto Cunha
Supervisor: Prof. André Calado Marta
Member of the Committee: Prof. Virginia Isabel Monteiro Nabais Infante

November 2015

To my parents, for their unconditional support through every step of my life.

Acknowledgments

I would like to thank my thesis supervisor, professor André Calado Marta, for all the guidance and support.

I would also like to thank professors Virginia Infante and Zuzana Dimitrovová for giving me the opportunity to observe some test using the VIC software and letting me now as much as possible about it.

To professor Luís Reis, I would like the thank for all the help with the testing of the balsa and composite specimens.

Last but not least, I would like to sincerely thank my family and friends. Their presence and support throughout the good and the bad moments of my academic career was essential in helping me reach this point.

Resumo

O aumento na utilização de aeronaves não tripuladas nos últimos anos conduziu a um mercado mais competitivo, onde mais atenção tem vindo a ser dada à eficiência e segurança com as quais estas aeronaves completam os objectivos das suas missões. Tendo isso em conta, um maior foco tem sido colocado sobre a fase preliminar do seu design estrutural, onde as recentes evoluções a nível da análise computacional usando o método dos elementos finitos possibilitam uma melhor previsão do comportamento da estrutura final. Nesta tese, um protótipo de uma nova estrutura para a asa de um UAV de asa fixa é construído, e os resultados obtidos pelos testes nele feitos comparados com os do modelo numérico construído no CATIA®. Com vista a tal, um modelo CAD tanto da estrutura da asa como do protótipo foi concebido, com base em parâmetros de design identificados. Os materiais seleccionados para o protótipo são testados, as suas propriedades elásticas determinadas e uma validação desses testes efectuada no módulo de análise estrutural do CATIA®. O processo de produção do protótipo é descrito, sendo feitas considerações relativamente à influência de cada peça e material no peso final da estrutura. Os testes feitos no protótipo são apresentados, e uma comparação feita entre os seus resultados e os da análise por elementos finitos, seguida de uma discussão das diferenças entre eles. Conclusões sobre a precisão do modelo numérico obtido são feitas, e sugestões para minimizar as discrepâncias identificadas recorrendo a um processo de produção mais controlado são apresentadas. Este trabalho tem como objectivo estabelecer uma base para futuras geometrias computacionais de UAVS, usando as ferramentas de análise por elementos finitos aqui afinadas.

Palavras-chave: Método de elementos finitos, Propriedades dos materiais, Teste de materiais, Validação, Protótipo, Análise estrutural.

Abstract

An increase in the usage of Unmanned Aerial Vehicles (UAV) in the last couple of years has led to a more competitive market where more attention is being given to the efficiency and safety with which those aircraft accomplish their mission goals. Bearing that in mind, a greater focus is put on their preliminary structural design, where the development of computational Finite Element Analysis (FEA) methods allow for a better prediction of the behavior of the final structure. In this thesis, a prototype based on a new, suggested wing structure for a particular fixed wing UAV is built, and the results obtained by the experimental tests carried out on it compared to those yielded by a numerical model developed in CATIA®. To do so, a CAD model of both the suggested wing structure and its prototype is created, based on identified design parameters. The materials selected for the prototype are tested, their elastic properties determined and a validation of those tests made in CATIA®'s Generative Structural Analysis workbench. The building process of the prototype is described, and considerations regarding the influence of each material and part in its final weight are made. The tests performed on the prototype are presented, and a comparison between their results and those of the FEA is made, followed by a discussion of the differences between them. Conclusions on the accuracy of the numerical model are drawn, and suggestions of ways to minimize those discrepancies by means of a more controlled building process are presented. This effort is aimed to pave the way for future higher-fidelity computational structural designs of UAVs using the tuned FEA tools.

x

Contents

List of Tables

List of Figures

Nomenclature

Greek symbols

α Angle of attack.

ϵ Strain.

ν Poisson's coefficient.

ρ Density.

σ Stress.

θ Fiber orientation angle.

Roman symbols

$(t/c)_{max}$ Maximum thickness to chord ratio

A Area.

B_{cp} Circular boom chordwise position.

BF_l Bottom flange length.

BF_t Bottom flange thickness.

C Stiffness tensor.

C_D Coefficient of drag.

C_L Coefficient of lift.

C_M Coefficient of moment.

C_p Pressure coefficient.

c_r Root chord.

c_t Tip chord.

d_i Circular boom inner diameter.

d_o Circular boom outer diameter.

E Young's Modulus.

F Force.

G Shear Modulus.

I Area moment of inertia.

iW Incidence angle of the wing.

l Length.

Ma Mach number

P Applied load.

R Transformation matrix.

r_h Rib hollowness.

r_s Rib spacing.

r_t Rib thickness.

S Compliance coefficients matrix.

S_{cp} Spar chordwise position.

TF_l Top flange length.

TF_t Top flange thickness.

v Volume percentages.

W_l Web length.

W_t Web thickness.

W_w Wing structural weight

p Pressure.

$\mathbf{u}$ Velocity vector.

u, v, w Velocity Cartesian components.

Subscripts

f Composite fiber.

i, j, k Computational indexes.

m Composite matrix.

n Normal component.

x, y, z Cartesian components.

Superscripts

0   Initial state.

T   Transpose.

Glossary

CAD   Computer Aided Design consists of the usage of computers in modeling and modifying parts.

CFD   Computational Fluid Dynamics is a branch of fluid mechanics that uses numerical methods and algorithms to solve problems that involve fluid flows.

CSM   Computational Structural Mechanics is a branch of structure mechanics that uses numerical methods and algorithms to perform the analysis of structures and its components.

FEA   Finite Element Analysis is a branch of solid mechanics that uses the Finite Element Method to perform structural analysis on a variety of structures.

FEM   Finite Element Method is a numerical technique used to find approximate solutions to boundary values problems, based on the subdivision of a domain ins smaller, simpler parts called finite elements.

GSA   Generative Structural Analysis is a workbench present in CATIA® that allows for a FEA of the modeled parts or assemblies, using a variety of finite elements and connection properties.

LEEUAV   Long Endurance Electric Unmanned Aerial Vehicle.

MDO   Multi-Disciplinar Optimization is an engineering technique that uses optimization methods to solve design problems incorporating two or more disciplines.

UAV   Unmanned Aerial Vehicle.

VIC   Virtual Image Capture and recognition software used to determine the deformation of a specimen based on the analysis of dots painted on its surface.

Chapter 1

Introduction

1.1 Motivation

Nowadays, we are witnessing an increase in the usage of Unmanned Aerial Vehicles (UAVs), also known as drones or Remotely Piloted Aircraft Systems (RPAS) not only for the more traditional military operations, but also for civilian purposes. As a matter of fact, UAVs have been used by civilians in a wide variety of missions, such as forest fire detection, 3D mapping of landscapes and even to provide assistance during search and rescue missions.

Given this growth in the market for UAVs, it is of a great importance to be able to design and build vehicles that are suited for the mission at hand, being able to complete such mission in the safest and most efficient manner possible. As such, it is necessary to consider all factors that influence the performance of the UAV as early in the design process as possible. Propulsion systems, energy sources and aerodynamics are some of those factors. However, the structure of the UAV will play an extremely important role on how the complete product will be able to perform its mission.

The significant evolution of computers over the last few decades has allowed for an easier design of such structures. Existing commercial structural analysis software packages using Finite Element Methods (FEM) give the opportunity for the designers to simulate the behavior of the structures designed under given loading cases, providing a useful tool to predict how said structures will react to such loading scenarios, even before a physical prototype is built. It is, however, very important for the designers to be mindful of the limitations of this type of software, and know how to overcome them, in order to obtain a model as faithful as possible to its future real life counterpart.

Using such tools and following an optimization process, it is possible to design lighter, more resistant structures than ever before, thus contributing to the overall goal of producing efficient UAVs that can meet the requirements of the growing market.

1.2   Objectives

This thesis is focused on obtaining a numerical model that can be put to use in a preliminary design phase of a new wing structure for a Long Endurance Electric UAV (LEEUAV) for civilian surveillance missions. The UAV has been developed as a product of the LEEUAV project [1], and already has a fully functional wing. This new structure should be based in that existing one, with slight modifications that may allow for a better behavior and reduced weight. A prototype of that structure will be built, and static tests performed on it. The obtained results will then be compared with those yielded by the numerical model of that prototype, and conclusions regarding its accuracy will be drawn.

Special attention will be paid to the characterization of the materials used on the wing. These materials will be tested and their properties determined prior to the structural analysis of the prototype. A fine tuning of the numerical model will be performed based on a validation of those properties using the same FEM software that will be used to perform the structural analysis,in order to obtain a numerical model that is as faithful to reality as possible.

1.3   Thesis Outline

In chapter 2, a few remarks will be made concerning the existing UAV, its main characteristics and goals will be identified, together with the aerodynamic loads to which it will be subjected. The existing wing will be presented and a general wing design process will be discussed.

In chapter 3, a CAD model of the wing will be produced. At this point, an identification of the parameters involved in the design of the wing will be carried out. Doing so allows for the CAD model to be modified at later occasions with greater ease. A selection of the software package used for this process will be done, presenting the advantages and disadvantages of the several considered options.

A general discussion about structural analysis using the Finite Elements Method will then take place in chapter 4, and a brief description of such method will be carried out. The constitutive laws of the different types of materials will also be presented, and a validation for a simple case will be carried out in order to assess the capabilities of the FEM software

At this point, a materials study will be carried out in chapter 5. The materials that are to be used in the wing will be tested and its elastic properties determined so that they can be applied to the model created on the software. The recommended test procedures will be described according to the international standards, when available, followed by a discussion of the actual tests and their results.

A validation of these tests will then be performed in chapter 6. The test procedures will be modeled in the chosen FEM software using the properties determined in the actual tests, and their results presented. If it is necessary, the material properties will be tuned, in order to obtain a numerical model for each material that accurately represents their real behavior.

Having performed this validation, the new wing design will be presented in chapter 7. A choice between the different structure configurations will be made, and the final wing presented, along with its CAD model.

It will then be described, in chapter 8 the process of building the prototype for the chosen wing, followed by several testing procedures. The results obtained will then be compared with the ones from the FEM analysis carried out on the chosen wing and an attempt at validating them will be made in chapter 9.

Finally, conclusions will be drawn and suggestions to eventual future work will be made in chapter 10.

Chapter 2

Background

In this chapter, a presentation of the required elements for the the completion of future tasks will be made. The general UAV characteristics will be presented, followed by a deeper look into the aerodynamic performance of the current wing. Some wing structure design topics will also be presented, as a foundation for what is to come later on.

2.1   General UAV Characteristics

In this section, the main characteristics of the UAV developed as a result of the LEEUAV project [1] will be presented.

The main specifications that drove the design of the UAV were long endurance, usage of green power sources, ability to fly autonomously and usage of a high-strength and lightweight structure, built with composite materials. The UAV should also be capable of performing different type of missions.

The LEEUAV mission was then defined. Its profile consists of a very short takeoff distance, which should happen in 8 meters for the case of an autonomous takeoff or in 3 meters in case of it being hand launched. The UAV should then climb to its cruise altitude of 1000 meters in 10 minutes, where it should fly for 8 hours at a speed to be determined according to the system efficiency, but above a threshold of 7 m/s. Following the cruise section of its mission, the UAV should be able to descend without power for 29 minutes and land in the field. The desired performance parameters are presented in Table 2.1

Cruise speed [m/s]	7.5
Maximum climb rate [m/s]	2.2
Lift-to-drag ratio	20
Maximum speed [m/s]	21.1
Stall speed [m/s]	6.1
Takeoff roll distance [m]	8.1

Table 2.1: Desired UAV performance.

A conventional wing and fuselage configuration proved to be the best choice, so as to allow for the installation of the avionics.

Regarding the aerodynamics of the wing, a more in-depth exposition of the reasoning behind the choices made during the design of the UAV will be later on presented. For now, however, it is relevant to say that a new airfoil was designed in order to meet the requirements set for the UAV. The wing built was comprised of three different sections, with a 13.5 aspect ratio, 4.50 m span and a total wing area of 1.518 m^2. Figure 2.1 shows the current LEEUAV CAD and the final aircraft in flight.

(a) LEEUAV CAD.
(b) LEEUAV in flight.

Figure 2.1: Current LEEUAV.

As far as the propulsion system is concerned, in order to satisfy the need for a long endurance with the usage of green energy, a hybrid system comprised of batteries and solar panels was chosen to power an electric motor.

Since a crucial part of the propulsion system is the number and type of solar panels used, a study on the required power for the UAV to perform each of the mission sections was carried out. Based on the results, the batteries and solar panels were chosen. These solar panels were to be mounted on the upper surface of the wing. The photo-voltaic cells chosen were mono-crystalline, being the best in terms of efficiency, flexibility and weight. Based on the wing size determined at an earlier stage, a total of 44 photo-voltaic cells were installed, 22 per wing.

It was also shown, based on the solar irradiation levels measured in the area of Covilhã, where the UAV was designed to operate, that during the summer months, the power provided by the solar cells during the cruise segment of the mission exceeded the power required for that segment. This meant that the batteries had to be pre-charged to allow for the take-off and climbing phases of the mission profile, being charged afterwards, in flight, during the cruise phase. However, during the winter months, where the solar irradiation is largely reduced, it was shown that the batteries would hardly recharge during flight, which means that a significantly larger battery would be required.

With concern to the communication and electronic systems, it was necessary to implement a system capable of allowing the UAV to fly autonomously or by remote pilot. In order to satisfy that last requirement, a first person view system was installed, consisting of a ground control station including a LCD screen, a digital video recorder, batteries and a power module, and several airborne components. These include a camera and a microphone, as well as an On-Screen Display, responsible for including all the relevant telemetry data on the video signal that is later broadcast by an antenna. The antennas used are circular polarized, so as to minimize multipath interference.

An open source autopilot system was implemented. This system includes several internal sensors, such as 3-axis gyros, 3-axis accelerometers, a magnetometer, a GPS system and a barometric pressure sensor.

The main LEEUAV characteristics may be found in Table 2.2.

Span [m]	4.500	Tailplane span [m]	0.850
Length [m]	2.370	Tailplane area [m^2]	0.181
Root wing chord [m]	0.350	Root empenage chord [m]	0.258
Tip wing chord [m]	0.250	Tip empenage chord [m]	0.364
Wing area [m^2]	1.518	Empenage area [m^2]	0.077
Aspect ratio	13.500	Structure mass [Kg]	1.590
Tailplane chord [m]	0.213	Empty mass [Kg]	3.890
		Takeoff mass [Kg]	4.900

Table 2.2: Main LEEUAV characteristics.

2.2   Aerodynamic Loads

In order to develop a wing structure that differs from the one already installed in the UAV, it is necessary to be aware not only of the general UAV characteristics, previously presented, but also of the existing wing and its characteristics. Its aerodynamic performance needs to be known and the aerodynamic loads it is subjected to determined.

In the present section, an overview of the work carried out in [2] will be made, paying close attention to the aerodynamic analysis carried out on the UAV wing.

2.2.1   CAD Model

Firstly, in order to perform an aerodynamic analysis using computer software, a CAD model of the UAV had to be obtained. As such, after considerations regarding the several pros and cons of different CAD programs, FreeCAD$^{®}$ [3] was chosen. This choice was based on the need for the program to support Windows and Linux operating systems, as well as scripting, since it was desired to minimize the interaction between software and designer. This software package also allows to export the CAD design into files of a format that can be used by the CFD program.

The UAV CAD design phase using FreeCAD$^{®}$ was then carried out in several stages. Firstly, the user would input the geometric parameters, which were then checked for errors or incongruities as far as sizes of the aircraft were concerned. Should this evaluation be successful, the different components of the UAV were then built, considering 4 different sections. Firstly, the wing was built, followed by the fuselage, tail and nose. Since the scope of this thesis is the main wing, further description on how it was designed will follow. In [2], it is explained that the left half wing was first built. It is also stated that the wing is defined by four sections, with a specified airfoil at each of them, as well as specific chord, sweep, twist and dihedral values. All sections are positioned taking into account the first section.

The different sections can be viewed in Figure 2.2. Since this is the left half wing, Section S0 is the one located at the fuselage plane of symmetry, with an airfoil chord of 350 mm. Section S1 is located at the end of the fuselage. As such, the distance between sections S0 and S1 was determined by the

7
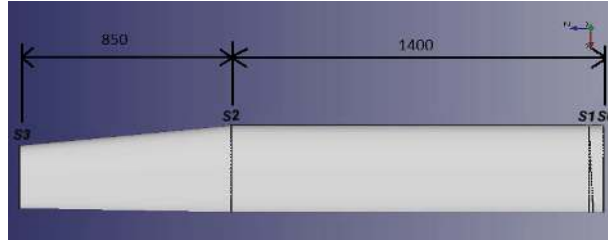
Figure 2.2: Wing and its different sections.

half width of the fuselage. The airfoil chord remains constant up until S2. Section S3 is located at the wing tip, with a chord of 252 mm. Between these last two sections, a sweep angle of 5.5º is present. The wing incidence is of -5º considering a positive rotation along axis *Oz*, and -1º dihedral considering a positive rotation along *Ox*.

The other parts of the UAV were then modeled, and finally assembled. In order to prepare the CAD model for the CFD analysis, several control volumes were also defined.

2.2.2 CFD Analysis

For the CFD analysis, Star-CCM+® [4] was chosen due to the fact of it being regarded as one of the best flow simulation and mesh generator software packages available.

In order to determine which aerodynamic models were to be used, a validation study was carried out. *k-ω* SST turbulence model [5], together with $\gamma - Re_\theta$ transition model [6] was one of the considered models, as well as the Spalart-Allmaras turbulence model [7], [8].

The validation study was carried out in 2D, considering the MA409 and the CAL1215J airfoils, for which [2] found relevant data for tests in low-turbulence subsonic wind-tunnel. As far as the mesh is concerned, a prismatic layer was employed along the airfoils, and a polyhedral mesh in the rest of the domain.

Several analyses were performed, considering Reynolds number values of 2×10^5 and 3×10^5, for a range of angles of attack. For each value of Re and angle of attack, analysis were conducted considering the *k-ω* SST turbulence model, together with $\gamma - Re_\theta$ transition model, and the Spalart-Allmaras turbulence models.

The behavior of the lift and drag coefficients with the variation of angle of attack was checked for both values of Re. It was shown that the Spalart-Allmaras turbulence model did not perform well when predicting the drag coefficient, even though it converged faster than the *k-ω* SST turbulence model. This latter turbulence model, together with the $\gamma - Re_\theta$ transition model, predicted accurately the aerodynamic coefficients, as well as the location at which natural transition occurred. As such, [2] found this model the best to use when performing aerodynamic analysis on the UAV wing.

The aerodynamic performance of the UAV was then determined. Using the control volumes previously defined during the CAD modeling of the UAV, several meshes were created, with different number of cells, by refining different control volumes. A mesh was then chosen, based on the results of analysis

carried out for the UAV flying at an angle of attack of 0º. A mesh with 7 million cells was chosen, as the author found it to be the best compromise between computational cost and accuracy of the results.

The aerodynamic performance parameters of the UAV determined in [2] are presented on Table 2.3

Maximum lift coefficient	$C_{L_{max}}$	1.51
Maximum lift angle of attack	$\alpha_{C_{L_{max}}}$	8º
Zero lift angle of attack	α_{0lift}	-9.5º
Lift VS angle of attack curve slope	C_{L_α}	$5.59rad^{-1}$
Minimum drag coefficient	$C_{D_{min}}$	0.0527
Zero lift drag coefficient	$C_{D,0}$	0.06
Maximum lift-to-drag ratio	$(C_L/C_D)_{max}$	14.01
Angle of attack of maximum lift-to-drag ratio	$\alpha_{C_L/C_D)_{max}}$	0º
Maximum lift$^{3/2}$-to-drag ratio	$(C_L^{3/2}/C_D)_{max}$	15.06
Angle of attack of maximum lift$^{3/2}$-to-drag ratio	$\alpha_{(C_L^{3/2}/C_D)_{max}}$	2º

Table 2.3: UAV performance parameters.

In order to properly estimate the aerodynamic forces acting on the LEEUAV wing, the analysis obtained in [2] was used. The reference values considered when calculating the aerodynamic coefficients are summarized in Table 2.4.

Reference density	1.184 Kg/m^3
Reference pressure	0 Pa
Reference velocity	7.48 m/s
Reference area	0.781 m^2

Table 2.4: Reference values used in CFD analysis.

Performing a post processing operation on the analysis results, the pressure distribution along the wing was obtained in two different manners. Since it would be impossible to process that data in the totality of the wing, in a continuous manner, both along the span and the chord, a discrete approach was taken along one of these dimensions. This way, it is possible to consider the continuous distribution of the pressure along either the chord or the span, even though only at discrete points on the other dimension.

In a first approach, several derived parts were defined at different points along the wingspan. These parts consisted of 2 cm wide slices of the wing surface, where the pressure coefficient was measured. A total of thirteen of these parts were created, and the chordwise pressure coefficient distribution obtained. The spacing between these sections was gradually decreasing, from the wing root to the tip, as it is expected that the pressure coefficient will vary more near the wing tip.

In a second approach, a total of eight derived parts similar to the previously described, also 2 cm wide, were defined at different points of the wing chord, allowing for a continuous measurement of the pressure coefficient along the span. These were homogeneously spaced.

Both approaches are schematically presented in Figure 2.3

It is worth noting that the width of the derived parts was chosen to be 2 cm due to a compromise between the accuracy of the data obtained and the time required to process such data. Since the mesh is not structured, the best way to obtain data in specific locations was to define the previously referred

(a) First approach.   (b) Second approach.

Figure 2.3: Approaches used for the estimation of the aerodynamic loads.

derived parts, which consist of the cells whose centroids are confined in a user defined interval. If this interval is too large, one would obtain data measured in a large number of cells, and a dispersion of values would be expected, since some cells would be separated by long distances. This would lead to difficulties processing the data, not only because of the high number of points to be considered, but also because of the dispersion of the values, which would make it difficult to find a good fit. However, if too thin of an interval is defined, one may lose continuity of data along the direction where it was wanted to be continuous, due to the non structured nature of the mesh. As such, a compromise had to be made, and the 2 cm interval was chosen.

The data was then exported from Star-CCM+® and imported into a spreadsheet table with the layout of Table 2.5, where it was processed. It is worth noting that the number of lines, n, varies along the several spanwise or chordwise positions (depending on which of these coordinates is being taken as discrete) at which data is gathered, since the number of elements along the chord (or span) is not constant.

Since Star-CCM+® does not separate upper and lower surface points, they had to be sorted, in order to be plotted as two different data series. This was achieved by sorting the values of the pressure coefficient along the profile from smaller to larger. By doing so, all negative pressure coefficients surface to the top of the table, while the positive values go to the bottom. Knowing that the negative pressure coefficient points are located at the upper surface of the wing, it is possible to split the previously obtained table in two, one for the upper and other for the lower surface. At this point, the data in each of the two tables, whose layout is identical to the one presented in Table 2.5, is sorted again, this time with respect to the chordwise coordinate, from leading to trailing edge.

Chordwise coordinate	Pressure coefficient
x_1	C_{p1}
x_2	C_{p2}
x_3	C_{p3}
...	...
x_n	C_{pn}

Table 2.5: Layout of the spreadsheet table.

Using the data from those tables, it is possible to plot the pressure coefficient distribution along the wing. Figure 2.4 shows a plot of the pressure coefficient data for a slice between 1.1 and 1.2 m along the chordwise position. It is worth noting that, since the CFD simulation includes the entire LEEUAV

model, when extracting the data relative to the wing it does not start at the origin point, but at 349 mm.
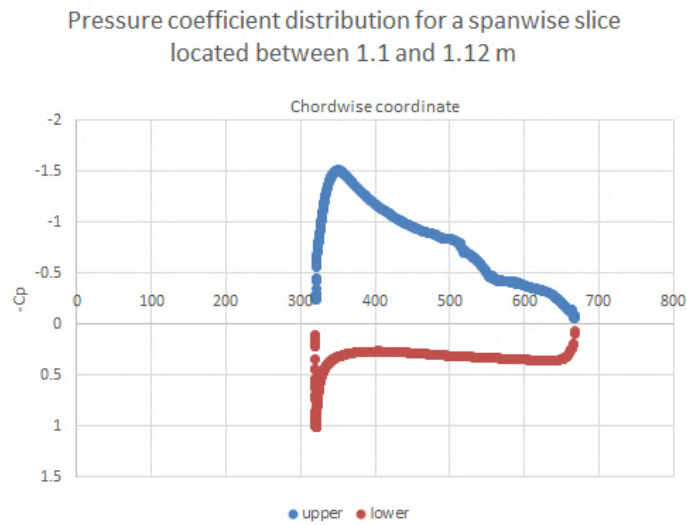
Figure 2.4: Pressure coefficient distribution for a chordwise slice between 1.1 and 1.12 m.

The pressure coefficient distribution obtained in slices along the chord was also plotted. Figure 2.5 shows the obtained plot for data gathered in a spanwise slice between the chordwise coordinates of 0.45 and 0.47 m.
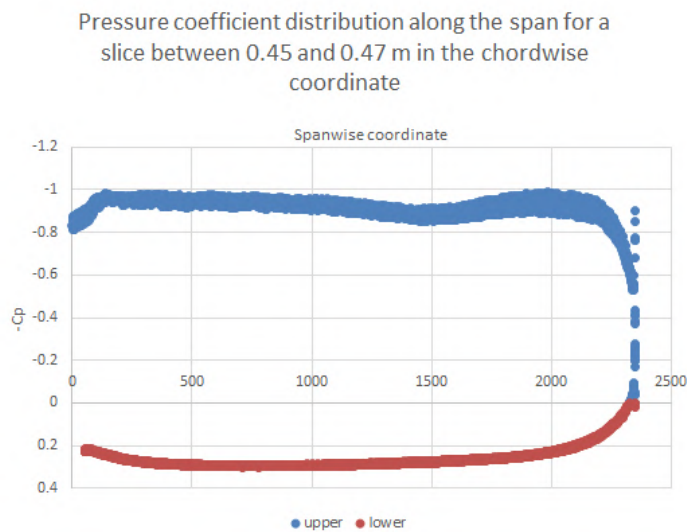
Figure 2.5: Pressure coefficient distribution for a spanwise slice between 0.45 and 0.47 m.

The pressure coefficient distributions determined will be used to calculate local forces that are to be applied on structural model in order to perform the FEA.

2.3 Existing Wing Structure

Taking into account the design goals of the UAV, stated in Section 2.1, a need for a lightweight structure is of the utmost importance. As such, the chosen materials were mainly wood and composites.

A D-box type structure was chosen for the wing. This box consists of two pultruded carbon spar caps and a 0.15 mm thick carbon fiber reinforce plastic (CFRP) skin, wrapped around a low density foam core. Plywood was used to build the strong aft ribs, while the light ones were built using balsa wood, as well as the trailing edge stringer. This type of structure was chosen as an alternative to a non-sheeted rib and spar construction, since it was considered to provide a higher torsional and bending stiffness, despite of its slightly higher weight. These structural features can be seen in Figure 2.6 (a).

(a) Current wing structure.

(b) Outer panel of the wing, with its CFRP connection tubes.
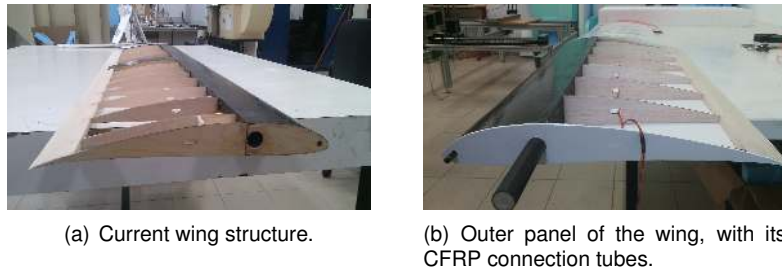
Figure 2.6: Current wing features.

The entire wing is covered by a thin sheet of heat-shrinking material, which gives the wing its final shape. The solar cells are placed on top of it.

This wing is divided into three different sections, and can be disassembled for transportation, one central panel with 12 solar cells and two outer panels, consisting of a rectangular zone containing the remainder of the solar cells and the taperd zone of the wing, where the ailerons are placed. Two CFRP tubes are responsible for the transfer of bending moments from the outer panels to the central panel of the wing. These tubes are attached to the spar by means of two plywood ribs and have different diameters, so that those in the outer panels fit into the central panel one. In Figure 2.6 (a) it is possible to see the hole of the tube, placed inside the D-box, where the tube that can be seen in Figure 2.6 (b) will fit.

2.4 Wing Design

At this point, it is relevant to present a general discussion of a preliminary wing design process. The fundamentals of this process remain unchanged despite the type of aircraft being considered, being it a commercial jet or a UAV. As such, this presentation will be as general as possible.

Several types of wing structures used in aircraft models will also be presented, as a reference for the new wing that will be modeled.

2.4.1 Wing Design Process

When designing a new wing for an aircraft, one first needs to take into account the aerodynamic aspects of the wing. The structural design of the wing comes afterwards.

As such, the first step to be taken in a wing design process is to select an airfoil which satisfies the needs of the aircraft, as far as its mission profile is concerned. This choice will determine the maximum

lift coefficient ($C_{l_{max}}$) that can be achieved. Several factors must be taken into account at this stage, such as the leading edge radius and the maximum thickness to chord ratio $(t/c)_{max}$. As it is shown in [9], there is an optimal value for $(t/c)_{max}$ of approximately 14%, based on data gathered from the most commonly used airfoils. The choice of $(t/c)_{max}$ will also be of extreme importance from a structural point of view, since the thickness of the airfoil will determine how thick the wing will be, which has an impact on how it behaves. The thicker the wing, the bigger its bending stiffness, which allows for the structural elements of the wing to be made lighter. It is presented in [9] that, based on historical data, the structural weight of the wing varies according to

$$W_W \propto (t/c)_{max}^{0.5}.$$
(2.1)

When selecting or designing an airfoil, camber also needs to be considered. It determines the curvature of the airfoil, and adding it shifts the zero lift angle of attack to negative values, which means that the airfoil will be capable of producing lift, even at an angle of attack of 0º. Adding camber also forces the value of minimum drag to occur at positive angles of attack.

After the selection of the airfoil, taking into account all the previously presented factors, the three dimensional aspects of the wing are considered. A planform is chosen, with a given Aspect Ratio. An high aspect ratio will positively impact the performance of the wing. However, high aspect ratio wings bring several structural problems, because of their significant span. Aeroelastic considerations must be taken into account in greater detail when designing high aspect ratio wings.

The wing sweep angle also needs to be selected. This is particularly important for wings flying at transonic Mach numbers and above, since it reduces the effective Mach number measured at the leading edge, at the cost of a reduction of the lift produced. According to historical data presented in [9] it can be seen that the addition of sweep is only considered for wings flying above $Ma = 0.4$.

After all these selections are made, the 3D lift coefficient and the wing drag are estimated. The entire process is iterative, and if these estimates aren't according to the expected results, new iterations can be performed.

Having taken all the steps mentioned before, it is then possible to design the structure of the wing. This structural design process begins by estimating the loads which the wing will sustain, taking into account the load factors felt during the different stages of the aircraft's mission. These are represented in a V-n diagram [10], a graphical representation of the load factors as a function of the speed. A design load factor is then calculated by multiplying the load factor limit represented on the V-n diagram by a safety factor (sf), according to

$$n_{design} = sf \cdot n_{limit}.$$
(2.2)

After the design load factor is determined, the distributed loads along the wing are determined.

As far as the lift is concerned, based on the data obtained from the aerodynamic and initial sizing of the wing considerations previously presented, it is possible to obtain different approximations for its spanwise distribution. Considering an elliptic planform, it is possible to obtain the elliptic spanwise lift

distribution,

$$L^E(y) = \frac{4L}{\pi b} \sqrt{1 - \left(\frac{2y}{b}\right)^2},$$ (2.3)

where L represents the overall lift, b the wing span and y the spanwise coordinate, measured from the wing root to the wing tip.

Based on this distribution, an empirical method for the determination of the spanwise lift distribution for a generic trapezoidal planform untwisted wing was developed by [11], claiming that it is determined by the average between the elliptic and the trapezoidal lift distributions, being the latter given by

$$L^T(y) = \frac{2L}{b(1+\lambda)} \left[1 - \frac{2y}{b}(1-\lambda)\right].$$ (2.4)

Calculating the average of both lift distributions presented in Equations (2.3) and (2.4) provides a good estimate of the actual spanwise lift distribution for wings with reduced sweep.

After this step, the other forces acting on the wing are estimated. The wing weight and fuel and engine weight (when the fuel tanks and the engines are placed on the wing) are examples of forces considered at this stage.

Knowing all these forces, it is possible to perform a preliminary shear force and bending moment analysis, considering the wing to be a cantilever beam, supported at the wing root. Usually, plots of the spanwise distribution of the shear force and bending moment are obtained, allowing for an identification of the points along the wing where it will be subjected to greater stresses.

The remaining process consists on the actual design of the internal structure. This is dependent on the type of aircraft under consideration, since different types of structural designs exist with different advantages and disadvantages. Some of the wing structures used in projects similar to the LEEUAV will now be presented.

2.4.2 Types of Wing Structures Used in Aircraft Models

Since the LEEUAV is fundamentally an aircraft model, it is relevant to know the types of wing structures usually used in that type of aircraft. Depending on the model being built and on the resources available, as well as the skill level of the builder, it is possible to obtain different types of structures, each of them with its unique features, advantages and disadvantages. It is then relevant to understand the positive and negative aspects of each of those structures.

One of the simplest types of wing structure is the non-sheeted rib and spar construction, which can be observed in Figure 2.7. It simply consists of a spar, with ribs whose shape is identical to the airfoil. Most of the structure itself is hollow, which makes for an incredibly lightweight wing. The final shape of the wing will be given by the covering, which usually consists of an heat-shrinking plastic material. This covering will contribute for an increase of the wing stiffness, but it must be applied carefully in order not to cause the structure to warp. However, due to the previously presented structural features, this is an extremely flexible wing, incapable of sustaining high aerodynamic loads.

Another type of wing structure frequently used in aircraft models is the semi-sheeted wing, which
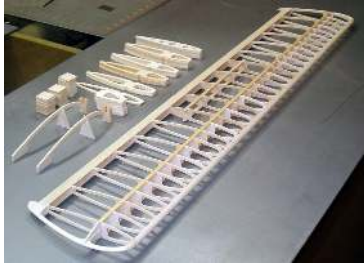
Figure 2.7: Non-sheeted rib and spar construction [12].
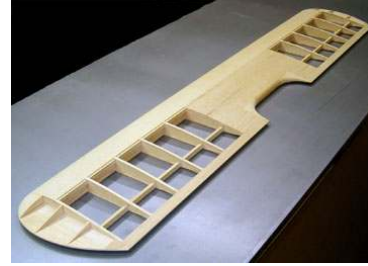
Figure 2.8: D-box semi-sheeted wing [12].

differs from the previously presented group in the fact that it possesses a sheeted section, with the shape of the airfoil. The non-sheeted section once again consists of ribs whose shape matches the airfoil's. The D-box wing structure (the one used in the wing described in Section 2.3) is an example of a semi-sheeted wing. It is sheeted from the main spar to the leading edge, providing the D shape that names it. The ribs have to be cut taking into account the thickness of the covering which will be applied, so that there is no discontinuity between the sheeted and non-sheeted section. This type of wing structure is shown in Figure 2.8. The inside of the sheeted area, the D-box, can be either hollow or filled with some sort of material, such as foam. This wing structure is naturally heavier than the non-sheeted rib and spar construction, but the added stiffness allows the wing to support higher loads. It also allows for a better transfer of forces to the fuselage, due to the increased support provided by the sheeted section.

A type of structure also to be considered is the fully-sheeted wing. This type of wings may have a regular rib and spar inner structure, or a foam core. It is a difficult wing to build, which requires great skill from the builders. It is also heavier than both previous structures, specially if a foam core is used, and it does not bring significant improvements to the wing behavior in flight, since its stiffness is not greatly altered. An example of a fully-sheeted wing can be seen in Figure 2.9.

Figure 2.9: Fully-sheeted wing [13].

Figure 2.10: Jedelsky wing [14].

Jedelsky wings are another type of structure frequently used in aircraft models. It is suitable for gliders, due to its characteristics. This wing structure is obtained by joining two sheets of balsa wood, foam, or other chosen material with a given angle. The upper surface of the wing is made of one of those sheets, and it is shaped as the upper surface of the airfoil. Figure 2.10 shows an example of a Jedelsky wing. The two different surfaces are observable, with the leading edge connected to the bottom side of the upper plate. This type of wing structure, although very light, is very flexible, and is not able to sustain more severe aerodynamic loads. It is for this reasons that it is essentially used in gliders, as previously

stated.

These are the main wing structures used in aircraft modeling. Sometimes, combinations of some of the previously presented structures are used, giving birth to hybrid wing structures, whose characteristics carry a bit of each of the main types of structures merged together.

Chapter 3

Wing Model

In this chapter, the process behind the creation of the CAD model of the wing will be described. This description will be as independent from a specific wing structure design as possible. A parametric definition of the main wing will be carried out, capturing the main parameters of the wing design, and thus allowing a parametric modeling process which makes it easier for quick changes to be made whenever necessary.

3.1   Identification of Design Parameters

As previously stated, a parametric approach to the design is extremely important, since throughout the project, several changes will be made to the structure. A parametric design process allows for a swift adjustment of the CAD model, without the need to start the whole process over and over again.

To address this issue, firstly the main design parameters must be identified. One must then consider the structural designs that will be employed, so as to understand which features to consider.

Since the scope of this project is the development of a numerical model of prototype of new wing structure that may eventually replace the existing LEEUAV wing, it is important that the aerodynamic properties of the existing wing are kept. As such, it is relevant to point out that the airfoil used in the CAD models will be the one developed for the LEEUAV in [1], being the overall wing configuration of the existing wing kept. This means that the wingspan, chord, and other geometric features of the wing presented in Table 2.2 will be used. These values are key parameters of the wing, even though they will not be changed during the CAD modeling process.

By looking at the different types of structures considered in Sections 2.3 and 2.4, one may identify that they share several common features. With the exception of the Jedelsky wing, it can be seen that both the sheeted and semi-sheeted wing structures, as well as the existing one, possess ribs along its span. These structural features are very important for the considered structural designs, and as such they will always be present. However, the number of ribs may vary, and, consequently, the spacing between them. As such, the distance between ribs, r_s, may be one of the considered parameters, and will define the number of ribs along the spanwise direction.

17

Regarding the ribs, their shape is the one of the airfoil, since these structural elements define the shape of the wing. However, some cut outs may be implemented, not only to allow for the passage of cables necessary for control systems, but also to reduce the overall weight of the wing. A parameter can be defined regarding the overall internal area of the rib that is going to be cut, r_h. Also, the thickness of the rib, r_t is yet another parameter to be considered.

Another structural feature common to the previously presented types of wing structures, once again with the exception of the Jedelsky wing, is the spar. In fact, this is the core feature of both the sheeted and semi-sheeted structures, consisting of a beam, with a selected cross section. Based on the selected cross-section, several different parameters may be identified (figure 3.1), and those will define the size of the beam.
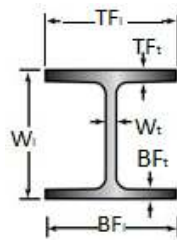
Figure 3.1: Spar cross section parameters.

By assigning values to these cross section parameters, it is possible to manipulate the length and thickness of both the flanges and the web, as illustrated in Figure 3.1. This method also accounts for the creation of a simple rectangular cross-section beam, if the value assigned to the flange length parameter is the same as the one attributed to the web thickness. It is also possible to obtain a T shaped cross section, if different parameters are defined for the upper and lower flange.

As for the placement of the spar with respect to the chord, a parameter S_{cp} representing the distance between the leading edge and the place where the spar is located will be defined.

Regarding the circular boom, parameters were defined for its outer, d_o, and inner d_i, diameters, as well as for its chordwise position, B_{cp}.

No dihedral angle will be considered. As for the twist angle necessary for the washout at the wing tip to meet the set requirements, discussed further ahead, it will be obtained by manipulating the incidence angle, iW.

Table 3.1 summarizes the parameters previously presented. Depending on the part in construction, the relevant parameters are selected and applied, allowing for a swift manipulation of the overall size of the part.

3.2   Software Selection

When it comes to the CAD software, there is a wide array of options available in the market. Each one of those software packages has its own advantages and drawbacks, some of them being more specialized towards a specific branch of engineering while others offer a more general solution to the

Parameter description	Parameter symbol	Parameter description	Parameter symbol
Half wing span	b	Top flange length	TF_l
Root chord	c_r	Top flange thickness	TF_t
Tip chord	c_t	Bottom flange length	BF_l
Rib spacing	r_s	Bottom flange thickness	BF_t
Rib thickness	r_t	Spar chordwise position	S_{cp}
Rib hollowness	r_h	Circular boom outer diameter	d_o
Web length	W_l	Circular boom inner diameter	d_i
Web thickness	W_t	Circular boom chordwise position	B_{cp}
		Incidence angle of the wing	iW

Table 3.1: Wing parameters.

design process. It is also worth noting that some of these software packages include a vast selection of toolboxes, including some that allow for a Finite Element Model (FEM) structural analysis. This feature is of great importance due to the fact that, since a structural analysis is to be carried out on the obtained CAD models, it eliminates the sometimes cumbersome task of importing a CAD model into a structural analysis software package. Another key feature necessary is a parametric modeling support, since, as previously stated, it is required to take into account the fact that changes will be made during the design process, and a parametric design process allows for these changes to be implemented with no need to start a new model from scratch.

An user friendly graphic user interface is also a feature to take into account, since it makes the entire design process easier and more pleasant.

Four software packages were considered:

- Dassault Systèmes SolidWorks® [15] is one of the first software packages that comes to mind when CAD modeling is concerned. It is one of the most powerful 3D modeling tools on the market, featuring an user friendly interface. It also includes a structural analysis module. One of its more remarkable customers are Robert Bosh LLC.

- Also developed by Dassault Systèmes, CATIA® [16] was another option considered. This software package is far beyond a mere CAD modeling tool, enabling the user to address the complete product development process. It possesses a wide range of toolboxes, including FEM structural analysis, while remaining user friendly. This software package has been used throughout the years by some of the biggest names of the the aerospace industry. Boeing (which used it to develop both its 777 and 787), Airbus, Bombardier Aerospace and EMBRAER are some of those big companies. It is also widely used by some of the greatest automotive companies, such as BMW, Volkswagen/Audi and Ford.

- Siemens NX® [17] was another considered software. It fulfills a role similar to CATIA®, as it also has its sights set beyond simple CAD modeling, also allowing for product lifecycle management. It also includes FEM structural analysis toolboxes, remaining user friendly. NX is also used by renowned aerospace and automotive companies, such as Boeing, Rolls-Royce and NASA for the first industry and General Motors, Fiat and Nissan for the latter.

- The final software package considered was FreeCad®. Its main advantage when compared to the previously presented is that it is open source and free. However it is merely a CAD modeling tool, and if one needs to carry out a structural analysis, the CAD model needs to be imported into another software, such as ANSYS®, or even CATIA® or NX®.

Having presented all software packages considered, it can be seen that one of the key features required is satisfied by all of them, since parametric design is supported by the four. However, FreeCad® falls short when it comes to an integration of structural analysis modules. All other software packages allow for an integrated design and analysis approach. Due to its wide use in the aerospace industry, CATIA® has modules specially adapted to the design of aircraft parts, while remaining user friendly and satisfying the two desired key features. As such, it was the chosen software to obtain the CAD model and, in a later phase of the project, carry out a FEM structural analysis.

3.3 CAD Modeling Process

Taking into account the parameters presented in Table 3.1, the parametric CAD modeling process will be described throughout this section. Only the left half-wing was modeled, given the symmetrical nature of the wing structure. At this point, only the general modeling process will be presented. Some more specific aspects of the model, including dimensions, will be presented at a later stage of the project.

Firstly, the airfoil profile was drawn in CATIA®. As previously stated, this airfoil was obtained earlier in the LEEUAV design process, using an in-house software, in order to meet the performance requirements set for the aircraft.

Using this profile, it was possible to obtain the overall shape of the ribs that are a main component of both the sheeted and non-sheeted types of structures, by means of a simple pad operation in the CATIA® Part Design workbench. Figure 3.2 shows the overall shape of the ribs.
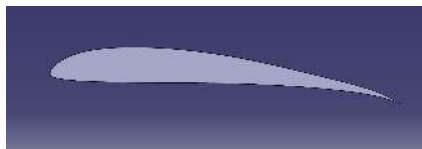
Figure 3.2: Rib shape modeled in CATIA®.

As seen in Section 2.2.1, the wing as a constant chord until 1400 mm span. After this point, the chord decreases linearly, from 350 mm on the previous section of the wing to 250 mm measured at the wing tip. As such, scaling operations were performed on the previously obtained rib shape, so as to obtain the ribs with the desired size in order to model the tapered portion of the wing. Since the chord varies linearly along this tapered section, depending on the spanwise position of the rib, an interpolation was made in order to determine the chord of each rib placed on this section of the wing, allowing for the determination of the amplification factor. This scaling operation was performed using the trailing edge as the reference point.

Furthermore, it was determined that a washout of 4.5º should be implemented in the wing tip, so as to meet the requirements set for flight at 7.5 m/s. As such, after the scaling operation was performed, a rotation operation took place. It was assumed that this washout angle varied linearly along the tapered section of the wing, having its value for the chordwise position of each rib at this section been determined, once again, by an interpolation process, knowing that the twist angle until 1400 mm span is 0º. This rotation was processed using the leading edge as a reference point.

Having the overall shape of the ribs determined, the following step was the choice of a spar cross section and modeling of this part. A simple rectangular cross section solid beam was chosen as a first spar, due to its simple and easy to build and manipulate features. The cross section was sketched, and a pad operation performed on it, resulting on the part shown in Figure 3.3 (a).

(a) Main spar modeled in CATIA®.

(b) Circular boom modeled in Catia®.
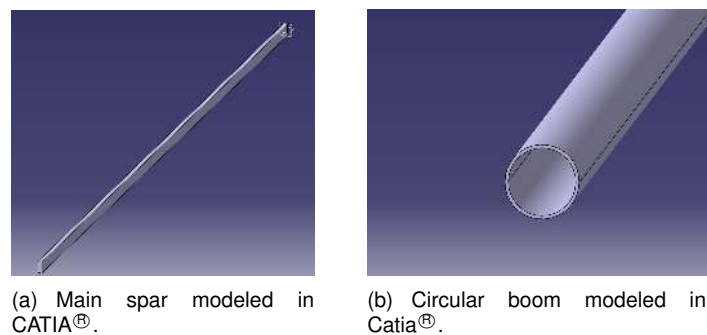
Figure 3.3: Main spar and boom models obtained in CATIA®.

A longitudinal stiffening tube was also designed, in order to provide more stiffness to the wing. This part consists of a hollow circular beam, intended to be installed in a position towards the trailing edge. Once again, its cross section was sketched, and a pad operation performed in order to obtain the complete beam. Figure 3.3 (b) shows a detail of this part.

After having the two previously presented beams modeled, it was necessary to further model the ribs, to account for their assembly to the beams. Firstly, the cross section of the spar was sketched on the rib model presented in Figure 3.2. The positioning of the spar was chosen to be at roughly 1/4 of the chord. The ribs have a greater area in the vicinity of this point, allowing for a better installation of the spar and, consequently, a better transfer of forces between both parts. A pocket operation was then performed, and a hole with the shape of the spar cross section obtained. A second hole was produced, near 2/3 of chord, with a circular shape that matches the outer radius of the circular beam previously presented. The process was identical to the described for the creation of the spar hole. Finally, a circular hole was created between the already presented two. Its main purpose is to allow for the passage of cables connecting to the aileron actuators and other features, such as the solar panels. The radius of this hole may also be manipulated in order to change the weight of the ribs, and thus, of the entire wing structure. Figure 3.4 shows all these features of the ribs.

As far as the individual parts of the wing structure are concerned, these are the ones that are worth
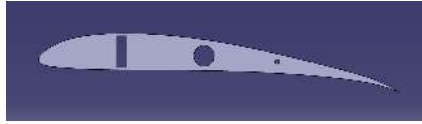
Figure 3.4: Rib modeled in CATIA®.

pointing out, since almost every structure presented in Section 2.4.2, with the exception of the Jedelsky wing, incorporates some variation of these components.

All that remains in order to obtain the full model of the wing is to assemble those individual components together. This was done using CATIA® Assembly Design workbench. When using this workbench, all the parameters used during the modeling of each individual part can be checked and edited, and the definition of new parameters can be made. The most important parameter defined at this stage was the rib spacing, since it determines the number of ribs that will be present in the wing.

In order to further exemplify the assembly process, the non-sheeted wing structure was modeled. The individual parts were obtained using the previously presented methods, and assembled together using coincidence, contact and offset constraints. At 1400 mm in the spanwise direction, where the tapered section begins, the main spar ends, and a smaller spar, placed further back in the chordwise position, is mounted into a support attached to the main one. By doing so, problems with the construction of a tapered spar are avoided. This type of construction also allows for the separation of both wing sections at that point, for ease of transportation.

The aileron, placed in the tapered section of the wing, was obtained using the shape of the ribs at this point. It is worth noting that it was built so as to smoothly adjust to the twist that this section of the wing has due to the washout requirement. It will be connected to the wing by means of hinges, attached to a small beam mounted in the wing that runs along the aileron length. The aileron itself has a structure similar to the wing, with ribs whose shape consists of the section of the wing ribs in the proximity of the trailing edge, attached to a beam to where the previously mentioned hinges will connect.
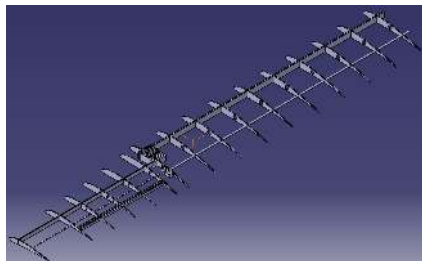
Figure 3.5: Non-sheeted structure modeled in CATIA®.

Figure 3.5 shows the assembly of the non-sheeted wing structure, without the inclusion of the solar panels. This generic structure can be modified and lead to several types of structures. A semi-sheeted structure can be obtained by modeling covers for the leading edge. It is also possible to obtain a fully-sheeted wing, if a solid, thick cover is modeled.

Chapter 4

Structural Analysis

Having obtained the CAD model of the wing structure, it is possible to proceed to the analysis of its behavior when subjected to specific loading cases. In this section, the fundamentals of the application of the Finite Element Analysis to a wing structural analysis process will be discussed, its limitations pointed out and means to bypass them identified.

4.1 FEM Applied to the Structural Analysis of a Wing

The fundamentals of FEM are the same regardless of the problem under consideration. The domain of the problem is divided into several smaller elements, and the matrices corresponding to each element defined, depending on the chosen element type. Connectivity tables are produced, followed by the assembly of the individual matrices of the elements into a global matrix relative to the entire domain [18]. Interpolation functions are defined, taking into account a reference element, followed by the transformation of that element into a real element using a Jacobian matrix.

This transformation needs to be made because the equations describing the physical problem under analysis are taking into account the real domain, and they need to be transported into each element, taking into account its degrees of freedom. Details on how these approximation functions are found and how they are transported from the reference elements into the real elements are described in detail in [19].

Several static FEM analysis will be carried out throughout this thesis, in order not only to perform validation of the determined material properties but also of the results of the physical tests performed on the prototype. The fundamentals necessary to perform those analysis will now be presented.

4.1.1 Element Types

Firstly, it is necessary to choose a type of element, and understand its properties. Following the software selection discussion presented in Section 3.2, it was decided that CATIA® was to be used due to its structural analysis module. This module allows for the usage of two different types of elements applicable to a three dimensional problem.

23

The simpler element used by this software is a linear tetrahedral element. This type of element possesses four nodes, and it is an isoparametric element, meaning that the geometric nodes are identical to the interpolation nodes. Figure 4.1 illustrates this element.
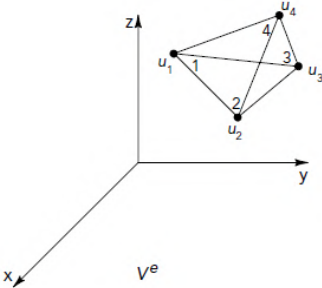
Figure 4.1: Tetrahedral linear element. Figure 4.2: Tetrahedral quadratic element.
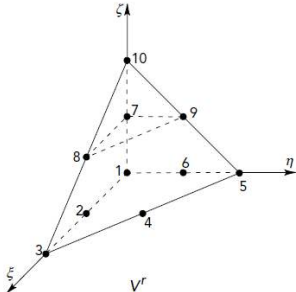
Each one of the four nodes has 3 degrees of freedom, which accounts for a total of twelve degrees of freedom per element. This type of elements are, however, using linear approximation equations, more susceptible to producing less accurate results.

An alternative to this element is the quadratic tetrahedron element, presented in Figure 4.2.

Although geometrically identical to the linear tetrahedral element, it hs six more nodes, one at the middle of each edge, accounting for a total of 10 nodes, with three degrees of freedom each. This element, obtained by means of a quadratic polynomial basis, produces more accurate results than the previously presented linear one. However, this increased precision comes at the cost of performance, since the increased number of nodes leads to larger matrices, and, consequently, longer computation times.

4.1.2 Mesh Parameters

Each part of an assembly is meshed separately. This means that, for example, the ribs located at a chordwise coordinate closer to the wing root may have a finer mesh than the others, and that the properties of the mesh may be different depending on the part being meshed.

As far as the mesh parameters are concerned, CATIA®'s Generative Structural Analysis workbench has several options available, that allow for a control of the mesh both in a global and, when needed, local approach.

Taking, at first, a look at the global mesh properties for each part, it is possible to define the size of the elements, as well as the sag. The sag parameter determines how well the the mesh fits the geometry of the part. Its effect is specially visible when applying a mesh to a curved part, such as the ribs, in this case. The sag parameter can be controlled both in an absolute and a proportional manner, or even both simultaneously. The absolute sag represents the maximum gap between the mesh and the geometry, as illustrated in Figure 4.3, while the proportional sag is expressed according to Equation (4.1).

$$\text{Proportional sag value} = \frac{\text{local absolute sag value}}{\text{local mesh edge length value}} \qquad (4.1)$$
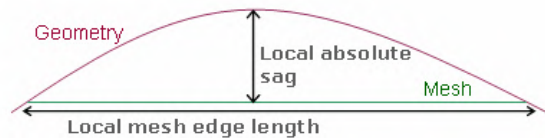
Figure 4.3: Absolute sag mesh parameter [20].

In order for the mesh to properly adjust itself to the geometry of the parts, a low absolute sag value will be imposed in the meshes produced later on. It is worth noting that, when both control parameters are simultaneously selected, the most constraining one will take effect.

If one desires to obtain a finer mesh in a specific location of a part, it is possible to define a local mesh size and absolute or proportional sag. This feature is extremely useful since it allows for a local, instead of global, refinement of a given part mesh, providing a means to save computation time by maintaining a coarse mesh in less problematic regions of the part while making it finer near connection zones and other critical features.

Another important feature is the ability to manage the quality of the mesh, using one of three criteria: shape, skewness and stretch. In this case, when parabolic elements are to be used, the manipulation of the intermediate node parameters allow for the manipulation of the intermediate point of the tetrahedron elements, by tweaking the values of the Jacobian and warp parameters. The values attributed to these parameters also influence how well the mesh fits the part geometry, since the distance between the intermediate node and the geometry is a function of both the Jacobian and warp parameters.

Several other tools are available for the manipulation of the mesh. Although not all of them will be used, some may yet come to be useful, such as the ability to suppress mesh edges. This operation is performed after the part is meshed, and alters it by checking for small element edges, and locally changing the configuration of the elements, eliminating smaller ones and replacing them by larger ones, as seen in figures 4.4. When performing this operation, one must bear in mind that since some edges are being eliminated, some applied constraints may not be respected.

(a) Before edge suppression.

(b) After edge suppression.
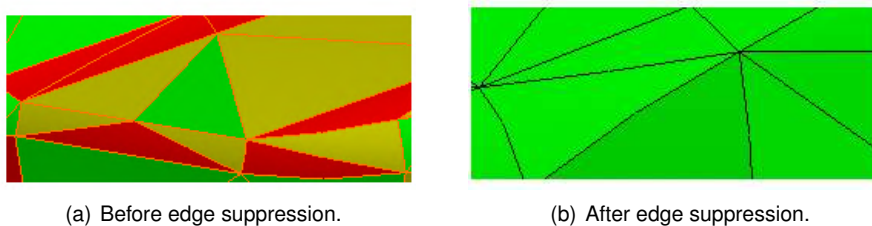
Figure 4.4: Effect of edge suppression on a 3D mesh [20].

As an example of all the previously presented mesh parameters, different meshes obtained for the rib presented in Section 3.3, Figure 3.4 will be presented. All meshes will be obtained using the quadratic tetrahedral elements, presented in Figure 4.2, for the reasons discussed earlier.

Example mesh 1, presented in figure 4.5, was obtained by manipulating only the global mesh parameters, maintaining the default values suggested by CATIA® for the remaining ones. The active mesh parameters used for the creation of this mesh are presented in Table 4.1.

(a) Complete rib.   (b) Hole detail.
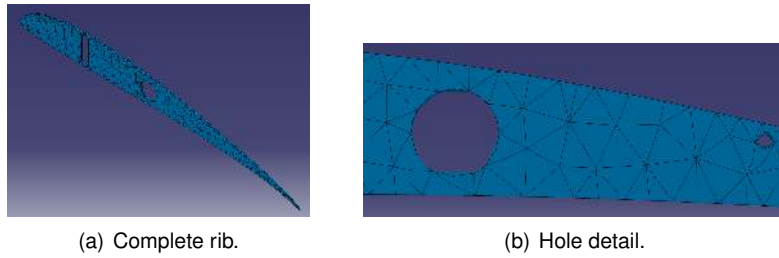
Figure 4.5: Example mesh 1 for the rib part.

Global parameters	
Size	10 mm
Absolute sag	5 mm
Quality parameters	
Criteria	Shape
Jacobian	0.3
Warp	60
Other parameters	
Geometry size limit	0.1 mm
Mesh edges suppression	0.2
Minimum size for sag specs	2.726 mm

Table 4.1: Example mesh 1 parameters

It can be seen, in Figure 4.5, that near the leading edge, the mesh does not adequately fit the geometry of the part, generating angular regions, instead of the smooth curve it was supposed to show. As such, the absolute sag parameter should be lowered. It can also be seen that this is a rather coarse mesh, with instances of elements that go from the upper to the lower surface.

Also regarding this mesh, by looking at the detail shown Figure 4.5 (b), it can be seen that it adapts very poorly to the circular holes created on the rib. In order to improve this, local parameters could be defined for these edges. However, since a finer mesh is to be obtained, it is convenient to first check how it fits those features of the part.

(a) Complete rib.   (b) Hole detail.
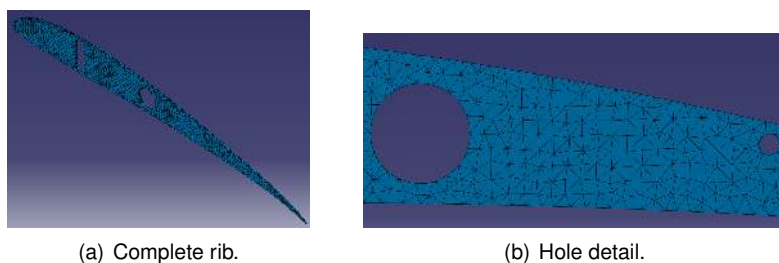
Figure 4.6: Example mesh 2 for the rib part.

Figure 4.6 shows the finer mesh obtained for the rib. Once again, only global mesh parameter were used in the creation of this mesh, maintaining the rest with their default values suggested by CATIA®. The parameters used and their values are presented in Table 4.2.

It can be seen that the overall mesh fits the geometry of the part much better. This comes as an

Global parameters	
Size	3 mm
Absolute sag	1 mm
Quality parameters	
Criteria	Shape
Jacobian	0.3
Warp	60
Other parameters	
Geometry size limit	0.1 mm
Mesh edges suppresion	0.2
Minimum size for sag specs	2.726 mm

Table 4.2: Example mesh 2 parameters

effect of the smaller element size, as well as a reduced absolute sag parameter. It is also expected to produce more accurate results, since there is a greater number of elements when compared to example mesh 1.

However, by looking carefully at figure 4.6 (b) it can be seen that, although the mesh fits the hole used for the passage of cables and weight reduction almost perfectly, it still does not adapt well to the hole through which the circular stiffening beam will pass. This is a particularly important region of the part, since stresses will be transferred between parts at that specific location. As such, it is convenient to locally refine the mesh in the vicinity of that hole.
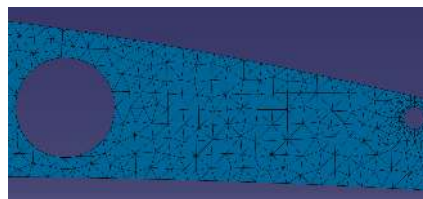
Figure 4.7: Local refinement on example mesh 2.

As one can see in Figure 4.7, a much better mesh was obtained in the vicinity of the hole discussed earlier by defining local size and absolute sag parameters, whose values are presented in Table 4.3.

Local parameters	
Size	1 mm
Absolute sag	1.25 mm

Table 4.3: Local refinement parameters in example mesh 2

This mesh serves, at this point, only as an example of the influence of the mesh parameters in its final form. Further ahead, when analyses are carried out, different meshes will be produced, and a discussion will be made regarding the selection of the mesh that best suits the problem.

4.1.3 Connection Types

After selecting the type of element used for the simulation, as well as providing a first value for the mesh parameters, it is necessary to define the type of interaction between each part of the assembled wing structure. CATIA®'s Generative Structural Analysis workbench provides the user with a wide array of choices as far as the type of connection between parts is concerned, from slider connections, to pressure fitting, or even spot and seam welding. Each of these connections has its own properties, and manipulates the interaction between the meshes of the different parts in a distinct manner. However, regardless of the type of connection used, it is first necessary to identify which surfaces, lines or points interact with each other, so that the software can properly apply the connection property chosen. This is done by creating a general analysis connection. This has no influence on the property of the connection, and only serves the purpose of marking that some type of interaction will exist between the selected entities. As such, this process has to be repeated for every surface, line or point of the assembled structure where an interaction between parts exists.

Having defined all the general analysis connections, three different types of connection properties were tested. At a more preliminary stage, two types of virtual connections were used. These are the rigid and smooth connections, and are called virtual since they are used to connect parts who do not have a common interface with a third body.

The rigid connection property links two bodies which are fastened together at their common boundaries. What it does is to create a rigid spider finite element which connects all the nodes of the interacting surfaces to a null-length bar created at the midpoint between the nodes of the two meshed parts, as can be seen in figure 4.8 (a). This type of element, shown in figure 4.8 (b), does not have a constant number of nodes, since it depends on how many nodes there are in the surfaces it connects. It has 6 degrees of freedom per node, taking into account translations and rotations in the three axis. The master node belongs to the null-length bar, and the slave nodes correspond to the ones present on the surface meshes.

(a) Rigid connection diagram. (b) Rigid spider element.
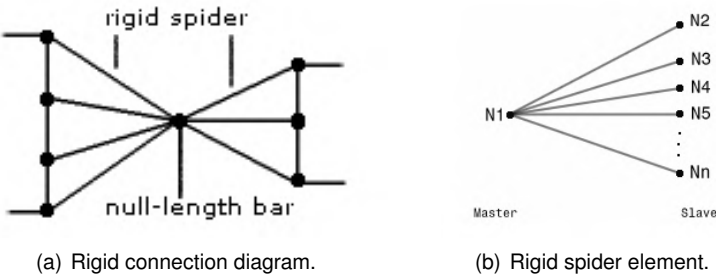
Figure 4.8: Rigid connection.

However, this type of connection does not take into account the elastic deformation between the interface surfaces, and thus considers it to be infinitely rigid. As such, it is not an appropriate connection to use in future analysis, since using it would ultimately turn the entire spar into a infinitely rigid beam, since every segment of this beam between ribs would be considered rigid, thus only allowing for the deformation of the ribs themselves.

The smooth connection, schematically represented in Figure 4.9, was then considered. This type of

connection is similar to the rigid one, in the sense that it is used to link two bodies which are fastened together using a spider element identical to the one presented in Figure 4.8 (b) connecting each of those interacting surfaces to a null-length bar created at the midpoint between their mesh nodes. However, it takes into account an approximate elastic deformability of the interface between the bodies, based on a least squares fit of the slave nodes linked to the master nodes.
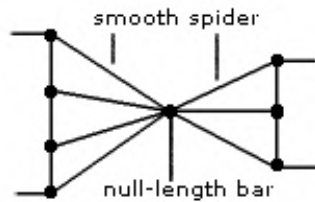
Figure 4.9: Smooth connection diagram.

This type of connection, already accounting for a deformation of the interfaces between the several parts of the assembly, allows for the deformation of the entire structure, which did not happen using the rigid connection. However, it still uses an approximation for the displacement of the nodes connected to the null-length bar, consequently producing results whose accuracy may be further improved.

Finally, the fastened connection was tested. This connection also considers the parts fastened together at their interface. However, in this case, a spider element connecting the different bodies to a null-length bar is not created. In fact, this connection simply merges the nodes of the meshes of the interacting surfaces. By doing so, more than taking into account the elastic deformation of the interface between the bodies, they act as if they become a single body, due to the merging operation that occurred in the interacting surface nodes. CATIA® is also capable of handling incompatible meshes using this type of connection, making it possible to further refine the mesh of one of the connected parts while maintaining the other unchanged, without problems when it comes to the mesh compatibility at the interface.

After considering the aforementioned properties of each of the discussed connection methods, it was determined that the fastened connection was the one that more accurately described the real life problem, and thus will be the one used for the analysis carried on at a later stage.

4.1.4 Boundary Conditions

All that remains for the model to be complete is to apply the boundary conditions. Regarding the constraints, it will be assumed, according to the wing design methodology presented in Section 2.4, that the spar and the stiffening circular beam are cantilever beams, fixed at their roots. Thus, all degrees of freedom were constrained in the root surfaces of both those beams in the model. These constraints were applied to the geometric faces themselves, and not the nodes of the specific mesh active at that point. By doing so, CATIA® transfers the constraint to whatever mesh is active at the moment, meaning that there is no need to change the definition of the constraint itself when changes are made to the mesh.

4.2 Constitutive laws

In order to understand the behavior of a given material, it is important to be familiar with its constitutive laws [21]. These laws relate stresses and strains, according to the properties of the material. The equations describing these constitutive laws are based on the assumption of ideal elasticity, meaning that the body recovers its original form after the removal of the forces causing its deformation. As such, they do not account for creep or stress relaxation. The material properties present in these laws are considered constant throughout the deformation of the material.

As shown in [22], the general form of the constitutive laws for infinitesimal deformation is, based on Hooke's law

$$\sigma_{ij} = C_{ijkl}\epsilon_{kl} + \sigma_{ij}^0, \tag{4.2}$$

where, C is the stiffness tensor, including the material parameters, σ_{ij} the components of stress, ϵ_{kl} the components of strain and σ_{ij}^0 the components of stress assuming that the body is pre-stressed. Due to the symmetrical properties of the stress components ($\sigma_{ij} = \sigma_{ji}$), the stiffness tensor also needs to be symmetrical in the first two subscripts, thus being a square 6x6 matrix.

As for the components of stress and strain, it is usual to express them using only one subscript. When i and j are equal, we have the stress or strain components in each of the main axis, meaning that $11 \rightarrow 1$, $22 \rightarrow 2$ and $33 \rightarrow 3$. When $i \neq j$, the assumed convention is $23 \rightarrow 4$, $13 \rightarrow 5$ and $12 \rightarrow 6$. For the strain components with subscript between 4 and 6, it is also necessary to take into account that

$$\epsilon_4 = 2\epsilon_{23}; \epsilon_5 = 2\epsilon_{13}; \epsilon_6 = 2\epsilon_{12} \tag{4.3}$$

In the wake of this nomenclature, C needs to be expressed using only subscripts i and j. This is called the Voigt-Kelvin notation [22].

Equation (4.2) is invertible, and the strain expressed in function of the stress, using the Voigt-kelvin notation, according to

$$\epsilon_i = S_{ij}\sigma_j + \epsilon_i^0 \tag{4.4}$$

or in matrix notation,

$$
\begin{Bmatrix} \epsilon_1 \\ \epsilon_2 \\ \epsilon_3 \\ \epsilon_4 \\ \epsilon_5 \\ \epsilon_6 \end{Bmatrix} =
\begin{bmatrix}
S_{11} & S_{12} & S_{13} & S_{14} & S_{15} & S_{16} \\
S_{21} & S_{22} & S_{23} & S_{24} & S_{25} & S_{26} \\
S_{31} & S_{32} & S_{33} & S_{34} & S_{35} & S_{36} \\
S_{41} & S_{42} & S_{43} & S_{44} & S_{45} & S_{46} \\
S_{51} & S_{52} & S_{53} & S_{54} & S_{55} & S_{56} \\
S_{61} & S_{62} & S_{63} & S_{64} & S_{65} & S_{66}
\end{bmatrix}
\begin{Bmatrix} \sigma_1 \\ \sigma_2 \\ \sigma_3 \\ \sigma_4 \\ \sigma_5 \\ \sigma_6 \end{Bmatrix} +
\begin{Bmatrix} \epsilon_1^0 \\ \epsilon_2^0 \\ \epsilon_3^0 \\ \epsilon_4^0 \\ \epsilon_5^0 \\ \epsilon_6^0 \end{Bmatrix}, \tag{4.5}
$$

where matrix [S] is called the compliance coefficients matrix. Each of its entries contains the material elastic properties in a given direction, thus containing all the information necessary to relate strains and stresses.

Assuming an initial state without deformation, components $\epsilon_i^0 = 0$, and the last vector of Equation (4.5) disappears. These equations can be further simplified, taking into account the properties of the

specific types of materials.

4.2.1 Orthotropic materials

A material is said to be orthotropic when it has three mutually orthogonal axes of symmetry, presenting different elastic properties along each of those axes. Wood is a prime example of this class of materials. In this particular case, the constitutive law takes the form presented in Equation (4.7), as shown in [22].

$$
\begin{Bmatrix} \epsilon_1 \\ \epsilon_2 \\ \epsilon_3 \\ \epsilon_4 \\ \epsilon_5 \\ \epsilon_6 \end{Bmatrix} = \begin{bmatrix} S_{11} & S_{12} & S_{13} & 0 & 0 & 0 \\ S_{21} & S_{22} & S_{23} & 0 & 0 & 0 \\ S_{31} & S_{32} & S_{33} & 0 & 0 & 0 \\ 0 & 0 & 0 & S_{44} & 0 & 0 \\ 0 & 0 & 0 & 0 & S_{55} & 0 \\ 0 & 0 & 0 & 0 & 0 & S_{66} \end{bmatrix} \begin{Bmatrix} \sigma_1 \\ \sigma_2 \\ \sigma_3 \\ \sigma_4 \\ \sigma_5 \\ \sigma_6 \end{Bmatrix}.
\tag{4.6}
$$

Substituting the different entries S_{ij} in the matrix of Equation (4.7) by the adequate elastic properties (Young modulus (E), shear modulus (G) and Poisson coefficient (ν)), yields

$$
\begin{Bmatrix} \epsilon_1 \\ \epsilon_2 \\ \epsilon_3 \\ \epsilon_4 \\ \epsilon_5 \\ \epsilon_6 \end{Bmatrix} = \begin{bmatrix} \frac{1}{E_1} & -\frac{\nu_{21}}{E_2} & -\frac{\nu_{31}}{E_3} & 0 & 0 & 0 \\ -\frac{\nu_{12}}{E_1} & \frac{1}{E_2} & -\frac{\nu_{32}}{E_3} & 0 & 0 & 0 \\ -\frac{\nu_{13}}{E_1} & -\frac{\nu_{23}}{E_2} & \frac{1}{E_3} & 0 & 0 & 0 \\ 0 & 0 & 0 & \frac{1}{G_{23}} & 0 & 0 \\ 0 & 0 & 0 & 0 & \frac{1}{G_{13}} & 0 \\ 0 & 0 & 0 & 0 & 0 & \frac{1}{G_{12}} \end{bmatrix} \begin{Bmatrix} \sigma_1 \\ \sigma_2 \\ \sigma_3 \\ \sigma_4 \\ \sigma_5 \\ \sigma_6 \end{Bmatrix}.
\tag{4.7}
$$

This matrix is symmetric, thus providing a relationship between the elastic properties outside the diagonal of the matrix.

4.2.2 Isotropic materials

In the case of isotropic materials, the elastic properties are uniform throughout the material, with no preferred directions. As such, the Young modulus (E), shear modulus (G) and Poisson coefficient (ν) are constant in the entire material sample.

In this case, after substituting the S_{ij} entries in the matrix of the constitutive law, results

$$
\begin{Bmatrix} \epsilon_1 \\ \epsilon_2 \\ \epsilon_3 \\ \epsilon_4 \\ \epsilon_5 \\ \epsilon_6 \end{Bmatrix} = \begin{bmatrix} \frac{1}{E} & -\frac{\nu}{E} & -\frac{\nu}{E} & 0 & 0 & 0 \\ -\frac{\nu}{E} & \frac{1}{E} & -\frac{\nu}{E} & 0 & 0 & 0 \\ -\frac{\nu}{E} & -\frac{\nu}{E} & \frac{1}{E} & 0 & 0 & 0 \\ 0 & 0 & 0 & \frac{1+\nu}{E} & 0 & 0 \\ 0 & 0 & 0 & 0 & \frac{1+\nu}{E} & 0 \\ 0 & 0 & 0 & 0 & 0 & \frac{1+\nu}{E} \end{bmatrix} \begin{Bmatrix} \sigma_1 \\ \sigma_2 \\ \sigma_3 \\ \sigma_4 \\ \sigma_5 \\ \sigma_6 \end{Bmatrix}.
\tag{4.8}
$$

This is the simplest form of the material constitutive laws, since the assumption of an isotropic material forces the existence of only two independent elastic coefficients, being their relation given by

$$G = \frac{E}{2(1+\nu)}.$$

<div align="right">(4.9)</div>

4.2.3 Composites

Composites are inherently an anisotropic material. Their material properties are highly direction dependent, and their specific characteristics must be taken into account when deriving their constitutive laws.

For the case of a laminate composite, these constitutive relations are specific for each lamina, under the assumptions that said lamina is a continuum and behaves as a linear elastic material, according to [22]. These assumptions make it possible to consider the composite material to be homogeneous, from a macroscopic perspective.

Considering a lamina comprised of a matrix and uni-directional fiber reinforcement, it may be assumed that it is an orthotropic material, with two axes of symmetry, one parallel to the direction of the fibers, and one perpendicular to it. The local coordinate system considered for this type of lamina is depicted in Figure 4.10. The constitutive relations presented in Section 4.2.1 apply, taking into account this coordinate system.
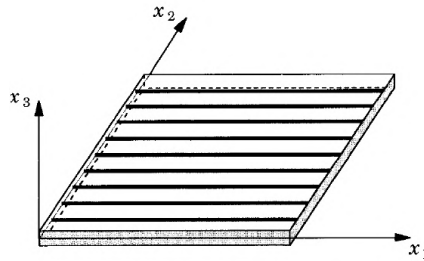
Figure 4.10: Fiber reinforced composite layer coordinate system.

It is, consequently, necessary to derive the orthotropic properties of the composite material. For that purpose, a micromechanics approach is usually taken, as presented in [22]. Considering a perfect bond between the fibers and the matrix, a uniform distribution of those fibers, a matrix with no voids, an isotropic behavior of both matrix and fiber, and assuming that the composite is only subjected to loading parallel or perpendicular to the fiber direction, the following results are obtained, according to [22]:

$$
\begin{aligned}
E_1 &= E_f v_f + E_m v_m &;& \quad \nu_{12} = \nu_f v_f + \nu_m v_m \\
E_2 &= \frac{E_f E_m}{E_f v_m + E_m v_f} &;& \quad G_{12} = \frac{G_f G_m}{G_f v_m + G_m v_f}
\end{aligned}
$$

<div align="right">(4.10)</div>

where v_m and v_f are the volume percentage of matrix and fibers, respectively, and

$$G_f = \frac{E_f}{2(1+\nu_f)} \quad ; \quad G_m = \frac{E_m}{2(1+\nu_m)}$$

<div align="right">(4.11)</div>

However, since Equations (4.7) are valid in the local coordinate system, and since each layer of the laminate composite will have its own coordinate system, a transformation of coordinates will have to be made. In fact, each layer of composite material has its own fiber orientation, an thus, even though the planes defined by axis x_1 and x_2 will always be parallel, the directions at which those two axes are oriented are not the same between layers of the material. As such, a global coordinate system, compatible with the overall problem under analysis, is defined, and transformation relations must be developed. Figure 4.11 shows a local and global coordinate system for a given layer, and the angles used for the transformation relations.
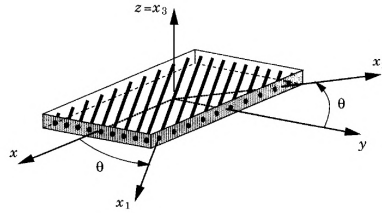
Figure 4.11: Local and global coordinate systems.

Since in Sections 4.2.1 and 4.2.2, the constitutive relations were presented in terms of strains, only the strain transformation relations will be presented here. All deductions and results for stress transformations may be found in [22]. The transformation of coordinate syste, is then given by

$$
\begin{Bmatrix} \epsilon_{xx} \\ \epsilon_{yy} \\ \epsilon_{zz} \\ 2\epsilon_{yz} \\ 2\epsilon_{xz} \\ 2\epsilon_{xy} \end{Bmatrix}
=
\begin{bmatrix}
\cos^2(\theta) & \sin^2(\theta) & 0 & 0 & 0 & -\sin(\theta)\cos(\theta) \\
\sin^2(\theta) & \cos^2(\theta) & 0 & 0 & 0 & \sin(\theta)\cos(\theta) \\
0 & 0 & 1 & 0 & 0 & 0 \\
0 & 0 & 0 & \cos(\theta) & \sin(\theta) & 0 \\
0 & 0 & 0 & -\sin(\theta) & \cos(\theta) & 0 \\
\sin(2\theta) & -\sin(2\theta) & 0 & 0 & 0 & \cos^2(\theta)-\sin^2(\theta)
\end{bmatrix}
\begin{Bmatrix} \epsilon_1 \\ \epsilon_2 \\ \epsilon_3 \\ \epsilon_4 \\ \epsilon_5 \\ \epsilon_6 \end{Bmatrix}
\tag{4.12}
$$

where the transformation matrix used in Equation (4.12) is usually referred to as [R].

This process also requires the material coefficients to be transformed from the local coordinates of each layer of the composite to the global coordinate system. As such, the compliance matrix [S] will be transformed into $[\overline{S}]$, which contains the material properties in the global coordinate system, according to

$$
[\overline{S}] = [R]^T [S][R].
\tag{4.13}
$$

Having all the variables and constants of the problem defined in the global coordinate system is the key to being able to solve the problem of the deformation of a composite material. The previously presented constitutive relations, not only for composites, but for all types of materials, are taken into account when performing stress and strain analyses, both by hand or when using FEM software.

4.3 Validation

In this section, a simple structural problem will be analytically solved, and the results compared to the ones obtained with CATIA®'s Generative Structural Analysis Workbench. This will be done with the intention of validating the results, and thus checking if the mesh options and FEM model simplifications are adequate.

For simplicity, a simple cantilever beam, made of an isotropic material, with a concentrated load acting at its free end will be considered. This general problem is depicted in Figure 4.12, considering a rectangular cross-section for the beam.
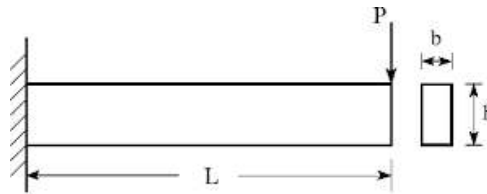
Figure 4.12: Cantilever beam validation problem.

Let the dimensions in Table 4.5 be considered for the beam, under a loading of $P = 50N$ in the presented direction.

The material properties used in this analysis are those of Titanium, available in CATIA®'s material database, and presented in Table 4.4.

E	$1.14 \cdot 10^{11}$ Pa
ν	0.34
ρ	$4460 Kg/m^3$
σ_{yield}	$8.25 \cdot 10^8$ Pa

L	50 cm
b	5 mm
h	15 mm

Table 4.4: Material properties of the titanium used on the beam.

Table 4.5: Dimensions considered for the cantilever beam validation problem.

The displacement of the beam will be analytically calculated and compared with the numerical results obtained using CATIA®.

Theoretically, for a cantilever beam, the displacement along its length is given by (considering y to be the vertical axis, and x the axis along the beam length, L) [23]

$$y = \frac{Px^2}{6EI}(3L - x),\tag{4.14}$$

where E is the Young's modulus of the material and I the area moment of inertia of the beam cross-section, with reference to the axis passing through its center, as depicted in Figure 4.13.

As such, and according to the dimensions presented in Table 4.5, the area moment of inertia of the beam's cross-section is given by

$$I = \frac{bh^3}{12} = 1.40625 \cdot 10^-9 m^4.\tag{4.15}$$

Substituting all the known values in Equation (4.14), it is possible to obtain the theoretical displace-
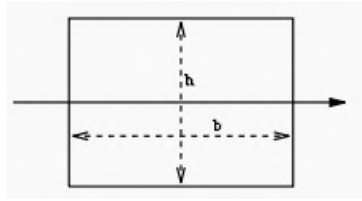
Figure 4.13: Axis with respect to which the cross-sectional area moment of inertia is calculated.

ment of the beam along its length, plotted in figure 4.14.
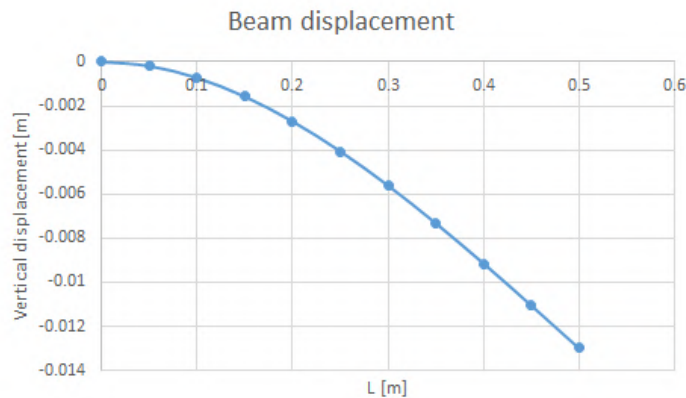
Figure 4.14: Theoretical displacement of the beam along its length.

Considering the displacement at the free end of the beam, substituting the values in Equation (4.14), it can be seen that a maximum displacement of 0.013 m is expected.

Having the theoretical solution determined, it is necessary to model the problem in CATIA®. The beam was created, and the mesh properties presented in Table 4.6 used, taking into account the usage of tetrahedron quadratic elements, for a convergence study. The maximum displacement obtained with each mesh is also presented Table 4.6. A point was created in order to apply the load. This point is located at the center of the upper edge of the free end of the beam. The fixed end was clamped, and the force applied.

As one can, even though the number of element is increasing from mesh 1 to 3, the obtained displacement remains constant. It can then be assumed that the result has converged. Mesh 2 will be used, since the computational time is approximately the same as for mesh 1, but significantly lower than for mesh 3.

Running a static analysis on the modeled problem using mesh 2, the deformed shape of the beam presented in Figure 4.15 was obtained.

As one can see in Figure 4.15, the maximum displacement of the beam is obtained in its free end, as expected, with a value of 13 mm. This value is consistent with the one determined using the theoretical equations, producing a relative error of only 0.038%.

Plotting the Von Mises stress distribution, it can be seen that the highest values of stress are located at the expected regions of the beam. Looking at Figure 4.16, it can be seen that the highest stress values are obtained on the upper and lower surfaces of the beam, in the vicinity of its clamped end. In

	Mesh 1	Mesh 2	Mesh 3
Global parameters			
Size	4 mm	2 mm	1 mm
Absolute sag	2 mm	1 mm	1 mm
Quality parameters			
Criteria	Shape	Shape	Shape
Jacobian	0.3	0.3	0.3
Warp	60	60	60
Other parameters			
Geometry size limit	0.1 mm	0.1 mm	0.1 mm
Mesh edges suppresion	0.2	0.2	0.2 mm
Minimum size for sag specs	3.908 mm	3.908 mm	3.908 mm
Number of elements	5298	28096	175637
Maximum displacement	13 mm	13 mm	13 mm

Table 4.6: Validation mesh parameters and convergence study.
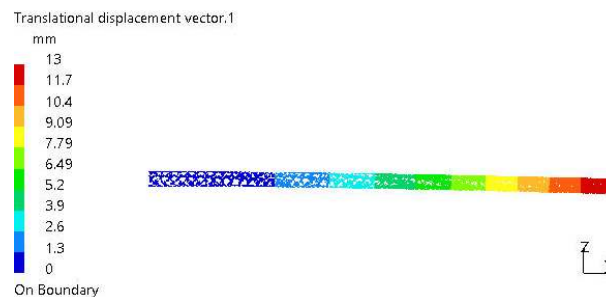
Figure 4.15: Deformed shape of the beam.

fact, under the given loading conditions, this is expected, since these are the regions where the beam will be subjected to maximum bending moment. The value of stress measured there, of $1.57 \cdot 10^8$ MPa is bellow the yield strength of the titanium chosen for the purposes of this analysis, meaning that this beam did not suffer plastic deformation.

It can also be seen that , the closer to the free end of the beam, the lower the values of the stress. Towards the central region of the beam cross-section, the stress values are much lower, consistent with the proximity to the neutral line.
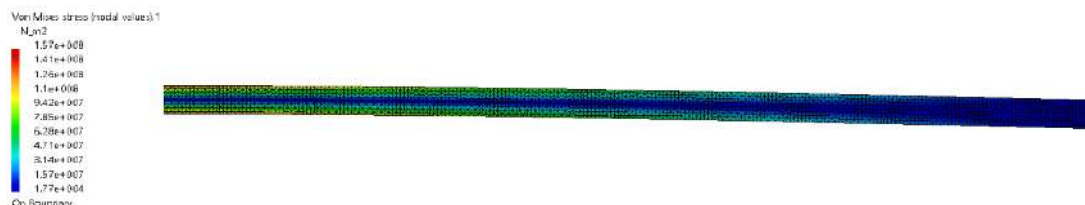
Figure 4.16: Von Mises stress distribution on the loaded beam.

It can then be assumed that CATIA®'s Generative Structural Analysis workbench is capable of producing results with an extremely good accuracy, given that the appropriate options are used, as this preliminary validation process demonstrated.

Chapter 5

Material Study

In order for the finite element analysis to yield the best results possible, it is necessary to use the most accurate input data possible. This applies not only to the boundary conditions and geometry of the problem, but also to the mechanical properties of the materials used in it. As such, it is of the utmost importance to accurately measure the mechanical properties, which requires knowledge of the testing methods applied to each material, as well as the characteristics of the material itself.

In this chapter, the materials used in the wing model will be identified, its main properties presented and the testing methods and procedures used to determine their mechanical properties outlined.

5.1 Materials Used in the Wing Model

In order to produce a wing capable of withstanding the loads generated during the LEEUAV mission profile without penalty to its weight and overall performance, it is necessary to select from a range of materials whose properties best meet these needs.

Taking into account that this is fundamentally a model aircraft, one of the first materials that comes to mind is wood, more specifically balsa. This is a very light, low density (about $200 \ kg/m^3$) wood, because of its large, thin walled cells, that, after a kiln drying process that evaporates the water contained within, provide strength due to its large surface area. These characteristics make this type of wood one of the best choices when it comes to modeling projects, be it aircraft or even building models [24].

Fiber glass layers of composite may also be added to the balsa parts in order to increase their strength. This comes at the cost of a slight increase of weight per part, mostly due to the resin applied in order to bind the fibers to the wood surface.

Plywood is also one of the materials to be taken into account. It consists of thin layers of wood glued together using different types of resins. The grain orientation of each layer of wood may differ. It is a form of composite material, with the fibers being composed of the cellulose cells of the wood plies used in its manufacturing. The fact that the grain orientation is not the same provides the plywood with a balanced strength in all directions. Usually, plywood panels have better quality plies on the outer surfaces, with normal ones on the core. This provides the overall piece of plywood with a better resistance to bending,

since the outer panels are the ones where greater values of stress due to bending will be measured. Different types of plywood are available on the market, with different characteristics. One of these is the aircraft plywood, built with stronger woods and resin with good resistance to heat and humidity [25].

Pultruded carbon tubes are also a common choice for this type of builds. In fact, due to its great strength and relatively reduced weight, they constitute an efficient choice when one wishes to increase the overall stiffness of the structure without a significant increase in structural weight.

Heat shrinking plastic will also be applied to cover the structure and give the wing prototype its outer shape.

Table 5.1 summarizes the different materials considered for the building prototype, and the parts in which they will be used.

Material	Part
Balsa wood	Spar and ribs
Plywood	Ribs
Pultruded carbon tube	Boom
Fiberglass composite	Spar and ribs reinforcement
Heat shrinking plastic	Cover

Table 5.1: Materials considered for building the prototype.

5.2   Wood Testing Methods

In this section, the testing procedures for the determination of the elastic properties of wood will be presented.

Wood structure is comprised of elongated cells, which are aligned vertically when the tree is alive, bonded together by lignin, a complex polymer that confers mechanical strength to those cell walls. These characteristics of wood allow it to be considered an orthotropic material, whose three principal axes of symmetry are the longitudinal, radial and tangential [26], resulting in 3 Youngs' moduli, 3 shear moduli and 6 Poisson's ratios (which make for the elastic properties comprised in the constitutive laws presented in Section 4.2).

Due to the fact that wood fibers have a preferable orientation, the tensile strength of wood in that direction will reach its greatest value. Since it is much higher than the values in other directions, it is not the determining factor in engineering design. However, when testing for such determining properties, difficulties arise due to the low values of shear parallel to the grain, which could cause the failure of the test specimen when tensile testing it, as described in [27].

The general principles applied to tensile testing still apply to tensile testing of wood. However, some adjustments must be made. It is shown in [27] that filleted test specimens should be used, so as to minimize the stress concentration. A 17.5 inch radius fillet is an ASTM standard for specimens used in parallel to grain tensile tests, as shown in Figure 5.1 (a).

Not only the specimen itself must be adapted, but also the testing rig used. The usage of clamp

supports with flat surfaces is not advisable for parallel to grain tensile tests, since they would crush the specimen due to its lower perpendicular to grain strength. A flat contact surface is also to be avoided, since slipping could occur. As such, notched shoulder supports are used, as illustrated in Figure 5.1 (b).

As for perpendicular to grain tensile testing, problems arise due to the smaller dimensions of the specimen in a direction perpendicular to the grain. Limitations to the usage of the aforementioned flat specimens come into play, such as stress concentration promoting failure near the grips.

There are also available documents that provide the usual relations between the several elastic properties of different types of wood, such as [28], that allow for an estimation of most of those properties based on an already determined one.

5.2.1   Parallel to the Grain Tension Tests

Following an iterative process, the specimens used for parallel to the grain tension tests were gradually improved, culminating in the development of a new specimen with a better performance in this type of tests. Further information on that evolution may be found in [27]. This specimen presents the aforementioned features that limit slippage and stress concentration, while being smaller than previously used ones, at 18 inches of length. Testing of this type of specimen also showed that results present less variation, although not in a very significant manner, having been successful in testing of an array of wood types. The head travel speed recommended by the authors for this specimen is of 0.03 inches per minute, in order for the load-strain data to be accurately obtained.

(a) Specimen suggested in [27].   (b) Testing   setup used in [27].
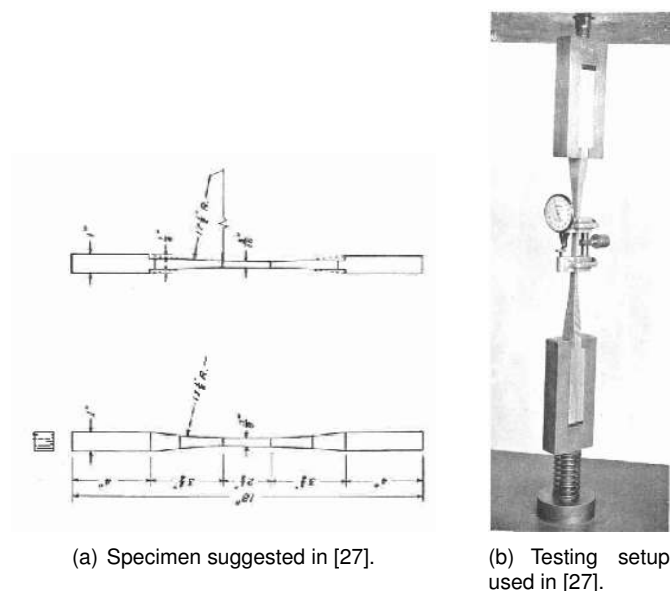
Figure 5.1: Parallel to the grain tension testing.

An extensometer is used to measure the displacement in the central region of the specimen, and, knowing the force applied by the loading cell, it is possible to plot the strain-stress graph with the gathered data, thus allowing for the determination of the Young modulus of the material.

Most of the suggestions made in [27] were later adopted by ASTM, and outlined in standard D143-94.

As far as the shear modulus is concerned, the one felt on the direction parallel to the grain is usually referred to as longitudinal shear. One test method used for the determination of this shear modulus, used in [29] and shown in Figure 5.2, suggested in ASTM standards, is based on the assumption that the test specimen will only fail along one zone of shear.
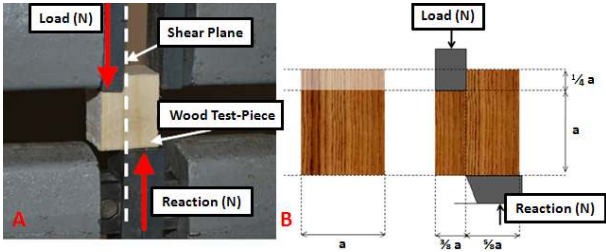
Figure 5.2: Shear along the grain testing rig suggested by American standards, and used in [29].

Using this method, the shear modulus of rigidity can promptly be determined, using its definition (equation 5.1), and considering values at the elastic limit of the material, as

$$G = \frac{FL}{A\Delta x},$$ (5.1)

where F is the applied force, L the length of the shear plane, A the cross-sectional area od the specimen, and Δx the displacement caused by shear.

Given the dimensions presented in the specimen of figure 5.2, the shear modulus definition can be manipulated, yielding the following result:

$$G = \frac{F}{a\Delta x}.$$ (5.2)

5.2.2 Perpendicular to the Grain Tension Tests

As mentioned before, the strength of wood perpendicularly to the grain is much smaller than the one along the grain, meaning that this may be, in certain occasions, a limiting design factor. A different type of specimen is then required, and ASTM Standard D143-94 [30] suggests the specimens presented in Figure 5.3.

(a) Radial surface of failure   (b) Tangential surface of failure.
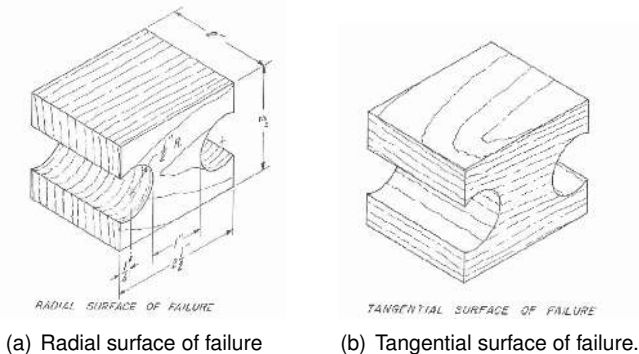
Figure 5.3: Specimens suggested in [30] for perpendicular to the grain tension testing.

It is worth noting that, even though the dimensions of the specimen are equal, the tension loading is being applied in different directions in both specimens, since the orientation of the failure surface with respect to the wood fibers orientation differs. This type of specimens allows for the determination of the maximum tensile stress, with the recognized limitation of not having a uniform stress distribution along its area. However, the fact that it is easy to build is a big advantage of this type of specimen.

Other types of specimens and testing procedures were suggested by several entities, but results yielded by testing the presented one are historically good, according to [27], without the complications that come with the usage of more complex specimens that require a more careful production process and specialized testing tools. In fact, using the specimens suggested requires the usage of a rather standard testing apparatus, as depicted in Figure 5.4.
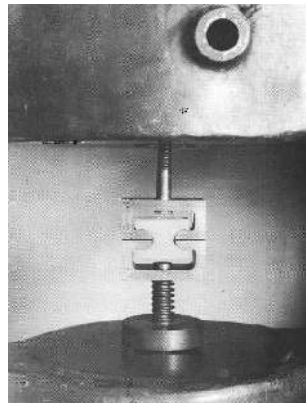
Figure 5.4: Perpendicular to the grain testing rig.

5.3 Testing Procedure

In this section, all the procedures employed for the testing of the different materials will be described, the obtained data processed and the results presented.

5.3.1 Balsa Testing Procedure

When it comes to the determination of the material properties of balsa wood, the first step is the production of adequate test specimens, according to the guidelines presented in [27] and further defined in ASTM Standard D143-94 [30].

For tension parallel to grain, the test specimen presented in Figure 5.1 (a) is recommended. This features two square cross section portions where the grips will be attached, with 25 mm side length. However, the maximum thickness found available for balsa wood was in the form of planks with 20 mm thickness. As such, a slight adaptation had to be made. The aforementioned sections of the specimen had to be scaled down in one of the directions, taking, then, a rectangular cross-section shape, with 25x20 mm. It should be noted that this adjustment had no impact whatsoever on the size of the central section of the specimen, where the measurements will be made.

In order to cut the specimen from the balsa plank, a CNC milling machine was used. To do so, a CAD model of the specimen was produced, and a drawing depicting its sides obtained. The side that was selected to maintain the suggested 25 mm length on the zones where the grips will be applied was the one where the indentations are present. A drawing of this view of the specimen was then treated in such a way that the software controlling the CNC milling machine could read it, and the cut was made. When cutting the specimen, attention was paid to ensure that the region of the plank where the cut was being produce would allow for a specimen with the wood fibers aligned with its longitudinal axis.

After performing the cutting operation, the curved surfaces of the remaining sides of the specimen were manually produced. This required a manual cutting process, using a snap-off blade, aided by drawings made in the surface of the wooden specimen, according to the CAD model and, consequently, to the suggestion made in [27]. After the desired shape was obtained, a final sanding operation was performed, in order to obtain a smooth surface, particularly in the active test section. Figure 5.5 shows the obtained test specimen after all the production procedures previously described.

Figure 5.5: Parallel to the grain produced test specimen.

Having produced the adequate specimen, the test methods available in the lab were considered. After considering the available machinery and the source of the material for the specimens, it was concluded than only the tension parallel to the grain tests could be carried out. In fact, even some changes to those test procedures had to be made, and will be discussed later. However, using the relations between properties presented in [28], it is possible to deduce the remaining properties based on the results of the parallel to the grain tests.

One of those parallel to the grain test methods used a set of cameras and image recognition software to measure the displacement of several points along the test subject, while under the tensile loading. This method is called Virtual Image Capture (VIC), also referred to as Digital Image Correlation (DIC) [31]. The VIC method uses a normal tensile testing machine, relying on the identification of points along the active test section of the specimen by a set of cameras. In order to facilitate this identification, spray paint is applied to the surface of the specimen, as depicted in Figure 5.6. The image recognition software then identifies those points and, after processing all the pictures taken throughout the test, calculates the displacement of each of those points. This method can be applied in both two and three dimensional problems. If a 2D problem is being considered, only one camera is needed while a second camera is mandatory for a 3D problem. For the case under consideration, a 2D analysis would suffice.

The VIC method relies on the quality of the pictures for the accuracy of the results. As such, special care has to be taken when focusing the camera, in order to guarantee that all the painted points are

Figure 5.6: Painted specimen.

easily visible. To begin the test, a set of five or six pictures is taken, one of them including a visible ruler (or similar), so as to calibrate the software by identifying a distance shown in that ruler. After having completed this calibration process, the remaining pictures are used to run a dummy analysis, so as to determine if the software can adequately "read" the points and their position, without "losing" them from picture to picture. This analysis is ran on a user defined section of the picture, where a finite element mesh is created and used to obtain the coordinates of the points. This mesh can be changed between analyses, should it be necessary to increase or decrease the number of elements.

After the calibration and dummy analysis are successfully completed, the actual test can begin. The frequency at which pictures are taken is chosen and defined in the VIC software. Since there is no interaction between the software running the loading machine and the VIC software, it is necessary to manually start both the tensile test and the picture capture process, as simultaneously as possible. This is one of the biggest drawbacks of this method, since an accurate synchronization of the results yielded by the VIC software and the ones from the tensile testing machine is very difficult to achieve. After the testing is finished, the processing of the pictures can take place.

The VIC method has the advantage of producing very accurate results, for a good finite element mesh and processing options, assuming superior quality pictures are being taken. However, the processing of those results can be somewhat complicated, given the synchronization problems previously discussed.

One simpler test method was then considered. This one does not use the VIC software for the measurement of the displacements on the specimen, but instead uses an Instron® uniaxial clip gauge (CAT Nº 2620-602) to do so, similarly to the recommendations of the ASTM standard D143-94 [30]. Although this is a simpler method, its results should have an adequate accuracy (although lower than the one achieved with the VIC) for the intended purposes, being the processing of data less problematic.

After analyzing the advantages and disadvantages of each of the presented test methods, and taking into account that, in order to perform the processing of the images captured by the VIC a special license was necessary, the second test method was selected.

Another change had to be made to the specimen, since the grip mechanism presented in [27] was not available. As such, that section of the specimen was cut, and it was fixed to the tensile testing

machine using standard grips, whose rough surfaces are supposed to minimize sliding of the specimen. However, special care must be taken when fixing the specimen, in order to properly fix it while avoiding crushing it.

The extensometer was then fixed to the specimen, and the test carried out using a Instron® 5566 electromechanical testing machine. A rate of motion of the movable crosshead of 1 mm/min was used, following the recommendations of ASTM standard D143-94 [30]. Figure 5.7 shows the rig used for the testing procedure, where the loading cell used had a 10 kN capacity.

Figure 5.7: Parallel to grain test of the specimen.

5.3.2 Balsa Testing Results

The measurements made by the clip gauge were recorded by the software controlling the machine, and automatically plotted together with the loading applied to the specimen. Figure 5.8 shows that plot. The raw data of the experiment was exported ito a spreadsheet for further analysis. However, for initial guidance, let this plot be considered.
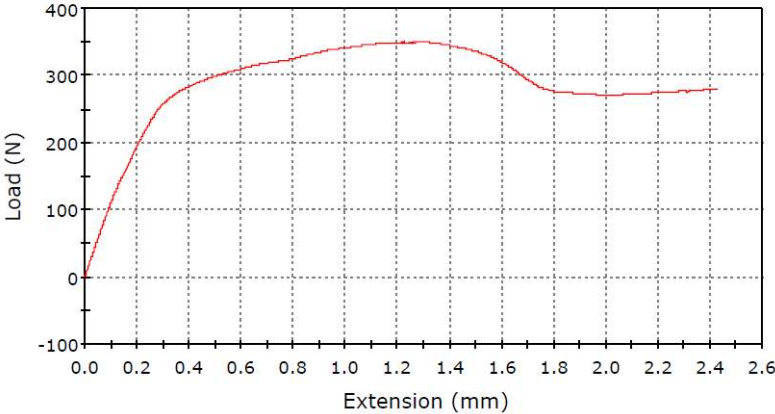
Figure 5.8: Output load vs displacement graph produced by the software.

Several aspects are worth mentioning at this point. First of all, it is important to understand that

the extension plotted in this graph is the one measured by the displacement of the overhead bar of the tension testing machine. As such, it is not particularly useful as far as data processing is concerned, since it does not correspond to the actual deformation of the active test area of the specimen. It is also worth noting that this plot does not have the usual appearance of load/displacement plots for tension tests. In fact, up until a measured extension of about 1.7 mm, the overall shape of the plot is consistent with an usual tension test. However, after this point, the load applied continues to vary with an increase in the measured extension. This suggests that deformation of the specimen may not be occurring mainly in a single region, and thus it is possible that the data registered by the clip gauge does not correspond to that of the region suffering greatest deformation.

Focusing, on this point, on the data collected by the clip gauge, it is possible to obtain the more usual stress relative to the strain plot. To do so, the nominal cross sectional area of the central zone of the specimen, where the clip gauge was applied, was considered. It is worth noting that, despite all the previously described changes that had to be made to the specimen, the actual test region was never altered in any way, and it is in complete accordance to the recommendations of [27] and ASTM Standard D143-94 [30]. As such, the cross section of the active test section is a rectangle, with dimensions of 9.5 $\times$ 4.8 mm. The values of the stress in Figure 5.9 were then obtained by dividing the applied strength by the aforementioned nominal cross-sectional area. The strain was recorded by the clip gauge.
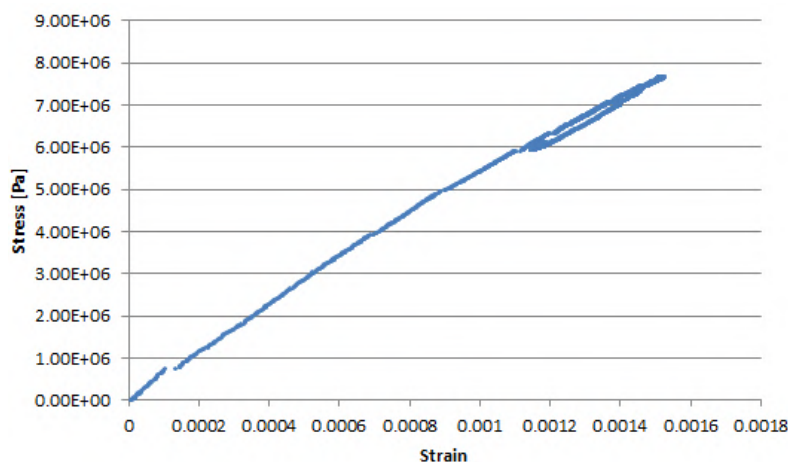
Figure 5.9: Stress with respect to strain plot for the balsa tension parallel to grain test.

Looking at Figure 5.9, a discontinuity can be observed in the early stages of the test, even before the stress reaches $1 \cdot 10^6$ Pa, accompanied by change in the slope of the graph. After that point, the slope stabilizes, although the curve is never quite straight, as would be expected of a material being deformed in its elastic domain. It can also be noted that, when reaching the highest value of stress measured in the active test area, there is actually a decrease in the strain measured by the clip gauge. This section of the plot has, however, a very similar slope to the one observed up to that point. It is almost as if the specimen was elastically recovering from the load it was subjected to. In fact, the force applied by the machine was, in fact, decreasing in that part of the test, prompting this change in the results. This decrease in force can be explained by the aforementioned fact of deformation not being focused only on the region where the clip gauge is applied. Slippage of the specimen may have also occurred. This

would explain the decrease in force measured by the machine even with the increase in displacement of the crosshead.

Considering, at this point, only the region up to where a decrease in force is registered, i.e., up to a strain of approximately 0.0015124, and obtaining a trend line of these points, it is possible to obtain an approximation for the slope of this portion of the graph, which, assuming it accurately represents the elastic region, represents the Young's Modulus of the wood in this direction. Figure 5.10 shows this plot, along with the trend line that suits the data, explicitly presented in Equation (5.3).

$$\sigma = 4.85 \cdot 10^9 \epsilon + 4.05 \cdot 10^5 \tag{5.3}$$
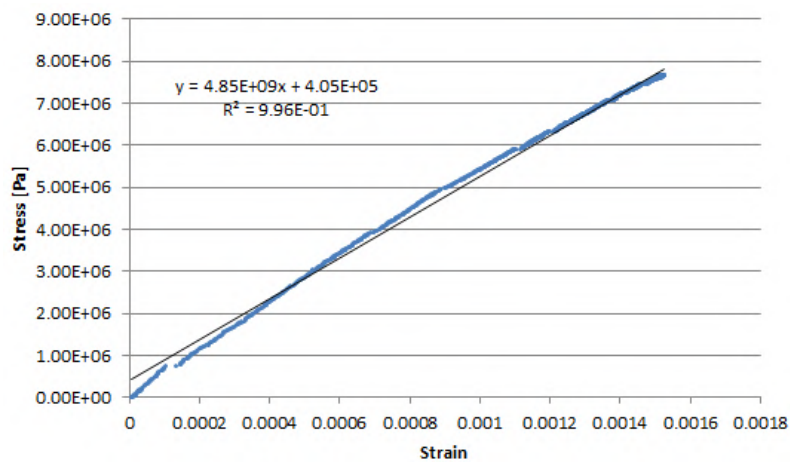
Figure 5.10: Stress with respect to strain plot for the balsa tension parallel to grain test, with the trend line.

A value of $R^2 = 0.996$ shows that the trend line satisfactorily suits the data. Ignoring the zero degree term of Equation (5.3), a value of 4.85 GPa is found for the Young's Modulus of this wood in the direction parallel to the grain. This value of the Young's Modulus is not in accordance with tabled values for balsa wood, of approximately 3GPa [28]. In fact, a higher value was obtained.

However, taking into account all the problems encountered during this test, a new one was carried out, using a second specimen, identical to the first. The testing conditions remained the same, in order to avoid discrepancies. Figure 5.11 shows the plot of the load applied to the specimen with respect to the displacement of the crosshead bar. Comparing this graph to the one obtained during the first test, several differences can be identified. In fact, this test was carried out until fracture occurred, with an increase in force up to that point. Unlike in the previous case, no decrease of applied force while increasing displacement was registered, suggesting that there was no slippage of the specimen. It is also worth noting that the fracture occurred at a internal discontinuity of the wooden specimen, a node which caused tension accumulation. This was, however, located in a region at a significant distance from the active test area.

Similarly to the previous case, a stress/strain plot was then obtained, using the strain data recorded by the clip gauge. This plot is shown in Figure 5.12. The trend line is already included in that plot.

Looking at Figure 5.12, it can be seen that up until the fracture of the specimen, an elastic behavior
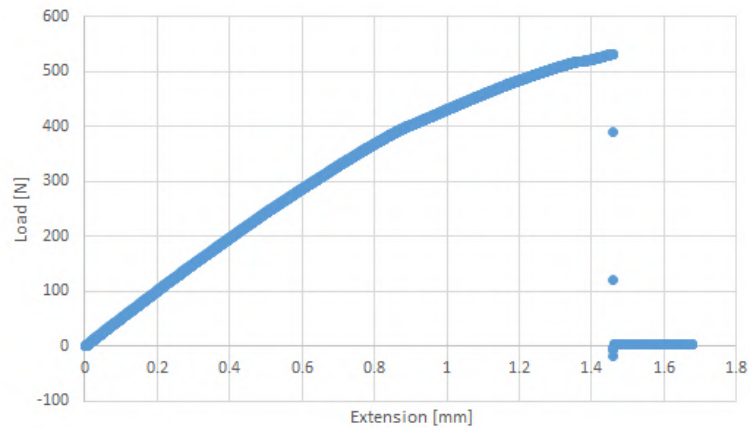
Figure 5.11: Load with respect to crosshead bar displacement for the second specimen.
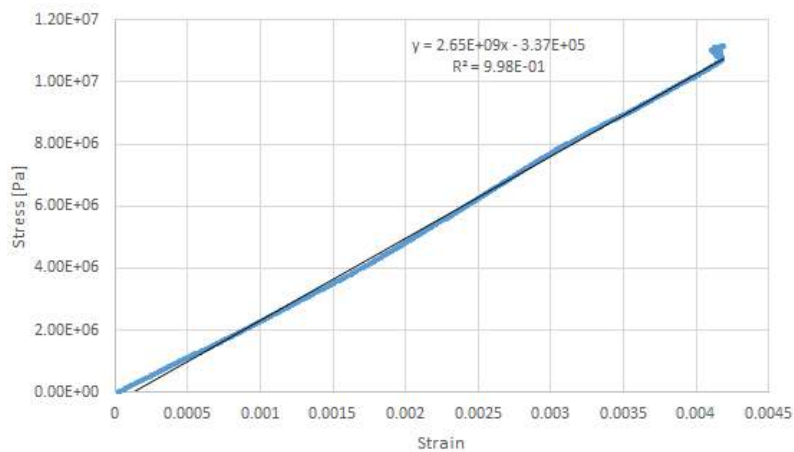
Figure 5.12: Stress with respect to strain plot for the balsa tension parallel to grain test (second specimen).

can be safely assumed. This is only possible because of the fact that fracture occurs, as previously said, in a region distant from the one where the strain is being measured. In fact, for the region where measurements are being made, the slope remains almost constant throughout the test. It can also bee seen that the trend line suits the data point very satisfactorily, with a value of $R^2 = 0.998$. Equation (5.4) explicitly presents the equation of that trend line,

$$\sigma = 2.65 \cdot 10^9 \epsilon - 3.37 \cdot 10^5. \tag{5.4}$$

According to the trend line Equation (5.4), and once again neglecting the zero degree term, a value of 2.65 GPa is found for the Young's Modulus of the balsa in the direction parallel to the grain. This value is significantly closer to the reference 3GPa commonly found.

Comparing the results of both tests, a significant difference can be observed. However, and bearing in mind the several problems identified and discussed regarding the first test, and that the second test produced much more standard results as far as the shape of the plots and the results themselves are

47

concerned, one can assume that this second test yielded more accurate results. As such, from this point forward, a value of 2.65 GPa is assumed for the Young's modulus in the direction parallel to the grain for the wood used in the construction of the model.

Knowing the value of the Young's modulus in the direction of the fiber, it is possible to deduce the remaining needed elastic properties of this particular wood, based on the ratios presented in [28]. Since wood is, as previously discussed, an orthotropic material, three principal axes are identifiable. These are the longitudinal, parallel to the fibers of the wood, and the radial and tangential, defined with respect to the growth rings of the wood. Figure 5.13 shows these axes and their orientation in a sample wood plank.
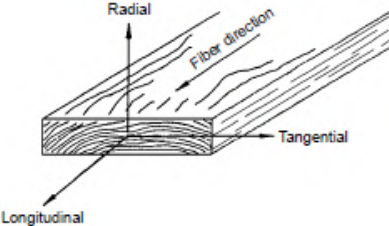
Figure 5.13: Principal axes identifiable in wood.

Table 5.2 shows the ratios presented in [28].

Elastic ratio	
E_T/E_L	0.015
E_R/E_L	0.046
G_{LR}/E_L	0.054
G_{LT}/E_L	0.037
G_{RT}/E_L	0.005

Table 5.2: Elastic ratios for balsa wood (approximately 12% moisture content).

Since the Young's modulus determined during the tests was E_L, using the ratios previously presented, obtaining the remaining elastic properties is a straightforward task. Table 5.3 contains all the necessary elastic properties of the tested balsa wood.

Elastic property		Poisson's Ratio	
E_L	2,650 MPa	μ_{LR}	0.229
E_T	39.75 MPa	μ_{LT}	0.488
E_R	121.90 MPa	μ_{RT}	0.665
G_{LR}	143.10 MPa	μ_{TR}	0.231
G_{LT}	98.05 MPa	μ_{RL}	0.018
G_{RT}	13.25 MPa	μ_{TL}	0.009

Table 5.3: Elastic properties of the tested balsa wood. Table 5.4: Poisson's ratio for balsa wood (approximately 12% moisture content).

As for the Poisson's ratios along the different axes, [28] provides the values included in Table 5.4, for

balsa at approximately 12% moisture content. Tests were not carried out for this particular property, due to the equipment limitations previously discussed.

All the elastic properties of balsa needed for the computational model are now known.

5.3.3 Carbon Tube Testing Procedure

Having presented the procedure carried out for the determination of the material properties of the balsa wood used in the model, the carbon tube was then considered.

It was assumed that the material could be considered isotropic. Since these carbon tubes are pultruded, it is a fact that the fibers are generally oriented in a longitudinal direction. However, since the loading of the tube will essentially consist of bending, or tension/compression, the longitudinal direction is the predominant one, and thus the assumption of it being isotropic is justified. It is also assumed that this material is sufficiently elastic for the assumption that the flexural modulus of elasticity is equal to the tension modulus of elasticity to remain valid.

Since the tube was acquired in its final form, it is not possible to produce a specimen and carry out a standardized test such as with the balsa wood. As such, a testing procedure had to be developed.

Two options were considered at this point. At first, a tension test was considered. However, due to the fact that this tube had a hollow cross-section, this test was not adequate. As such, a bending test was chosen alternatively. This test considers a simple cantilever beam (in this case, the carbon tube), loaded at its free end. Measuring the displacement of the free end and knowing the dimensions of the cross-section and span of the "beam", it is possible to determine the value of the Young's Modulus, according to Equation (4.14).

In order to carry out this test, a support for the tube was produced from wood conglomerate. It is worth noting that this support was built taking into consideration the need to support the complete model later on, and thus also supports the spar. A ruler was fixed vertically, near the free end of the tube, and was used to measure the displacement of this end. Figure 5.14 shows the setting used for these tests. A mark was drawn on the back of the ruler for the unloaded tube (reference) and for each loading, and a caliper rule used to measure the distance between the mark for each loading and the reference.

Three different weights were used, two smaller and a larger one. They were previously weighed in a digital scale. The obtained values are presented in Table 5.5. They were then fixed at the free end as illustrated in Figure 5.15. A screw was inserted in the free end of the tube, in order to prevent the weights from sliding and falling when the tube bent.

Figure 5.14: Setting used for the testing procedure of the carbon tube.

Figure 5.15: Carbon tube with a weight at its free end.

	Mass [g]
Small weight nr. 1	133.47
Small weight nr. 2	133.27
Large weight	621.79

Table 5.5: Weights used for the testing procedure of the carbon tube.

It was decided that a set of values was to be obtained, instead of a single result, in order to minimize the error on the results. As such, different combinations of weights and tube spans were used, and the values registered.

5.3.4 Carbon Tube Testing Results

Firstly, a span of 360 mm was considered. For this span, it was possible to apply three different loads, consisting of weight nr. 1, weight nr. 1 together with weight nr. 2, and the large weight alone. Then, a 500 mm span was chosen. This span did not allow the testing with the large weight, since the displacement of the free end would cause the weight to touch the table, and thus the measured results would not be valid. As such, only the loading cases of weight nr. 1 and weight nr. 1 and 2 together were applied. The free end displacement was measured for each case, and its value registered.

Load [gf]	Displacement [mm] (360 mm span)	Displacement [mm] (500 mm span)
133.47	23	58.4
266.74	44.5	111.5
621.79	101	——

Table 5.6: Free end displacements for each span/loading combination.

Looking at Equation (4.14), reproduced here as Equation (5.5), it can bee sen that the values of P and l are already known, such as y, the displacement measured at the x coordinate, which, in this case, corresponds to the free end ($x = l$). A value of $g = 9.81\ m/s^2$ was considered when converting mass to force.

$$y = \frac{Px^2}{6EI}(3l - x) \tag{5.5}$$

As for the area moment of inertia of the cross section of the tube, it is obtained according to Equation (5.6), where D is the outer diameter and d the inner one, measuring 4 and 3 mm respectively, in this situation,

$$I = \frac{\pi}{64}(D^4 - d^4). \tag{5.6}$$

Using all known and measured values, it is then possible to obtain the values of the Young's Modulus for each span/loading combination, presented in Table 5.7.

Taking into account that the material was assumed to be isotropic, it was expected that the values obtained for the Young's modulus should be independent from the conditions of the test regarding the loading and the span. However, errors are present in the procedure, originating not only from the measurements but from the testing setup itself. In fact, the marks drawn on the back of the ruler used for

50

Load [gf]	Young's Modulus [GPa] (360 mm span)	Young's Modulus [GPa] (500 mm span)
133.47	102.96	108.64
266.74	106.35	113.72
621.79	109.23	——

Table 5.7: Young's Modulus determined for each span/loading combination.

measuring the displacement of the free end might not have coincided with the center of the cross section and the ruler as well as the support might not have been completely vertical, despite all efforts. However, it can be seen that the values obtained for the Young's modulus do not present a large variation between the several span/loading scenarios, and thus it may be considered that the previously presented error sources did not have a significant influence in the test results.

Taking into account the results presented in Table 5.7, an average value of those results may be obtained and considered to be the value of the Young's modulus of this particular carbon tube. That average is 108.18 GPa. This value is rather close to that which is presented by several suppliers, of about 125 GPa for the flexural modulus of elasticity [32], which, as discussed earlier, corresponds to the tension modulus of elasticity under the assumption of elastic behavior of the tube.

5.3.5 Fiberglass Composite Testing Procedure

Unlike the previously tested specimens, which were composed of a single material, when testing a composite the problem of it being constituted by several materials with distinct properties arises. However, taking into consideration that, for the purpose of building the model, a single layer of fiberglass will be bonded to the balsa parts by means of an epoxy resin, a test will be carried out to determine the properties of the composite as a whole, not considering the individual properties of each component.

For the purpose of this test, a specimen was created using the fiberglass fabric and the epoxy resin used in the model. It is worth noting that due to the fact that these composites are handmade, it is impossible to create two perfectly equal specimens. The quantity of resin added may vary slightly, the fabric itself may not be completely homogeneous throughout its area, and many other limitations exist. However, special care was taken to the orientation of the fibers. This last point will be discussed further ahead. Due to this impossibility to obtain two perfectly equal specimens, it is also hardly possible to guarantee that the composite applied to the wooden parts of the model will have the exact same properties as the one tested. However, for the purpose of this work, let us assume that the properties determined in this section apply to all composite parts.

Since, as presented further ahead in this document, only a layer of fiberglass will be added to each side of the wooden parts, the specimen created will also be comprised of a single layer of fibers imbued in epoxy resin. Due to the limitations imposed by such a thin specimen, only a tension test can be carried out, allowing for the determination of the Young's Modulus in specific directions, according to the orientation of the fibers.

The composite built consisted of a rectangle, with a length of 100 mm and a width of 20 mm. This specimen was obtained by a hand lay-up process, and so its thickness could only be determined after

the drying and curing process were finished. A rectangular cross section with a measured thickness of 0.10 mm is considered constant throughout the specimen. Since this would be too thin for the grips of the testing machine to handle, several layers of fiber were added to create 2 grips, with a 1 mm thickness. According to the ASTM standard D3039 [33], a 2 mm/min test speed was chosen. Figure 5.16 shows the specimen built.

Figure 5.16: Composite specimen (after testing was performed).

As previously discussed in Section 4.2.3, a layer of composite made of a matrix and fibers with a known orientation can be considered orthotropic. In this specific case, the fibers used came in the form of a fabric, where two directions of fiber orientation can be identified, perpendicular to one another. Since a tensile test will be performed, these fibers will be oriented in the directions parallel and perpendicular to the loading. By doing so, when obtaining the Young's Modulus for the direction parallel to the loading, the one in the direction perpendicular to it is known to be equal.

The same Instron$^{\circledR}$ clip gauge used previously was applied to the surface of the specimen. However, due to how thin the specimen was, applying the clip gauge caused it to bend slightly on the edges. After carefully manipulating it, that bending effect was minimized.

5.3.6 Fiberglass Composite Testing Results

The test was carried out until fracture of the specimen occurred, using the Instron$^{\circledR}$ 5566 testing machine. A plot of the displacement of the crosshead bar (labeled extension by the data recording software) relative to the force applied to the specimen was obtained, presented in Figure 5.17.
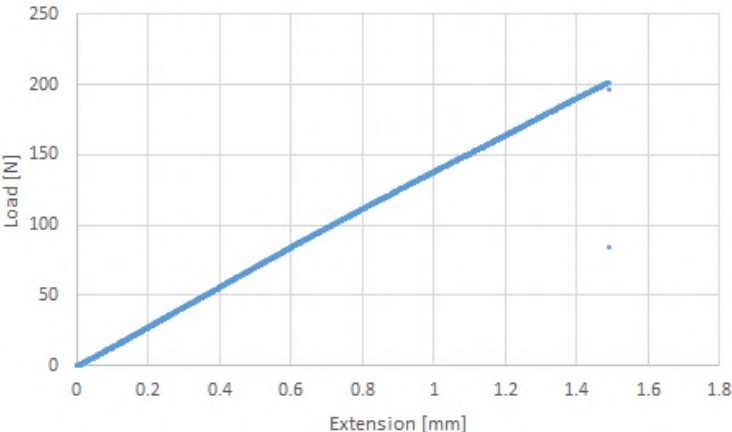
Figure 5.17: Load with respect to crosshead bar displacement for the composite specimen.

Looking at Figure 5.17, one can identify the moment of fracture, at about 1.5 mm of displacement of the crosshead bar, for a loading of approximately 200 N.

Considering, at this point, the strain data recorded by the clip gauge, it is possible to obtain a stress versus strain plot, up until the moment of fracture. To do so, the nominal area of the cross section ($20 \cdot 0.1$ mm^2) was considered to obtain the stress values.
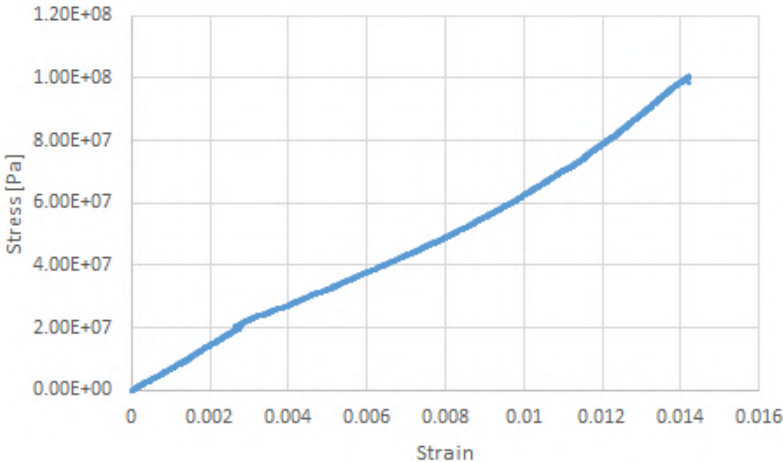
Figure 5.18: Stress vs. strain plot for the composite specimen, up to fracture.

Closely looking at the plot shown in Figure 5.18, a first change in the slope of the graph can be identified at a strain of 0.0027. After this point, the graph becomes a curve, and as such the slope is continuously changing. Bearing that in mind, the elastic region can be assumed to be that first linear region, where the slope remains unchanged. Plotting only the test data relative to that portion of the graph, it is possible to obtain a trend line, and consequently, an estimate for the Young's modulus of the composite in the direction of the loading (which, as discussed earlier, was made to be one of the directions of the fibers when building the specimen).
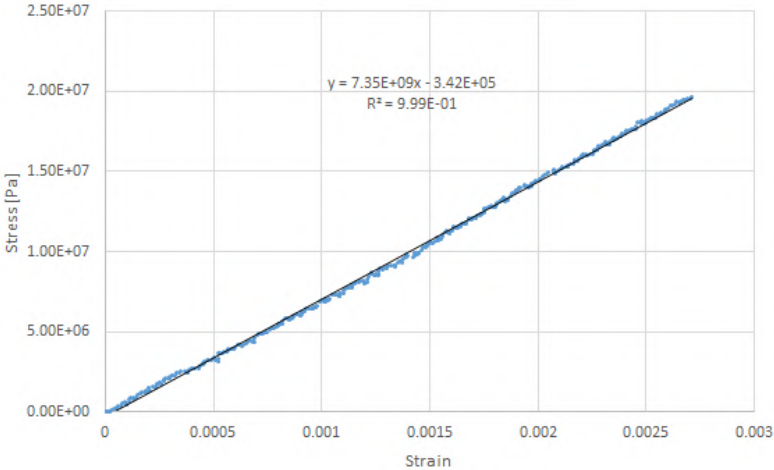
Figure 5.19: Stress vs. strain plot of the elastic region (composite specimen).

Figure 5.19 already includes the trend line that fits the data for the elastic region identified above, explicitly presented in Equation (5.7)

$$\sigma = 7.35 \cdot 10^9 + 3.42 \cdot 10^5. \tag{5.7}$$

Looking at that equation, and neglecting the zero degree term, a Young's Modulus of 7.35 GPa is extracted from this test.

Looking back at Figure 4.10, and taking into account that in this specific case, the fibers are perpendicularly woven in a fabric, the value of the Young's Modulus for the x_1 and x_2 directions is the one determined with this testing procedure. As for the Poisson's Ratio, since it was not possible to determine it experimentally, a value of 0.29, suggested by most manufacturers of pre-cured layers of fiberglass composites was used.

5.4 Summary of Results

The results obtained in this chapter are summarized in Table 5.8. These are all the elastic properties required to perform the FEA. For the case of isotropic materials, only the Young's Modulus and Poisson's ratio are presented.

Elastic property	Balsa wood	Carbon tube	Fiberglass composite
E [MPa]	-	108,180	7,350
E_L [MPa]	2,650	-	-
E_T [MPa]	39.75	-	-
E_R [MPa]	121.90	-	-
G_{LR} [MPa]	143.10	-	-
G_{LT} [MPa]	98.05	-	-
G_{RT} [MPa]	13.25	-	-
μ	-	0.1	0.29
μ_{LR}	0.229	-	-
μ_{LT}	0.448	-	-
μ_{RT}	0.665	-	-
μ_{TR}	0.231	-	-
μ_{RL}	0.018	-	-
μ_{TL}	0.009	-	-

Table 5.8: Summary of the elastic properties determined in this chapter.

Chapter 6

Validation of the Numerical Models

In the previous chapter, the properties of the several materials included in the wing model were experimentally determined. At this point, it is relevant to perform a validation of the tests carried out using CATIA®'s Generative Structural Analysis workbench. The tests will be modeled and solved numerically, using the previously determined properties, and the results compared with the actual experimental ones.

For each material test, a control variable will be selected to perform a comparison between the experimental and numerical tests. This process allows for a fine tuning of the numerical model, should the modeled tests yield results far different from the ones presented in Section 5.3. By doing so, one guarantees that the input values of the material properties are as accurate as possible, in order to obtain, at a later stage, a numerical model that accurately represents the built prototype.

For each test, a discussion of the mesh parameters will be carried out, alongside a convergence test. The adequate boundary conditions for each test will be selected and applied to the model. A discussion regarding eventual simplifications and their impact on the model will be presented, whenever found necessary.

6.1 Balsa Wood Model

Taking into consideration the testing procedure carried out for the determination of the properties of the balsa wood, special attention must be taken to some details when creating the numerical model that represents the test.

Firstly, only the central section of the specimen will be modeled. By doing so, attention will be focused only in the region where the clip gauge was applied, and thus the more accurate data gathered by this sensor will be used. Also, since in the actual test fracture occurred due to an imperfection on the inner structure of the wood, if one were to use the displacement of the crosshead bar to compare the results yielded by the numerical analysis to those achieved in the test, a greater degree of error could be introduced, since that imperfection would not be taken into account in the model.

Bearing that in mind, a CAD model of the central section of the specimen was created, according to the dimensions provided in [27] and ASTM Standard D143-94 [30], and is presented in Figure 6.1.

Using CATIA®'s Generative Structural Analysis workbench, the boundary conditions were applied to that model. One of the ends was clamped, while the other remained free. Since, in the real life test, the force is applied in a region rather distant from the modeled section of the specimen, a normal, uniformly distributed force acting on the surface of that free end of the model was added.

In order to compare the results of the numerical model to the ones of the experimental test, a load applied during the real test will be selected, and the corresponding strain measured using the clip gauge considered.

Let us consider an applied load of 200.08 N, with which a strain of 0.00184 was obtained. Taking into account the initial length of the modeled central region of the specimen of 63 mm, and considering it as the reference length, a displacement of $0.00184 \cdot 63 = 0.116$ mm is expected.

Special care was taken when assigning the material properties to the model. The orientation of the fibers on the specimen was carefully checked, and a local coordinate system accordingly created in the CAD model of the part. The material properties determined in Section 5.3.1 were then applied taking into account that local coordinate system.
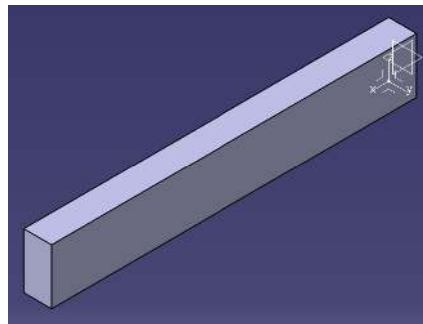
Figure 6.1: CAD model of the specimen test region.

Before delving into a comparison of results, it is necessary to carry out a small convergence study of the mesh. Tetrahedron quadratic elements were selected. Several different meshes were applied to the part. At first, a very coarse mesh was applied, followed by increasingly finer meshes. Table 6.1 shows the parameters used for obtaining those meshes. Using these mesh parameters, the number of elements obtained for each mesh is shown in Table 6.2, which also includes the value obtained for the maximum displacement.

It can bee seen that the values of the maximum displacement are converging, with slight changes in the order of the hundredth of millimeter, without a significant impact on the time required for the computation. However, given the simplicity of this case, a global refinement of the mesh such as is being done may not be the best. In fact, the more problematic region is the one where the distributed force is applied, particularly in the corners. This is particularly well visible in Figure 6.2. It can be seen that the nodes of the elements on the edges of that surface of the specimen are pulled further from where the central region is. This naturally occurs. However, the four corners act as stress concentration regions, and thus their deformation is even larger.

In order to try to capture the behavior of this region as accurately as possible, a local refinement

	Mesh 1	Mesh 2	Mesh 3
Global parameters			
Size	2 mm	0.75 mm	0.5 mm
Absolute sag	0.5 mm	0.5 mm	0.25 mm
Quality parameters			
Criteria	Shape	Shape	Shape
Jacobian	0.3	0.3	0.3
Warp	60	60	60
Other parameters			
Geometry size limit	0.1 mm	0.1 mm	0.1 mm
Mesh edges suppression	0.2	0.2	0.2
Minimum size for sag specs	0.494 mm	0.2 mm	0.2 mm

Table 6.1: Mesh parameters used for the balsa specimen analysis.

	Mesh 1	Mesh 2	Mesh 3
Number of elements	2,355	27,465	75,930
Maximum displacement [mm]	0.144	0.134	0.126

Table 6.2: Number of elements of each mesh used on the balsa specimen analysis, and maximum displacement obtained with each mesh.
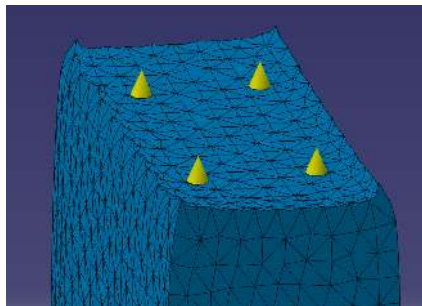
Figure 6.2: Deformed shape of the region where the force is applied, obtained with the locally refined mesh.

of the mesh was applied, while using the global parameters employed to obtain mesh 2. Mesh 2 was already satisfactory for the overall part, and this local refinement now applied allowed for a reduction in computational resources needed, when compared to the global mesh refinement used to obtain mesh 3. A local mesh size of 0.15 mm was imposed on the face where the force is applied. A finer mesh should minimize the overall effect seen in Figure 6.2, and so produce better results as far as the maximum displacement measured in those regions is concerned. A final mesh with 47363 elements was the result.

Figure 6.3 shows the deformed shape in that region, using the new mesh.It can be seen that the entire region is more uniformly shaped. The four corners still stand out as the points where maximum deformation is measured, but much less than before.

Focusing, now, on the value obtained for the displacement, Figure 6.4 shows that a maximum displacement of 0.116 mm is calculated, measured near the edges of the surface where the force is applied.
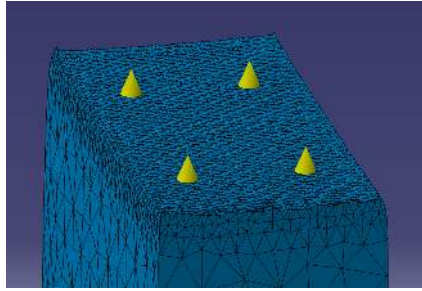
Figure 6.3: Deformed shape of the region where the force is applied, obtained with mesh 3.
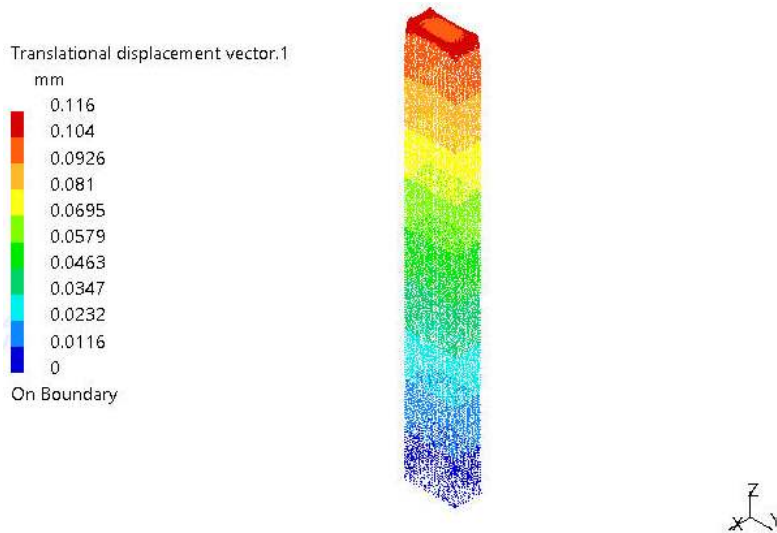
Figure 6.4: Deformation of the specimen under the selected loading.

Comparing this to the results obtained in the experimental test, a perfect match is obtained. It is then safe to assume that the numerical model accurately depicts the behavior of the specimen, leading to the conclusion that the determined balsa wood properties are adequate and that no tuning of their value is necessary.

6.2 Carbon Tube Model

In order to create a model of the test carried out for the determination of the properties of the pultruded carbon tube, a CAD model of the tube was created, and is shown in Figure 6.5. To minimize the error of the analysis, the span/loading pair which yielded the value of the Young's modulus closest to the final average of 108.18 GPa was chosen. As such, a tube with a length of 500 mm was modeled, and a loading of $0.13347 \cdot 9.81 = 1.309$ N applied. It was considered that this force was acting on a single point, on the top surface of the carbon tube.

Using CATIA®'s Generative Structural Analysis, the boundary conditions were applied to the model. One end of the tube was clamped, while on the other end a force was applied on a point previously added to the CAD model. When meshing the part, this point was forced into the overall mesh. Tetrahedron quadratic elements were used.
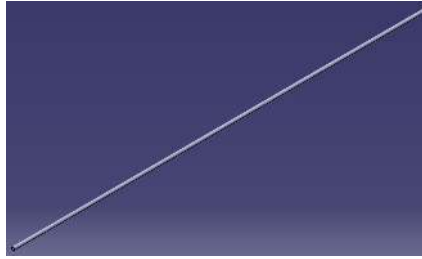
Figure 6.5: CAD model of the specimen tested carbon tube.

At this point, a convergence study was carried out. Different meshes were applied to the part, the problem solved with each of them, and the results analyzed. Table 6.3 shows the mesh parameters used to obtain the different meshes.

	Mesh 1	Mesh 2	Mesh 3
Global parameters			
Size	1 mm	0.75 mm	0.5 mm
Absolute sag	1 mm	0.2 mm	0.2 mm
Quality parameters			
Criteria	Shape	Shape	Shape
Jacobian	0.3	0.3	0.3
Warp	60	60	60
Other parameters			
Geometry size limit	0.1 mm	0.1 mm	0.1 mm
Mesh edges suppression	0.2	0.2	0.2
Minimum size for sag specs	3.908 mm	0.2 mm	0.2 mm

Table 6.3: Mesh parameters used for the pultruded carbon tube analysis.

The global split option was selected for all the meshes used for the tube, to obtain more elements along the thickness of the tube. Taking into account the mesh parameters presented above, the final number of elements of each mesh is presented in Table 6.4.

	Mesh 1	Mesh 2	Mesh 3
Number of elements	74054	134774	290721

Table 6.4: Number of elements of each mesh used on the pultruded carbon tube analysis.

The mesh was refined sequentially to evaluate the impact of that refinement process on the results of the analysis. The problem was solved for each of the meshes, and the displacement of the free end was used to perform the convergence study.

	Mesh 1	Mesh 2	Mesh 3
Displacement of the free end [mm]	57.6	58.6	58.6

Table 6.5: Displacement of the free end obtained with each mesh.

As one can see by analyzing Table 6.5, by refining the mesh, the value obtained for the maximum

displacement measured at the free end converges. In fact, it can be seen that further refinement of the mesh beyond the number of elements of mesh 2 does not prove advantageous, since the increase in computational time needed to solve the problem is not compensated by a more accurate result. As such, mesh 2 was selected and used for this analysis. Figure 6.6 shows a zoomed in view of the mesh near the free end of the tube, including the imposed point where the force is applied.
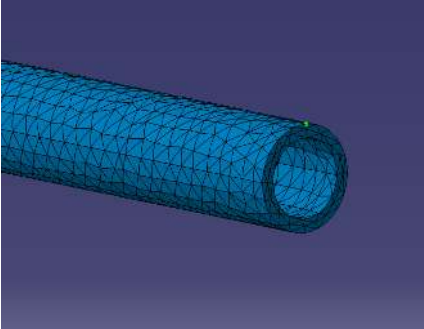
Figure 6.6: Detailed view of the mesh used in the analysis of the carbon tube.

Proceeding now with the validation of the material properties determined for the pultruded carbon tube, looking at Figure 6.7 one can see that the value of the displacement (58.6 mm) of the free end of the tube is very similar to the one measured during the actual testing procedure, of 58.4 mm.
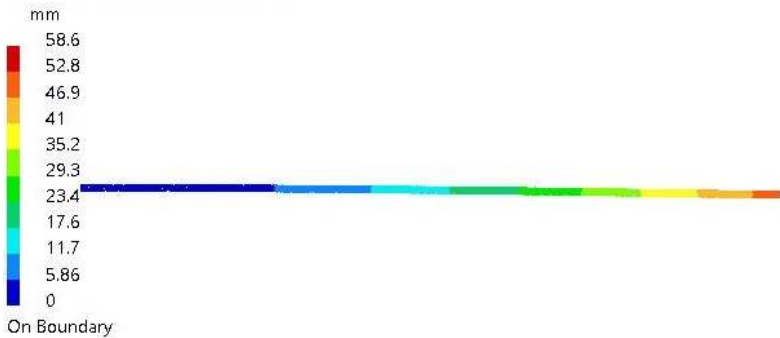
Figure 6.7: Deformed shape of the carbon tube.

The disparity between the results obtained with the experimental test and with the finite elements analysis is of only 0.34%. Given that this value is extremely low, it can be safely concluded that the numerical model accurately predicts the real life results of the test. Taking that into account, there is no need to tune the values of the material properties previously determined for the pultruded carbon tube.

6.3 Fiberglass Composite Model

This is, perhaps, the most problematic of the three testing procedures to perform validation on due to the dimensions of the specimen, particularly its extremely reduced thickness.

As with the previous validations exercises carried out, firstly a CAD model of the specimen was obtained. Similarly to what was done in the validation of the balsa specimen, only the active test region

of the specimen was modeled, as illustrated in Figure 6.8, meaning that the grips were disregarded for simplicity.
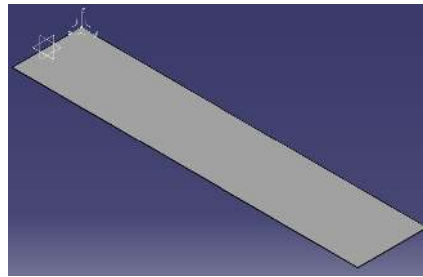
Figure 6.8: CAD model of the tested fiberglass composite.

It was then time to obtain a finite element mesh for the modeled part. This is where the difficulties with this validation process started. Due to how thin the specimen was, a three dimensional mesh using tetrahedron elements was not suited for the validation problem when considering orthotropic material properties. In fact, using it led to difficulties in obtaining results that satisfactorily modeled the experimental test, with significant warping of the cross section, even though the loading was perpendicular to it.

Bearing in mind those issues, a two dimensional mesh was considered. In fact, due to how thin the specimen was, this was a valid assumption, and should not introduce a great level of uncertainty in the analysis. This type of mesh can be obtained using triangular or quadrangular elements. Considering the geometry of this specific part, it can be seen that quadrangular elements better suit it. As such, using CATIA®'s Advanced Meshing Tools workbench, it was possible to easily obtain different quadrangular meshes for the part.
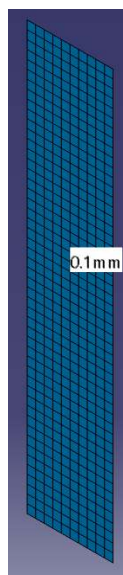
Figure 6.9: Sample 2D mesh applied to the fiberglass composite.

Taking into account that a 2D mesh is being used, the usual 3D properties used in CATIA®'s Generative Structural Analysis workbench in the previous cases do not apply. These properties include the

material elastic properties. As such, at this point, a simplification had to be made. Since the version of CATIA® being used does not support 2D orthotropic material properties in the structural analysis workbench, a simplification had to be adopted. The material was considered to be isotropic, meaning that it had a constant value for the Young's Modulus in all directions. Given the fact this is no longer a three dimensional problem, this means that axis x_3 of Figure 4.10 is not being considered, and neither are the properties of the composite along this direction. As for the other two directions, x_1 and x_2, it was discussed in Section 5.3.6 that, due to the fact that the fiberglass fabric used was woven with fibers perpendicularly oriented with respect to each other, the value obtained for the Young's Modulus in one of the directions of the fiber would be equal to that of the other direction. bearing in mind all these factors, the assumption of two dimensional isotropy in this case is not entirely inadequate.

Considering this simplification, the specimen was modeled as a simple surface, with no thickness. When assigning the 2D properties to this surface, the thickness was defined to be the 0.1 mm of the actual specimen, as modeled previously in 3D. Using quadrangular quadratic elements, different meshes were obtained, based on the size of the elements, and a convergence study was performed. A loading of 20 N was considered, for which, according to the data gathered during the actual test, a maximum displacement of 0.147 mm was expected. This loading was applied on one of the 20 mm edges of the surface, while the other was clamped. Table 6.6 shows the different element sizes adopted for each mesh, and the resulting total number of elements, as well as the maximum displacement obtained.

|	Mesh 1	Mesh 2	Mesh 3	Mesh 4
Element size [mm]	4	2	1	0.5
Number of elements	125	500	2000	8000
Maximum displacement [mm]	0.145	0.142	0.139	0.138

Table 6.6: Convergence study for the 2D mesh applied to the composite specimen model.

It can be seen that, even though the number of elements used increased significantly from mesh 1 to mesh 4, only a discrepancy of 0.007 mm is registered. It can then be assumed that the solution is slowly converging. From a computational efficiency point of view, mesh 2 can be selected, since it already yields accurate results. Figure 6.10 shows the deformed shape of the composite specimen under the 20 N load. The maximum displacement obtained with this numerical model of 0.142 mm is significantly close to the one that was measured in the experimental test, with a discrepancy of only 0.005 mm, corresponding to a relative error of 3.40% between both results. This suggests not only that the value determined for the Young's modulus in Section 5.3.6 is accurate, but also that the simplification of considering 2D isotropy for this specific specimen was valid.

Having validated the results of the test with the aforementioned simplification, an attempt was made at applying a 3D mesh to the model of the specimen, while maintaining the assumption of isotropic behavior, in order to bypass the problems with a two-dimensional mesh when considering orthotropic properties, as well as to avoid compatibility issues between 2D and 3D meshes further ahead. Several meshes, with different levels of refinement each, were considered, using tetrahedron quadratic elements. The parameters used to obtain those meshes, as well as the total number of elements of each, are pre-
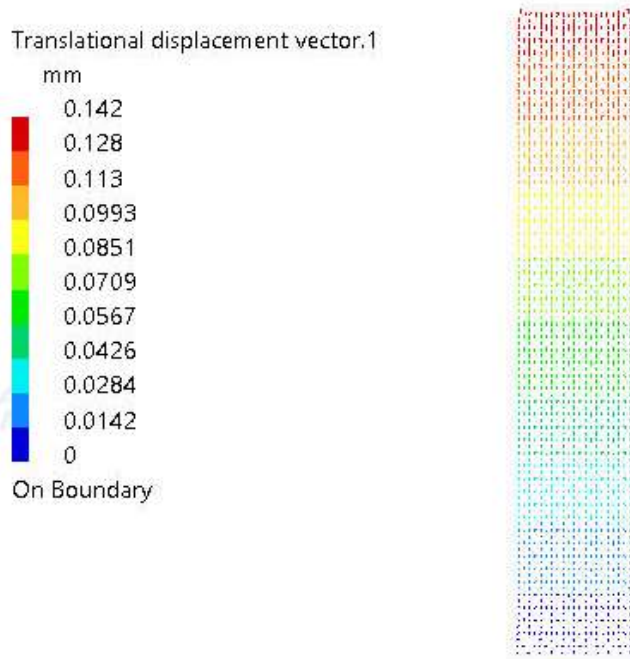
Figure 6.10: Deformed shape of the composite specimen (2D mesh 2).

sented in Table 6.7. The global split option was not selected in this case, since the meshes obtained with it activated produced computational problems regarding memory usage, leading to inaccurate results.

Table 6.8 shows the maximum displacement obtained when using each of the aforementioned meshes.

	Mesh 1	Mesh 2	Mesh 3
Global parameters			
Size	1 mm	0.75 mm	0.5 mm
Absolute sag	0.5 mm	0.5 mm	0.5 mm
Quality parameters			
Criteria	Shape	Shape	Shape
Jacobian	0.3	0.3	0.3
Warp	60	60	60
Other parameters			
Geometry size limit	0.1 mm	0.1 mm	0.1 mm
Mesh edges suppression	0.2	0.2	0.2
Minimum size for sag specs	0.783 mm	0.783 mm	0.2 mm
Number of elements	11978	22518	47919

Table 6.7: Mesh parameters used for the 3D mesh of the composite specimen.

	Mesh 1	Mesh 2	Mesh 3
Maximum displacement [mm]	0.142	0.146	0.139

Table 6.8: Displacement obtained with the 3D meshes, considering isotropic behavior.

Similarly to what occurred in the two dimensional case previously considered, it can be assumed

63

that the solution is converging, since only changes in the order of the thousandth of millimeter are registered. Considering the results obtained with mesh 3, depicted in Figure 6.11, since it has the highest number of good elements according to the quality criteria, it can be seen that the numerical model accurately predicts the displacement measured during the experimental test, with a discrepancy of only 0.008 mm, which corresponds to a relative error 5.44%. It can then be assumed that using a three-dimensional mesh to model this specimen is acceptable, if the simplification of considering the material to be isotropic is still made. Taking all this in consideration, no fine tuning of the composite properties was made.
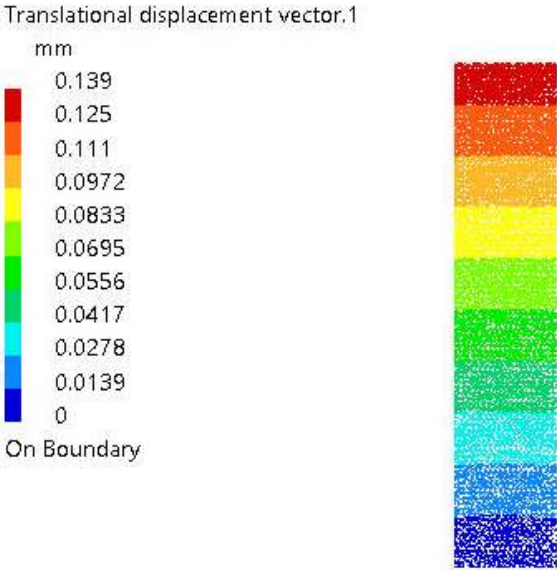
Figure 6.11: Deformed shape of the composite specimen (3D mesh 2).

Chapter 7

New Wing Design

In this chapter, a new structural design of the LEEUAV wing will be discussed. Its main features will be described, along with its advantages and disadvantages. This structural design will serve as a guideline for the prototype that will be built later on. The solar cells will not be included in this structure, and no considerations regarding their inclusion will be made.

7.1   Wing Configuration

As previously discussed, one of the main aspects to be taken into account while designing a structure for this UAV is the need for it to efficiently accomplish its mission goals. Taking that into account, if a lighter structure is obtained, without great impact to its structural behavior, a more energy efficient aircraft would arise. It is important to identify the features of that wing that can be changed in order to improve it.

First of all, as discussed in Section 2.3, a D-box with a foam core was used in that wing. If that foam core is removed without a significant cost to the strength of the wing, a reduction in the overall structural weight can be achieved.

Another change that can be implemented is concerned with the ribs. The existing wing uses balsa ribs for the majority of the span, except for those where different panels of the wing connect, where plywood was used in order to reinforce the structure. However, plywood is much heavier than balsa, and so that reinforcement of the structure comes at a great cost as far as weight is concerned. If the ribs were to be reinforced with a fiberglass composite, it would be possible to obtain a sufficiently rigid structure without such a great impact on its overall weight. If all ribs are reinforced, it is even possible to reduce the number of ribs placed along the span, compensating for the weight added with the inclusion of the fiberglass fibers and the resin.

As far as the actual structure is concerned, the first considered layout was the non-sheeted presented in Section 2.4.2. A first version of this structure was also used when describing the general CAD modeling process in Section 3.3.

This is a rather straightforward structural design. A simple rectangular cross-section beam was used

65

as the main spar, with a thickness of 6 mm and a height of 20 mm. This spar, illustrated in Figure 7.1, although simple in design, has the benefit of being lightweight, and having a good mechanical behavior as far as bending is concerned. However, one of the drawbacks of the rectangular cross section is a poorer response when subjected to torsion, when compared to I or even T shaped cross-sections with the same area. This main spar goes up to the point where the tapered section of the wing begins, at 1400 mm from the wing root.
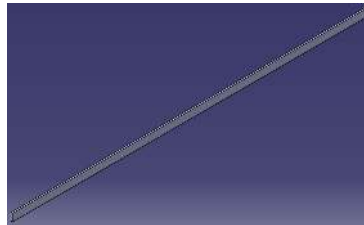
Figure 7.1: Main spar modeled in CATIA®.

The wing is still built to be divided into three panels, although the point where they are connected is different: a central panel, consisting of the non tapered portion of the wing, up to 1400 mm in the spanwise coordinate, the other two being the tapered sections in each half wing. The two smaller panels contain an independent spar, which connects to the central panel by means of a stronger rib, to which a connecting element is added in order to provide support for the outer panel spar, and thus transmit the forces from it to the main spar of the central panel. This connecting element will add significant weight to the wing, but its inclusion is necessary in order to split the wing, and thus allow for an easier transportation. Figure7.2 shows the left-half wing, where the connecting elements can be seen at the interface between the central and outer panels.
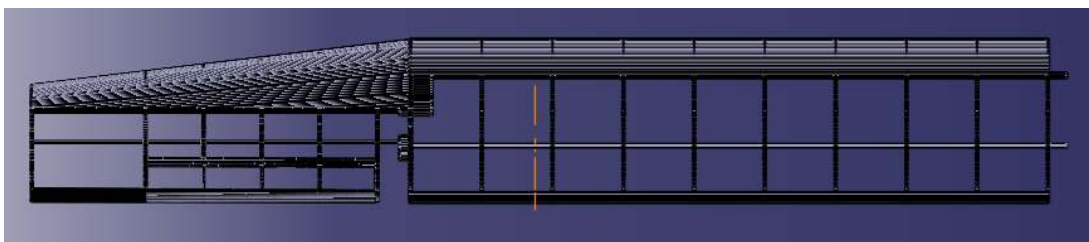
Figure 7.2: Left half-wing CAD model, split at 1440 mm span.

As for the ribs, they are 3 mm thick, made out of balsa wood. A reinforcement with fiberglass is considered, as previously discussed, adding stiffness to the structure at the cost of an increase in structural weight. Its inclusion will be debated when building the prototype for the wing. The rib at the interface between the central and outer panels is to be made thicker than the others, at 5 mm, and possibly reinforced with a composite material including stronger fibers, so as to withstand the force caused by the connection of the panels, as discussed previously. A central hole with a 10 mm radius is made in the central panel ribs. This feature serves the purpose of allowing for the passage of wires from the actuators and solar panels, but it also contributes towards a reduction of the weight of each rib. Figure 7.3 shows a rib containing this hole, as well as the ones used for connecting it to the spar and

carbon tube. This hole becomes smaller, with a 5 mm radius, for the last rib of the central panel and for the ribs of the outer panels, up until the second to last aileron rib.

Figure 7.3: Rib CAD model, with the holes for the assembly to the spar, carbon tube, and passage of cables.

The rib spacing is not homogeneous throughout the span. At the central panel, a spacing of 150 mm is used between ribs, with the first rib being placed a 40 mm distance from the wing root. A total of ten ribs are placed on this section of the wing. In the tapered region of the wing, the first rib is placed closer to the final rib of the central panel, so that a smaller gap exists at the connection between those two regions of the wing. An offset of 67.2 mm is considered between those ribs. A spacing of 122.3 mm is used between the ribs located in the region of the aileron, with a larger gap between the last rib of the aileron region and the tip rib of 242.8 mm. A total of six ribs are used in the tapered section of the wing. This means that a total of 16 ribs is obtained in the entire structure. Figure 7.4 illustrates the rib spacing previously discussed.
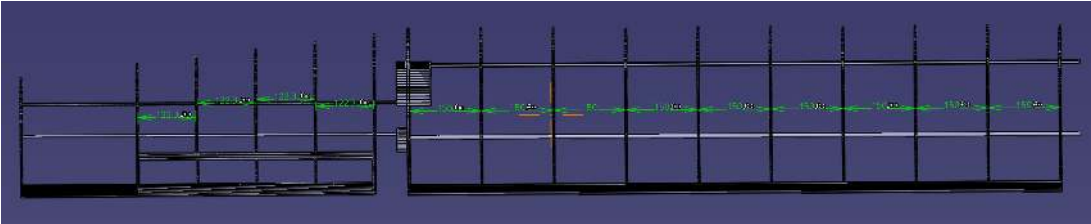
Figure 7.4: Rib distribution along the span of the wing.

A stiffening element is added near the trailing edge, as depicted in Figure 7.5. It is comprised of a carbon tube containing a hollow circular cross-section, with an outer diameter of 8 mm and inner diameter of 6 mm. The addition of this tube provides the structure with greater resistance to torsion. The material selected was carbon due to its high rigidity, with a Young's modulus of about 125 GPa [32], while maintaining a low weight. This weight is even lower considering that a hollow circular cross-section was selected. Similarly to what happens with the spar, this element goes up to the point where the first central panel of the wing ends. At that point, a different carbon tube, with a hollow circular cross-section with an outer diameter of 2 mm and inner diameter of 1.5 mm is used, connected to the main wing panel in a manner similar to what occurs with the secondary spar. It is also worth noting that, due to several constraints, this tube had to be placed above and to the left of the carbon tube of the main wing. In fact, due to the presence of the aileron, it was best to slightly move this secondary tube in the direction of the leading edge, in order to generate room not only for the aileron itself, but also to provide enough room for the installation of actuators and other electronics related to the aileron. It was moved upwards, in the direction of the upper surface of the wing as a consequence of the washout angle introduced in this tapered section. Since the tube is placed horizontally, similarly to the main one, if it had not been placed

upwards relatively to it, it would have not been able to go up to the wing tip. The geometrical centers of both tubes are separated by 7 mm in the horizontal coordinate and 3.95 mm in the vertical one.
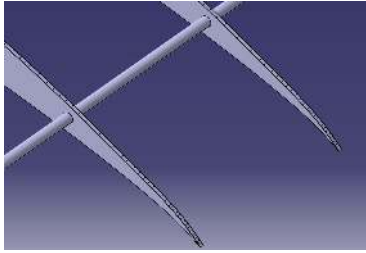
Figure 7.5: Carbon tube installed near the trailing edge.
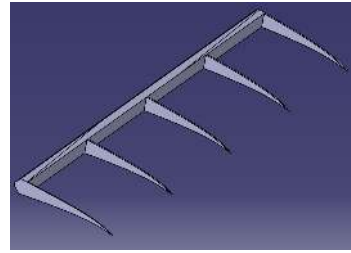
Figure 7.6: Aileron CAD model.

As for the aileron, different options were on the table. At first, a solid foam aileron was considered, with a balsa wood reinforcement at its leading edge, where the hinges that connect it to the main wing would be attached. This type of aileron would, despite being simpler to build, present some disadvantages, mainly due to its somewhat increased weight. As such, a structure more similar to that of the main wing was selected. This aileron, seen in Figure 7.6 is made entirely out of balsa wood, with ribs that, similarly to the ones of the main wing, may be reinforced with fiberglass for added stiffness. This aileron connects to a support beam, attached to the ribs of the main wing.

In order to provide the wing with its outer shape, a heat-shrinking cover is to be used. This cover should withstand the aerodynamic loads to which it will be subjected during normal operating conditions, while being extremely lightweight. However, applying it to the non-sheeted structure as it is at this moment would lead to it wrinkling at the leading and trailing edges, where the angles of curvature are greater. As such, a thin balsa wood cover is applied to the leading edge and tip of the trailing edge. Figure 7.7 shows a portion of this covers, mounted on the wing. This adds weight to the structure, but it is necessary to keep the cover well stretched, guaranteeing that the desired shape of the airfoil is maintained throughout the wing, thus assuring that the aerodynamic requirements are met. The structure becomes, then, a semi-sheeted one, with a hollow D-box.
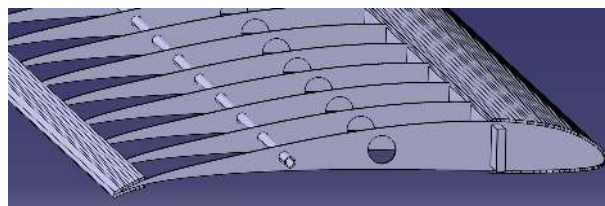
Figure 7.7: Aileron CAD model.

Based on this structure, a prototype will be build and statically tested. In the following chapter, the process of building the prototype will be described.

Chapter 8

Wing Prototype Building Process

In order to fulfill the goal of creating a finite element model that is adequate for a preliminary design process of the wing structure presented in the previous chapter, a prototype of the wing was built in order to be tested. Due to the size of the complete wing, a smaller, half-scale model of a portion of the wing was built. Throughout this chapter, the building process will be described, and considerations regarding the structural weight of each part made.

The portion of the wing to be modeled was chosen to be from the root to the 1 m point along the spanwise direction. A model with a 0.5 m span is then obtained, containing a total of six ribs. A scaled down CAD model of each of the structural parts of that portion of the wing was then produced, and a full assembly of the model obtained for the semi-sheeted wing structure, as shown in Figure 8.1.

8.1   Material Sourcing

The first task to undergo at this stage was the choice of the material source from where the parts were to be obtained.

Since the model required 1.5 mm thick ribs, two balsa sheets were bought, with the desired thickness and 20x100 cm dimensions.

As for the spar, a rectangular cross-sectioned beam, with a 3 mm width and 15 mm height was acquired. This beam was 1 m long. Since its cross section already has the desired shape, no further cuts need to be made, except for the one along the span in order to obtain the 500 mm long spar.

A carbon tube with a 2 mm outer diameter was also acquired, with a thickness of 0.5 mm. This tube also was 1 m long, and so had to be cut in half in order to obtain the desired length.

As for the fiberglass reinforcement, since it was to be applied to custom parts, instead of already produced plates, the individual components were acquired. As such, 49 g/m^2 fiberglass cloth, epoxy resin and hardener were bought.

(a) Scaled down spar.

(b) Scaled down rib.

(c) Scaled down carbon tube.

(d) Scaled down trailing edge cover.

(e) Scaled down leading edge tube.

(f) Scaled down assembly of the prototype.
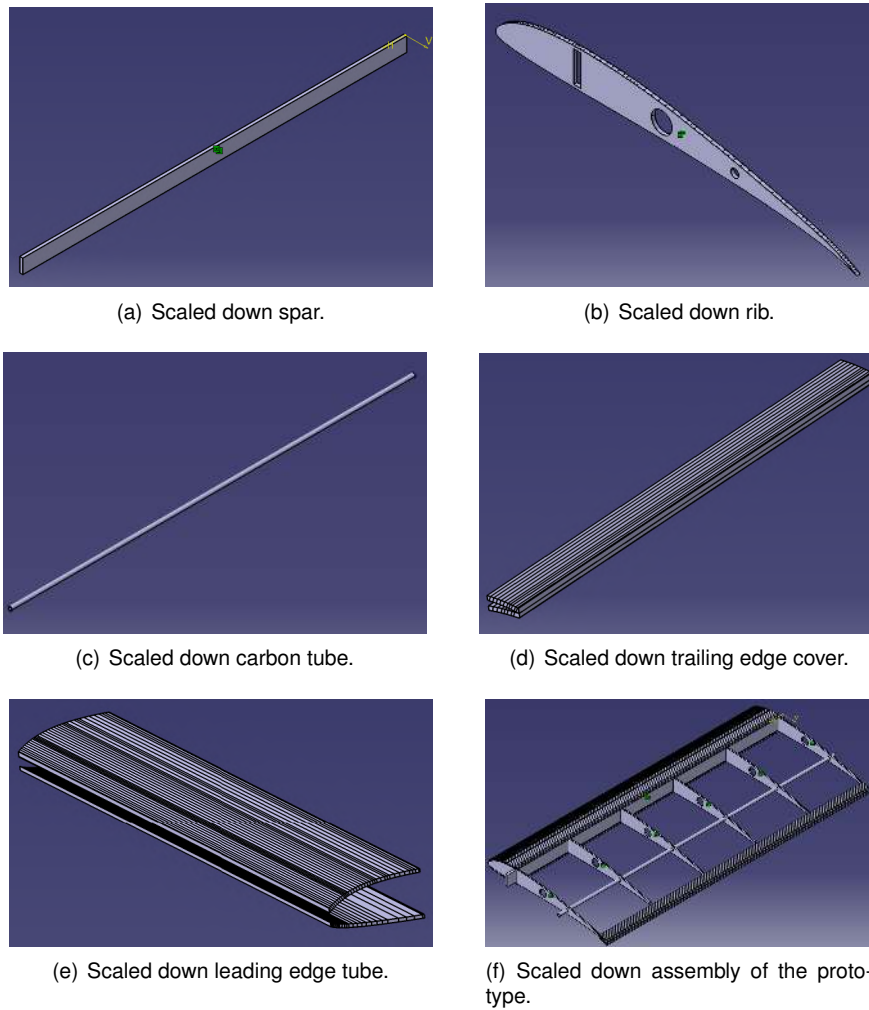
Figure 8.1: Scaled down CAD model of the prototype and its parts

8.2 Building Process

Regarding the building process, after performing the cuts on the balsa beam and the carbon tube, it was time to cut the ribs. Since the thickness of these parts is quite small, they were cut by hand, using drawings obtained from the CAD model as a guideline. These drawings were attached to the the balsa sheet, and the ribs cut using a snap-off blade. Special care was taken during this cutting process to the alignment of the balsa wood fibers, so as to obtain ribs where these fibers were preferentially parallel to the chord. By doing so, advantage is taken of the greater strength of this wood along this direction, as seen in Section 5.3.1. The hole where the spar attaches was cut using the same method, while the circular holes (the central one, for the passage of cables and reduction of structural weight, and the one near the trailing edge, where the carbon rod will be mounted) were carefully obtained using a driller. Figure 8.2 shows one of the built ribs. It is worth noting that, given the fact that all the ribs were hand made, small variations are to be expected as far as their shape is concerned, which will certainly constitute a difference between the physical prototype and the CAD model used to obtain the numerical model.

Figure 8.2: Balsa wood rib.

After cutting the ribs, the leading and trailing edge covers were produced. 1.5 mm thick balsa wood was also used. However, taking into account that these parts need to adequately fit the shape of the ribs, they had to be bent. A small gap had to be left in the regions where the angle of curvature is greater, in the tips of the leading and trailing edges, since it was not possible to bend the balsa as much without breaking it. As such, both in the leading and trailing edges, distinct covers for the upper and lower surfaces were cut. Using water to moisten the surface of the balsa wood where convex curvature should be present, the 4 parts were molded with the shape of the ribs and left to dry. Figure 8.3 illustrates one of the cut and bent trailing edge covers.

Figure 8.3: Balsa wood trailing edge cover.

All structural elements were then weighed using a digital scale with 0.01 g resolution. For the ribs, slight weight variations were registered between each part, and so an average value was determined. These structural weights can be seen in Table 8.1, together with an estimation based on the tabled density values of the materials and the volume of the parts.

Structural part	Real weight [g]	Estimated [g]	Deviation
Spar	4.06	4.50	9.78%
Rib (average weight)	0.35	0.57	38.90%
Carbon tube	4.24	4.12	2.9%
Leading edge cover (upper surface)	3.27	5.09	35%
Leading edge cover (lower surface)	3.03	4.63	34.56%
Trailing edge cover (upper surface)	1.21	1.39	12.95%
Trailing edge cover (lower surface)	1.21	1.39	12.95%

Table 8.1: Structural weight of the parts without fiberglass reinforcement.

After this first weighing process, it can be seen that, as expected, the ribs themselves are rather light. In fact, all the ribs together weigh in at 2.1 g, corresponding to 51.72% of the weight of the spar itself. Another interesting conclusion to be taken out of Table 8.1 is that even though the overall volume of the carbon tube is smaller than that of the balsa spar, it is moderately heavier. This shows the advantages, as far as weight is concerned, of using balsa wood for the majority of the parts of the wing structure.

Despite being light, the ribs in their current non-reinforced state did not show a satisfactory behavior, particularly as far as bending was concerned. In fact, the simple task of attaching them to the spar itself was cumbersome, with some of the breaking due to the force required to slide them along its span. This shows that simple balsa ribs may not be the most appropriate for the final model. Given this factor, and the remarks made in Chapter 7 regarding the eventual reduction on the overall number of ribs, a

fiberglass reinforcement was applied to them.

Regarding the difference between the real weight and the expected one for each part, it can be seen that the lowest discrepancy occurs for the carbon tube. This was somewhat expected, since the wood density present great variations, even within the same source.

In order to apply the fiberglass, pieces of the purchased fabric were cut, leaving an excess at the borders, and the ribs themselves prepared to receive the fibers. The inner cut surfaces were smoothed using sandpaper and the ribs cleaned to remove the small pieces of wood remaining from the cutting and sanding processes. A 50/50 mixture of epoxy and hardener was thoroughly mixed and applied evenly to one of the sides of the ribs. Special attention was payed to avoid the presence of air bubbles or zones with an excessive accumulation of resin, particularly in the regions near the edges of the inner cuts. After applying the resin, the fiberglass cloth was carefully placed, trying as much as possible to align the fibers in directions parallel and perpendicular to the chord. Once again, a special care was taken in order to avoid the presence of air bubbles or regions with an excess of resin. Sporadically, it was necessary to add small quantities of resin in order to guarantee a good binding between the fiber and the wooden rib. Figure 8.4 depicts a rib after being reinforced with the fiberglass composite.

Figure 8.4: Fiberglass composite reinforced rib.

After repeating this process for each rib, the same was done for the balsa spar, in order to stiffen it.

The resin was allowed to cure overnight for all parts. On the following day, the excesses of fiber were cut, and the process described before repeated for the other side of the parts. Once again, the resin cured overnight.

The excess fiber on the newly cured side was cut and the one covering the holes on the ribs removed. Using sandpaper, all the edges were sanded in order to feel smooth, and the parts cleaned. Finally, the parts were once again weighed. Since the carbon tube, leading and trailing edges covers remained unchanged, they were not weighed this time. Similarly to the last weighing process, the weight of the ribs presented fluctuations between each part, and so an average value was determined.

Structural part	Weight before reinforcement [g]	Weight after reinforcement [g]	Increase [g]
Spar	4.06	6.32	2.26
Rib (average weight)	0.35	0.97	0.62

Table 8.2: Structural weight of the parts after fiberglass reinforcement.

Comparing the values presented in Table 8.2 with those previously presented in Table 8.1, it can be seen that the addition of the epoxy based matrix and fiberglass reinforcement has a significant impact on the weight of each part. For the spar, an increase of 2.26 g is measured, corresponding to a weight increase of 55.67% relative to the original balsa-only spar. As for the ribs, an average increase of 0.62 g is measured, corresponding to a 177.14% increase on the part weight, when compared to the balsa-only rib. The impact on the complete prototype consists of an increase of 2.26 g and 3.72 g caused by

the reinforcement of the spar and ribs, respectively. If one were to make an approximation for the full scale complete wing, a total increase of approximately 20 g would be expected as a consequence of the reinforcement of the spars, while the reinforcement of the ribs would lead to an approximate increase of 40 g in the complete structure weight. It can then be seen that these values are relatively low when considering the structural benefits gained by applying that reinforcement.

Together with this increase in weight, a slight increase in thickness of each part is also noticeable. Using a caliper rule to measure the thickness of each part, a 0.3 mm increase was determined. Bearing in mind that a single layer of fiberglass reinforcement was applied per side, and assuming that the layers of both sides are equally thick, a 0.15 mm thickness for each layer of the reinforcement can be assumed. This is valid for both the ribs and the spar. It is worth considering, however, that it is not feasible to assure that this thickness is constant throughout each part. Once again, the limitations of a completely hand craft process will introduce differences between the prototype and the numerical model.

However, the overall stiffness of a part is not comparable before and after the fiberglass reinforcement, particularly as far as the ribs are concerned. After applying the resin and fiberglass, these show a significantly improved mechanical resistance to bending, being this difference specially noticeable in the direction perpendicular to the wood fibers, along which they easily fractured before. This was the intended result when the choice to apply the reinforcement was made.

8.3   Scale Wing Model Assembly

After having produced all the individual parts, it was only a matter of assembling the model. However, the rib holes where the spar was to pass through had to be enlarged, given the aforementioned increase in thickness of the spar due to the fiberglass reinforcement. This enlargement was achieved by further sanding the inner edges until the spar fitted the hole. The entire structure was then weighed, before the application of epoxy to permanently fix all parts together, yielding a total weight of 25.07 g.

Figure 8.5: Scale model.

Figure 8.5 shows the completed model, assembled together. The same epoxy resin used for the carbon fiber reinforcement was used on the contact surfaces between the several parts, and allowed to cure overnight, in order to guarantee an appropriate connection between them. A final weight of 26.44 g was registered.

At a later stage, a monokote cover was applied to the prototype, as seen in Figure 8.6, increasing its structural weight to a total of 41.34 g. It can then be seen that the influence of this cover in the structural weight is very significant, adding to the need of keeping the inner structure as light as possible in this type of projects.
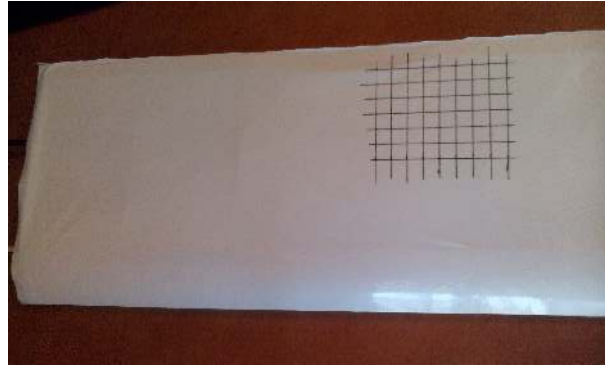
Figure 8.6: Heat-shrink film covered prototype.

Table 8.3 shows the weight of all parts used in the assembly, as well as the epoxy resin used to glue them together. A discrepancy of 0.03 g relative to the measured weight is recorded, due to the fact that an average weight was considered for the 6 ribs, and not the weight of each individual one.

Part	Weight[g]
Spar	6.32
Rib ($\times 6$)	0.97
Carbon tube	4.24
Leading edge cover (upper surface)	3.27
Leading edge cover (lower surface)	3.03
Trailing edge cover (upper surface)	1.21
Trailing edge cover (lower surface)	1.21
Heat-shrinking plastic	14.9
Epoxy used for assembly	1.37
Total	41.37

Table 8.3: Wing model break-up weights.

On the following chapter, a discussion of the tests carried out in the prototype will be made, and the results compared with those obtained by the finite elements analysis.

Chapter 9

Wing Prototype Testing

Having built the prototype, it was then possible to perform some experimental tests on it. Given the scope of the project, only static tests were carried out on the prototype. In this chapter, the testing procedure and the results obtained will be presented. Afterwards, the results obtained using the finite element model in CATIA® will also be discussed, and a comparison between both sets of data will be made.

9.1   Prototype Experimental Testing

Since the prototype built presents some limitations to the types of tests that can be carried out, given that only a portion of the wing and its internal structure is considered, simple static tests were performed.

Taking into account that the main goal of these tests is to acquire a set of data to be compared with the results obtained with the finite elements analysis carried out in CATIA®, for validation purposes, a simple loading case was considered. Using the support already described in Section 5.3.3, one end of the wing was fixed to it, and several loading cases were applied at the free end of the main spar. Between the support and the rib closest to it, a gap of 6 mm was present. This meant that the total span of the wing prototype tested was of 416 mm.

The testing procedure was very similar to the one applied to the carbon tube, as one can see in Figure 9.1. A ruler was used to mark the displacement of the bottom edge of the spar directly bellow where the load was being applied, and a caliper rule used to measure the distance between those marks and the original position.

Three loads were applied at a first stage, using combinations of 150 g weights. A fourth load was also considered, using the three weights and a bag filled with salt. All these loads were hung from the wing using fishing line, at a distance of 8 mm from the tip. Table 9.1 shows the displacements for each of the applied loads, measured at the lower surface of the spar, directly bellow the point where the force was applied.

It is worth pointing out that some degree of uncertainty is present in the measurements carried out, originating from the measurement devices used (an error of 0.25 mm, corresponding to half of the

75

Figure 9.1: Prototype testing.

Load [gf]	Displacement [mm]
150	7.30
300	14.60
450	22.30
548	26.40

Table 9.1: Displacement of the bottom edge of the spar at the point where the force is applied.

smallest division of the scale of the caliper rule, is expected) and from the procedure itself. In fact, a first set of data had been obtained, before realizing that the support had allowed for the prototype to move a few millimeters away from its original reference position. The data presented in Table 9.1 was recorded at a second stage, after performing some modifications on the support so that the wing prototype returned to its reference position after every load applied load was removed. Nevertheless, between each applied load, it was checked if the prototype returned to its reference position. This was confirmed for almost all cases, although a small discrepancy was registered between the last two loading cases, smaller, however, than the resolution of the caliper rule and thus considered of little relevance. These small errors will, however, have some influence when the comparison between these results and those of the FEA is made, further ahead.

In order to determine the influence of the heat-shrink cover on the behavior of the structure, a third set of tests was carried out, with the entire prototype covered. Before that cover was applied, however, a centimeter grid was added in order to determine how significant the effects of pre-tension added by the heat shrinking of the plastic during application are. Figure 8.6, presented in Section 8.3, shows that grid, drawn on the upper surface of heat shrink cover applied over the structure.

Checking the distances between the grid lines drawn on the cover after heat was applied, using a caliper rule, no apparent difference in the size of each cell was identified. This means that, even though some pre-tension effects are necessarily present due to the aforementioned shrinkage of the cover when heated, forcing it to remain stretched, they are not evident in this particular situation.

The four loads applied to the prototype when it was not covered were applied again, and the displacement caused on the wing registered. Table 9.2 shows the values of those displacements.

By comparing these values with those of Table 9.1, it is possible to conclude that, for the first two loading cases, no difference is identified. However, for the other two loading cases, a slight decrease in displacement is seen in the case where the cover was applied. This effect also becomes, although very

Load [gf]	Displacement [mm]
150	7.30
300	14.60
450	22.26
548	26.34

Table 9.2: Displacement of the bottom edge of the spar at the point where the force is applied(covered prototype).

slightly, more noticeable when a load of greater magnitude is applied. In fact, the difference between the uncovered and covered cases for the 450 g load is of 0.04 mm, compared to the 0.06 mm difference registered when the 548 g weight was used.

Based on these results, it can be assumed that the cover has some influence on the behavior of the structure. However, at this scale, and based on the tests carried out, that influence is rather small. For more complex loading scenarios, that influence should become more noticeable, since the presence of that cover alters the way on which forces act on the structure it covers, distributing them throughout the different parts in a way that does not occur for the uncovered structure.

9.2 Prototype Finite Element Analysis

Having performed the experimental tests on the prototype, the CAD model had to be changed in order to match the testing conditions. The span of the spar and carbon tube stiffening element were changed to 408 mm. This was done in order to apply the force at the edge of the modeled spar, thus eliminating the need of imposing a mesh point at the point where the force was applied. The elastic properties determined in Chapter 5 and validated in Chapter 6 were applied to each part. For the wooden parts, a local axis system was created so as to select an adequate orientation for the material properties, according to the direction of the wood fibers of each of those specific parts.

As for the connection between the several parts of the assembly, fastened connections were considered, as discussed in Section 4.1. The boundary conditions were then applied. One end was clamped while on the other the force under consideration was applied. Once again, the forces were obtained considering a value of gravitational acceleration of $g = 9.81 \ m/s^2$.

At this point, a convergence study was carried out. One of the applied forces was selected, and different meshes were applied to the parts. the displacement of the bottom edge of the spar, directly bellow where the force is applied was considered. The considered weight applied was the 450 g, which corresponds to a 4.41 N force acting in the vertical direction.

Since a high number of elements will be used in this analysis, given the amount of individual parts being meshed, instead of quadratic tetrahedron elements, linear tetrahedron elements are going to be used. By doing so, and taking into account that each linear element has six less nodes than the quadratic ones, as seen in Section 4.1, memory can be saved in the computation process, and a finer mesh can be achieved. A finer mesh is particularly important in this case, since rather thin parts are being considered, particularly the layers of composite.

Since several combinations of meshes were used for several parts, to be as synthetic as possible, only the most relevant aspects of each mesh, namely the element size and the sag parameters will be presented. These are the parameters that show a greater influence on the overall mesh, and thus no significant information will be lost to the reader.

	Mesh 1	Mesh 2	Mesh 3	Mesh 4
Global parameters for the mesh of the balsa rib				
Size	1.5 mm	1 mm	0.75 mm	0.75 mm
Absolute sag	1 mm	1 mm	0.5 mm	0.5 mm
Global parameters for the mesh of the composite reinforcement of the rib				
Size	1 mm	0.75 mm	0.5 mm	0.5 mm
Absolute sag	1 mm	1 mm	0.5 mm	0.5 mm
Global parameters for the mesh of the balsa spar				
Size	2 mm	1.5 mm	1 mm	1 mm
Absolute sag	5 mm	5 mm	5 mm	5 mm
Global parameters for the mesh of the composite reinforcement of the spar				
Size	1 mm	0.75 mm	0.5 mm	0.5 mm
Absolute sag	5 mm	5 mm	5 mm	5 mm
Global parameters for the mesh of the pultruded carbon tube				
Size	1.5 mm	1 mm	0.75 mm	0.75 mm
Absolute sag	1 mm	0.75 mm	0.5 mm	0.5 mm
Global parameters for the mesh of the balsa leading and trailing edge covers				
Size	2.5 mm	2 mm	1.5 mm	1 mm
Absolute sag	1.5 mm	1 mm	0.75 mm	0.75 mm
Total number of elements	428015	730269	1626517	1981926

Table 9.3: Global mesh parameters used in the to obtain the different meshes for each part.

In Table 9.3, the global mesh parameters used in each case can be observed. It is also worth noting that a great increase in the overall number of elements can be seen between all meshes. The influence of this refinement process can be easily seen by comparing Figures 9.2 and 9.3. The differences are particularly evident in the carbon tube and the spar. In fact, since these are the structural elements that, under the considered loading scenario, will be subjected to greater stresses and deformations, finer meshes such as 3 and 4 are better suited for the analysis. Note, also, that a greater number of elements per part makes it so that more nodes are being considered for the fastened connection between distinct parts, leading to more accurate results.

Focusing, at this stage, on the values of the maximum displacement obtained with each mesh, presented in Table 9.4, it can be seen that they are converging towards a value of 24.6 mm. Since there is no difference between the results obtained with mesh 3 or 4, mesh 3 will be considered for the analysis. Since this mesh has a lower number of elements than mesh 4, the computation time is, although not significantly, lower, and so using it is advantageous. It is worth noting that the computational times for
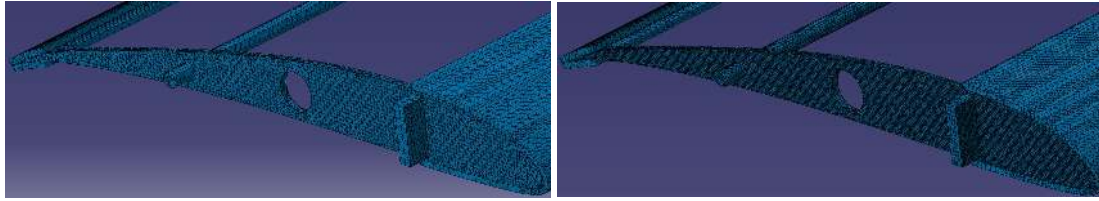
Figure 9.2: Detailed view of mesh 1 applied to the prototype.

Figure 9.3: Detailed view of mesh 3 applied to the prototype.

these last two meshes averaged 15 minutes, with a difference of about 1 minute between them.

	Mesh 1	Mesh 2	Mesh 3	Mesh 4
Maximum displacement [mm]	23	24.1	24.6	24.6

Table 9.4: Maximum displacement obtained with each mesh, for 450 gf loading case.

Having selected a mesh, conditions were met to carry out the analysis for all the applied loads, previously presented in Table 9.1. The resulting deformed shapes of the prototype are presented in Figure 9.4 and Figures A.1 through A.3, shown in Appendix A.
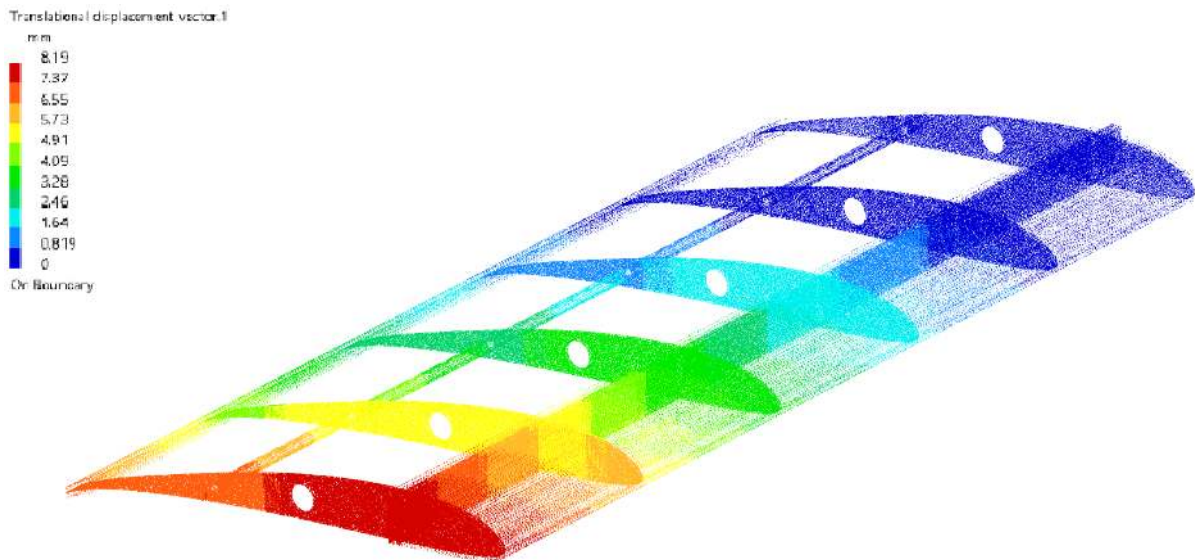

Figure 9.4: Deformation of the prototype under an applied load of 1.47 N.

It can be seen that the deformation of the wing prototype is consistent with the loading case. There can be identified both bending and torsion effects acting on the wing. This torsion effect is not, however, very significant, as one can see by looking at the values of the deformation in the rib closest to the point where the force is applied. In fact, regardless of the applied force, it is easily observable that the regions near the trailing edge of the wing are subjected to a slightly reduced vertical displacement, when compared to their leading edge counterparts. This torsion effect is particularly relevant after the third rib, counting from the clamped root. Given that a simple point loading is being applied, this phenomenon was expected. However, in an operational scenario, a distributed force would be applied over the entire chordwise coordinate, meaning that this torsion effect could be even less noticeable.

79

Comparing the value of the displacement of the lower edge of the spar, at the chordwise coordinate where the force is applied, obtained by the experimental test and the numerical model, it can be seen that there is a discrepancy in the results. Table 9.5 summarizes those results, presenting the relative difference between them.

Load [gf]	Load [N]	Displacement (physical test) [mm]	Displacement (finite elements analysis) [mm]	Relative difference
150	1.47	7.30	8.19	12.19%
300	2.94	14.60	16.40	12.33%
450	4.41	22.30	24.60	10.31%
548	5.38	26.40	29.90	13.26%

Table 9.5: Vertical displacement of the bottom edge of the spar at the point where the force is applied.

It can be seen that there are some discrepancies between the results of the numerical model and the ones measured with the experimental tests. These discrepancies are relatively uniform regardless of the weight applied to the wing. These differences must, however, be analyzed bearing in mind the sources of error described in Section 9.1 as far as the physical tests are concerned, as well as those introduced by the numerical model itself. These discrepancies and the sources motivating them will be discussed further ahead.

For all previous computations, it is also possible to determine the Von Mises stress distribution along the several parts of the wing prototype, to obtain further knowledge on potentially dangerous regions. The results are very similar for all the applied loads, differing between each other only in the values obtained for the stress, and not in where the maximum value for the stress is located, or in the overall distribution of stresses. Let the 548 gf loading case be considered as an example. Figure A.4, shown in Appendix A, presents the Von Mises stress distribution on the prototype. It can be seen that the highest values of the stress are present in the carbon tube, in the regions closer to the its clamped end, as well as near the clamped end of the spar. The remaining parts are not being subjected to significant stress, since this loading case does not particularly affect them.

A maximum value of 96.5 MPa is obtained, in the upper surface of the carbon tube, near its clamped end. This is particularly visible in Figure 9.5, which zooms in on the higher stress region. That value is, however, significantly lower than the 1.65 GPa tensile strength suggested by most manufacturers, indicating that this part in particular is well within its elastic domain. Looking at that same image, it can also be seen that the composite reinforcement layers near the root are the regions of the spar under a greater stress, of about 48 MPa, showing that they are fulfilling their mission and providing the structure with increased stiffness.

Looking now at Figure 9.6, by adjusting the scale of the color scheme used to represent the stress, a better representation of the Von Mises stress distribution in the tip rib is achieved. The stress concentration near the edges where the rib connects to both the spar and the carbon tube is now visible, and also near the trailing edge, where its surface area is lower and the cover is attached. The location of these values was expected, since, under the loading conditions, the ribs are responsible for the transmission
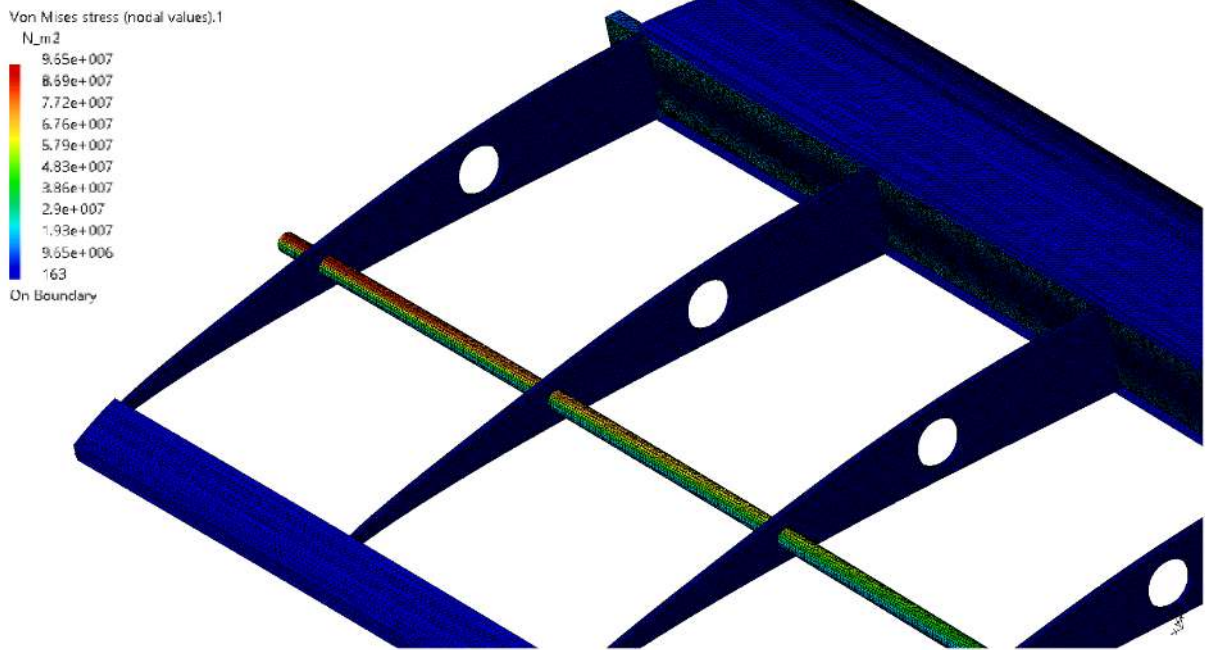
Figure 9.5: Von Mises stress distribution on the prototype under an applied load of 5.38 N (detail of the higher stress region).
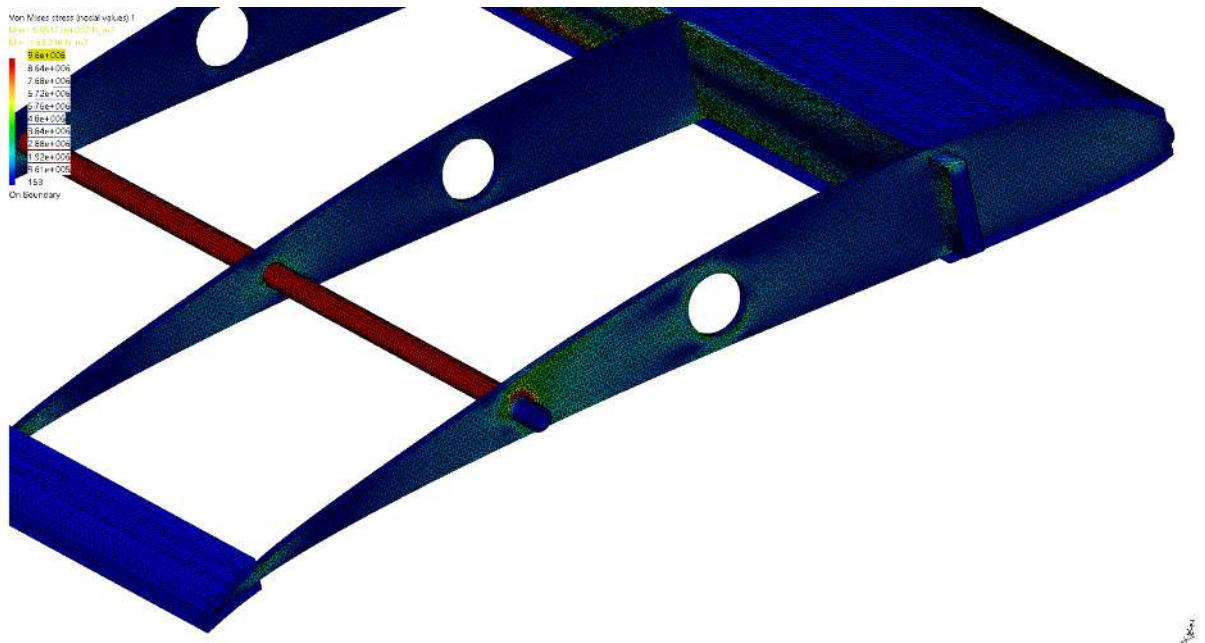

Figure 9.6: Von Mises stress distribution on the prototype under an applied load of 5.38 N (detail of the free end, with a different scale).

of the force from the spar to the remaining structure, namely the carbon tube. Higher values of the Von Mises stress can also be observed near the central hole of the rib, since like any discontinuity in a surface, it acts as a stress concentration feature. These values of stress are, however, significantly lower than the ones identified previously in the carbon tube, in the order of 4.8 MPa and act primarily on the layer of fiberglass composite added for reinforcement, as intended for this design.

Having compared the results for the uncovered structure, an attempt was made at modeling the heat-shrink cover and performing a finite elements analysis on it. Being the cover essentially a membrane under pre-tension, a surface was modeled and a two dimensional mesh applied to it. However, it proved impossible to apply pre-tension to that modeled surface. Furthermore, even without applying pre-tension, errors occurred when meshing the parts. These errors resulted from limitations of the software package when trying to merge the nodes of the 2D elements of the cover model and the 3D ones of the remaining parts. Considering, also, that the cover is extremely thin, modeling it as a 3 dimensional part would introduce a significant degree of uncertainty in the analysis. As such, no comparison could be made regarding those results.

9.3   Discussion of the results

Given the different results yielded by the experimental and the numerical models, a discussion of why those discrepancies were found is justified.

The first identifiable source of error as far as the numerical model is concerned is related to the material properties. In the particular case of the balsa, for instance, a certain degree of variation is expected between different specimens of wood. Since in this case the wood used for the various parts of the physical prototype came from two different sheets, it cannot be guaranteed that the properties that were validated in Section 6.1 apply equally to all the parts. Besides, it is also assumed in this model that the fibers of the ribs are all aligned in the same direction. This assumption constitutes a simplification of the model in itself. In reality, it is not feasible to obtain a piece of wood whose fibers are all perfectly aligned, meaning that, besides the eventual difference in orientation between different parts, even within the same part a slight variation of the orientation of the fibers is present.

Another aspect to consider is the simplification previously made of considering the composite used for the reinforcement of some balsa parts to be perfectly isotropic. This assumption, even though valid for some cases, as proved in Section 6.3, may not entirely apply under the bending and torsion conditions to which the prototype is subjected.

Still regarding the composite reinforcement, it was also assumed that the thickness of the layer added is constant throughout the entirety of the parts. It is not feasible to prove this in reality, since those reinforcement layers were hand made. Given that situation, a degree of uncertainty is introduced in the numerical model.

Finally, it is also relevant to consider that the connections between the parts were modeled assuming fastened connection properties, meaning that they were assumed to be perfectly bonded, originating a single rigid body. However, in the experimental model, epoxy resin was used to assemble the several

parts. This resin alone has its own elastic properties, and it too deforms according to the loading scenario applied to the prototype. Also, it cannot be guaranteed that those connections between parts are entirely filled with resin. Some gaps between parts can exist, which also goes against the perfect connection between parts of the numerical models introduced by the merging of nodes. Bearing this in mind, some degree of error is expected when performing the analysis on the assembled prototype.

Taking into consideration all these sources of error, it is understandable that the numerical model is not entirely accurate when predicting the behavior of the wing prototype. However, it is also important to remember that the calculated "relative differences" presented in Table 9.5 use as a reference value the displacement measured during the experimental test, which also includes a degree of uncertainty, as previously discussed. Considering an average calculated using the four sets of data, a relative error of 12% is obtained. Even though this value may already be considered relevant, given all the considered simplifications, it can be accepted that this numerical model may be used for a preliminary prediction of the behavior of the structure.

To an extent, the slight differences between the experimental and the numerical models presented previously prevent the simulation from being more accurate. Since the prototype was entirely hand built, it is impossible to produce two equal parts. Furthermore, considering the limitations imposed by working with orthotropic materials such as wood, whose properties are not constant throughout, these difficulties become even more evident. In this type of situations, a numerical model has a very slim chance of perfectly describing the behavior of its physical counterpart.

If a more controlled building process was put in place, using methods that minimized the uncertainty introduced by a completely hand made procedure, the produced parts would be more homogeneous as far as their properties are concerned, leading to a better match between them and their CAD modeled counterparts. For example, if the ribs were laser cut, their outer shape would be perfectly equal for all of them, and it would even be possible to devise a way to guarantee that the fiber alignment would remain constant throughout all parts. This would make it so that, since the fibers in the numerical model are perfectly aligned according to a set axis system, the actual alignment of the fibers in the experimental model would be more coherent with that of the numerical one.

If instead of applying the fiberglass reinforcement by means of a hand lay-up process, a vacuum had been used, an almost homogeneous thickness of the reinforcement composite layer could be guaranteed. In fact, since the fiberglass composite reinforcement is, as intended and previously confirmed by the analysis of the Von Mises stress distribution on the prototype, responsible for adding stiffness to the structure, a variation in thickness at some regions leads to differences in results.

All the aforementioned techniques would contribute towards a more controlled building process, leading to a better, more homogeneous final prototype. As previously discussed, this would contribute greatly to reduce the degree of uncertainty present in the numerical model, and far more accurate results would be obtained from it. However, given the limitations in the size of the parts, as well as the available materials, those processes could not be used.

Chapter 10

Conclusions

10.1 Achievements

The main objective of this thesis was to, based on a new design for the LEEUAV wing, produce a prototype and obtain a numerical model that predicts its behavior.

After an identification of the UAV characteristics and aerodynamic loads acting on the wing, the first major step was to identify the materials that would be used in the structure and determine their elastic properties. The recommendations presented by [27] and detailed in ASTM Standard D143-94 [30] for the testing of wooden specimens were studied. The orthotropic nature of wood made it so that several test are recommended, for the elastic properties in each direction. It was later concluded that, given the available sources of balsa wood, the specimens for some of the tests could not be obtained, limiting the number of tests to the tension parallel to the grain tension test. A conventional tension test using a clip gauge was carried out using a slightly modified specimen, produced for this purpose, but maintaining the testing region in accordance to ASTM recommendations. The longitudinal Young's Modulus was determined, and the remaining elastic properties obtained using the relations presented in [28]. As far as the carbon tube is concerned, a bending test was performed, and, assuming it to be isotropic, the Young's modulus determined. Finally, concerning the fiberglass composite, ASTM recommendations [34] were followed for building and testing a specimen, and its elastic properties determined. It was found that all the determined values for the several properties were approximate to the tabled ones for each material.

All those tests were then simulated in CATIA®, in order to validate the results. For the balsa wood and carbon tube tests, it was found that the determined properties were accurately describing the behavior of the material, with negligible values for the relative error between experimental and numerical results. As far as the fiberglass composite is concerned, an assumption of two dimensional isotropic behavior was made at first, and an almost negligible difference between the physical and FEA results found. It was also proved that if 3D isotropy was considered, assuming that a very thin part being analyzed, a very small discrepancy between results is obtained.

A more detailed description of the wing structure on which the prototype was based was then pre-

sented. Composite reinforcement was found to be a valid way of adding stiffness to the parts, allowing for a reduced number of ribs to be used, in an attempt to obtain a lighter structure.

Based on the new wing structure, the prototype was built. The building process was outlined. It was determined that the inclusion of the composite reinforcement was not only adequate, but necessary. An analysis on the influence of the addition of that composite reinforcement on the weight of the parts was made. It was seen that it had a greater impact on the ribs than it had on the spar, particularly in terms of weight addition. The structural weight of all parts and of the assembled prototype was determined, and it was found that the monokote cover had the greatest impact on the overall structural weight.

Static tests were then performed on the prototype, and their results compared with the ones obtained by the FEA carried out in CATIA®. It was determined that those results were not in complete agreement, given the small discrepancies, of about 12%, identified between the experimental prototype and its numerical model. Despite those differences, the disparity in results is not high enough to prevent a preliminary analysis of the structure. By analyzing the Von Mises stress distribution yielded by that FEA, it was confirmed that the prototype could safely support the loading scenarios to which it was subjected, without danger of any of its parts coming close to plastic deformation. It was also seen that the composite reinforcement was completing its task, withstanding the imposed forces and thus alleviating the stress felt on the balsa parts.

Finally, it was concluded that a more controlled building process, where the human factor is somewhat reduced, would allow one to obtain parts whose properties are significantly more consistent, leading to a reduction in the uncertainty on the results of the FEA, when compared to those obtained by the experimental tests.

10.2   Future Work

Towards the final part of this work, some of the limitations of CATIA®'s Generative Structural Analysis workbench became more obvious and somewhat limited the conclusions that could be drawn, since it was not possible to adequately model the wing cover and apply the estimated aerodynamic loads determined in the initial chapters of this document. As such, it would be interesting to perform this task using a different software package, one that provides better tools that could allow for the completion of that task. A complete transition to that new software would have to be made, beginning at the validation of the material properties, so as to maintain a coherent approach and obtain a robust numerical model.

It would also be interesting to build a prototype of the complete wing. This task would, nevertheless, require the previously presented one to be carried out first, since based on the results of that analysis, it could be determined whether the structural design suggested in this document fully satisfied the requirements set for the LEEUAV.

If a prototype of the wing was built, it would also be relevant to perform a set of wind tunnel tests in order not only to accurately determine the structural behavior of the wing when subjected to conditions more similar to those it would face when in operation, but also to determine the influence of the washout angle introduced in this new structure.

Bibliography

[1] A. C. Marta and P. V. Gamboa. Long endurance electric uav for civilian surveillance missions. In *29th Congress of the International Council of the Aeronautical Sciences*, St. Petersburg, Russia, September 2014. ICAS.

[2] Nuno M. A. Silva. Parametric Design, Aerodynamic Analysis and Optimization of a Solar Powered UAV. Master's thesis, Instituto Superior Técnico, 2014.

[3] FreeCAD manual. http://www.freecadweb.org/wiki/index.php?title=manual, Accessed in April 2015.

[4] CD-adapco^{TM}. http://www.cd-adapco.com/products/star-ccm2015.

[5] F. R. Menter. Improved two-equation k-omega turbulence models for aerodynamic flows. *NASA STI/Recon Technical Report N*, 93:22809, October 1992.

[6] P. Malan, K. Suluksna, and E. Juntasaro. Calibrating the γ-re_θ transition model for commercial cfd. In *47th AIAA Aerospace Sciences Meeting*, St. Petersburg, Russia, October 2008. AIAA.

[7] P. R. Spalart and S. R. Allmaras. A one-equation turbulence model for aerodynamic flows. *AIAA*, 1992.

[8] NING Fang-Fei XU Li-Ping. Application of one-equation spalart-allmaras turbulence model in the numerical simulation of internal flows. *Journal of Engineering Thermophysics*, 3:012, 2001.

[9] Thomas C. Corke. *Design of Aircraft*. Pearson Education, Inc., 2003. ISBN:0130892343.

[10] T. H. G. Megson. *Aircraft Structures for Engineering Students*. Elsevier, 2012. ISBN:978-0-08-096905-3.

[11] O. Schrenk. A Simple Approximation Method For Obtaining The Spanwise Lift Distribution. *Luftwissen*, 7(4):1–10, 1940. also NACA Technical Memorandum N.948.

[12] Airfield Models. http://www.airfieldmodels.com/index.html, Accessed in April 2015.

[13] Guillows Model Builders. http://balsamodels.com/phpbb/viewtopic.php?p=6713, Accessed in April 2015.

[14] RC groups. http://www.rcgroups.com/forums/showthread.php?t=580924, Accessed in April 2015.

[15] SolidWorks. http://www.solidworks.com/, Accessed in April 2015.

[16] Dassault Systemes Catia. http://www.3ds.com/products-services/catia, Accessed in April 2015.

[17] Siemens NX. http://www.plm.automation.siemens.com/en_us/products/nx/, Accessed in April 2015.

[18] J. N. Reddy. *An Introduction to the Finite Element Method*. McGraw-Hill, 2006. ISBN:007-124473-5.

[19] G. Dhatt, G. Touzot, and E. Lefrançois. *Finite Element Method*. John Wiley & Sons, Inc, 2012. ISBN:978-1-84821-368-5.

[20] CATIA® mesh tutorial. http://catiadoc.free.fr/online/cfyuganalysis_c2/cfyuganalysis3dmeshpart.htm, Accessed in May 2015.

[21] D. Roylance. Constitutive equations. October 2000.

[22] J. N. Reddy. *Mechanics of laminated composite plates and shells: theory and analysis*. CRC press, 2004. ISBN:0-8493-1592-1.

[23] F. Beer, E. Johnston, J. Dewolf, and D. Mazurek. *Mechanics of Materials*. McGraw-Hill, 2012. ISBN:978-0-07-338028-5.

[24] R. Schleicher and J. Barr. *Building And Flying Model Aircraft*. Dover Publications, Inc., 1988. ISBN:0-486-25801.

[25] L. H. Meyer. *Plywood - What it is - What it does*. McGraw Hill, 1947.

[26] S. Record. The Mechanical Properties of Wood Including a Discussion of the Factors Affecting the Mechanical Properties, and Methods of Timber Testing. July 1914.

[27] L. J. Markwardt and W. J. Youngquist. Tension test methods for wood, wood-base materials, and sandwich constructions. *United States Department of Agriculture Forest Service*, (2055), June 1956.

[28] Kretschmann, D. Mechanical Properties of Wood. Technical Report General Technical Report FPL–GTR–190, 1999.

[29] N. Andrew, H. Philip, and P. Noel. Determination of wood strength properties through standard test procedures. In *Proceedings of the 10th International Conference on Manufacturing Research ICMR 2012*, pages 372 – 377, School of Computing, Engineering and Information Sciences, Northumbria University, Ellison Building Newcastle Upon Tyne, NE1 8ST, UK, 2012.

[30] ASTM. D143-94 - Standard Test Methods for Small Clear Specimens of Timber. 1994.

[31] F. Hild and S. Roux. Digital Image Correlation: from Displacement Measurement to Identification of Elastic Properties – a Review. *Strain*, 42(7):69–80, 2006. DOI: 10.1111/j.1475-1305.2006.00258.x.

[32] GW composites. http://gwcomposites.com/carbon-tubes/, Accessed in June 2015.

[33] ASTM. D3039 - Standard Test Method for Tensile Properties of Polymer Matrix Composite Materials. 2000.

[34] Intertek: Tensile Testing Composite ASTM D3039. http://www.intertek.com/polymers/tensile-testing/matrix-composite/, Accessed in June 2015.

Appendix A

Analysis Images

Here are presented the results of the FEA carried out in chapter 9 that were not shown previously.

Figures A.1 through A.3 show the displacement obtained for each applied load.

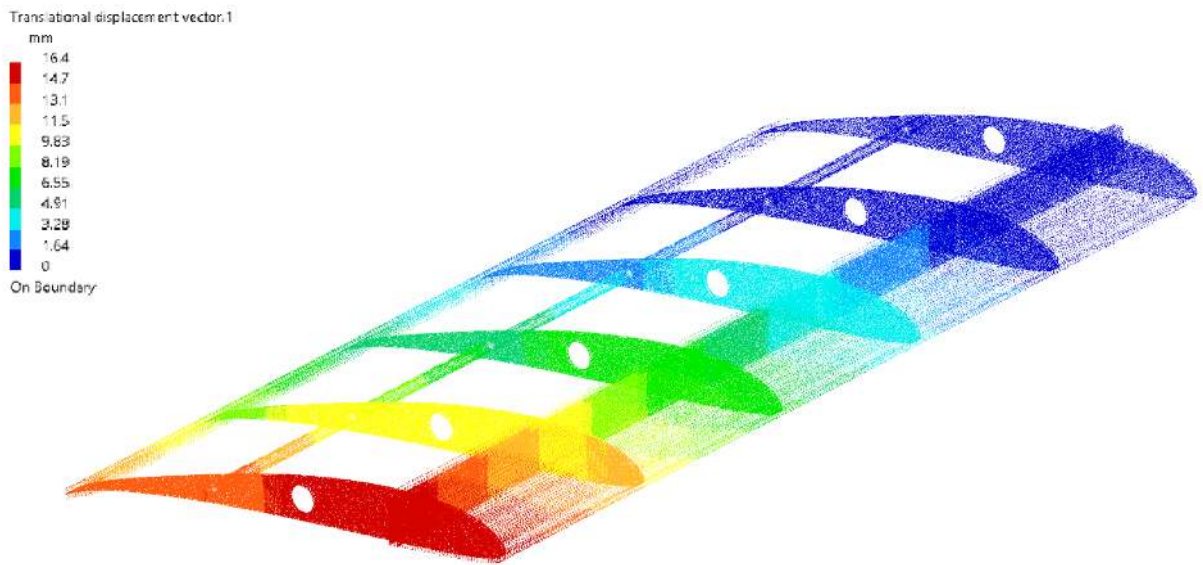Figure A.4 shows the Von-Mises stress distribution in the structure, for an applied load of 5.38 N.

Figure A.1: Deformation of the prototype under an applied load of 2.94 N.
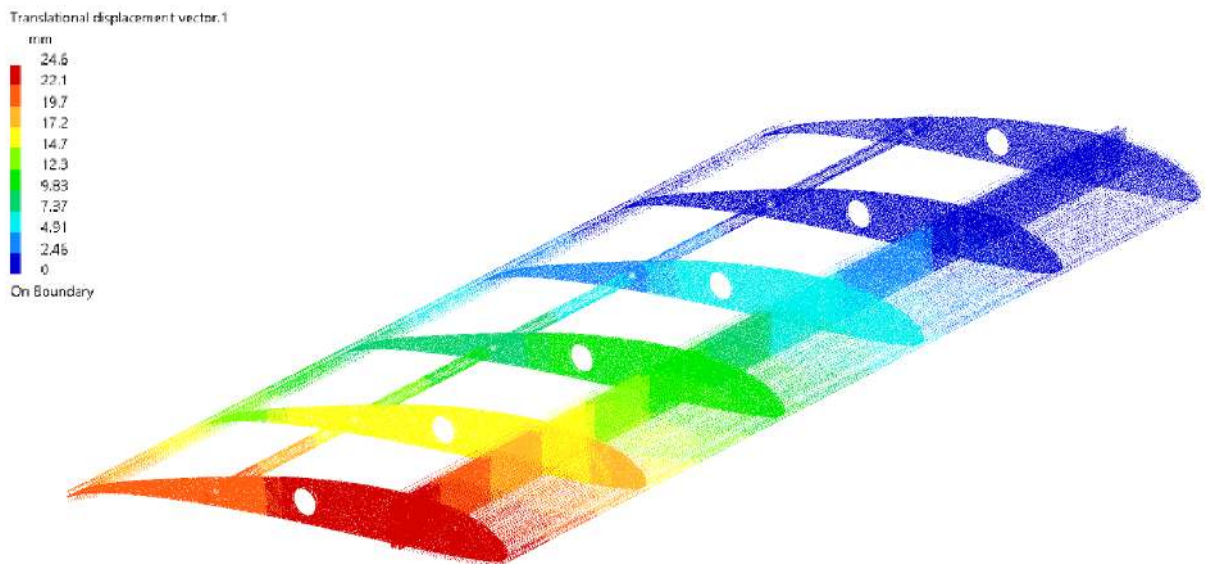

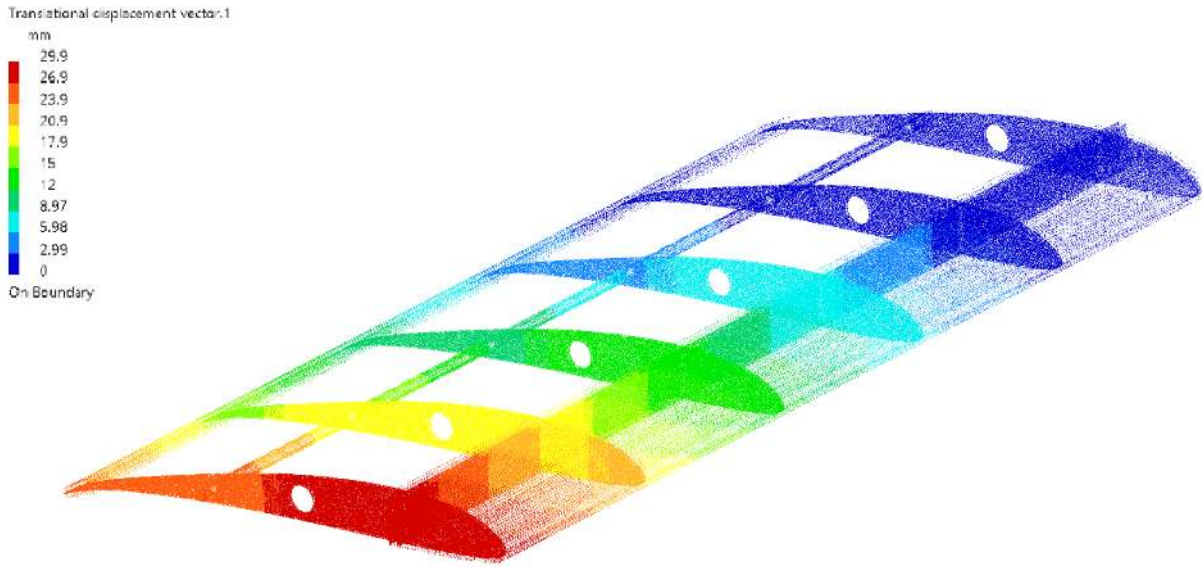Figure A.2: Deformation of the prototype under an applied load of 4.41 N.

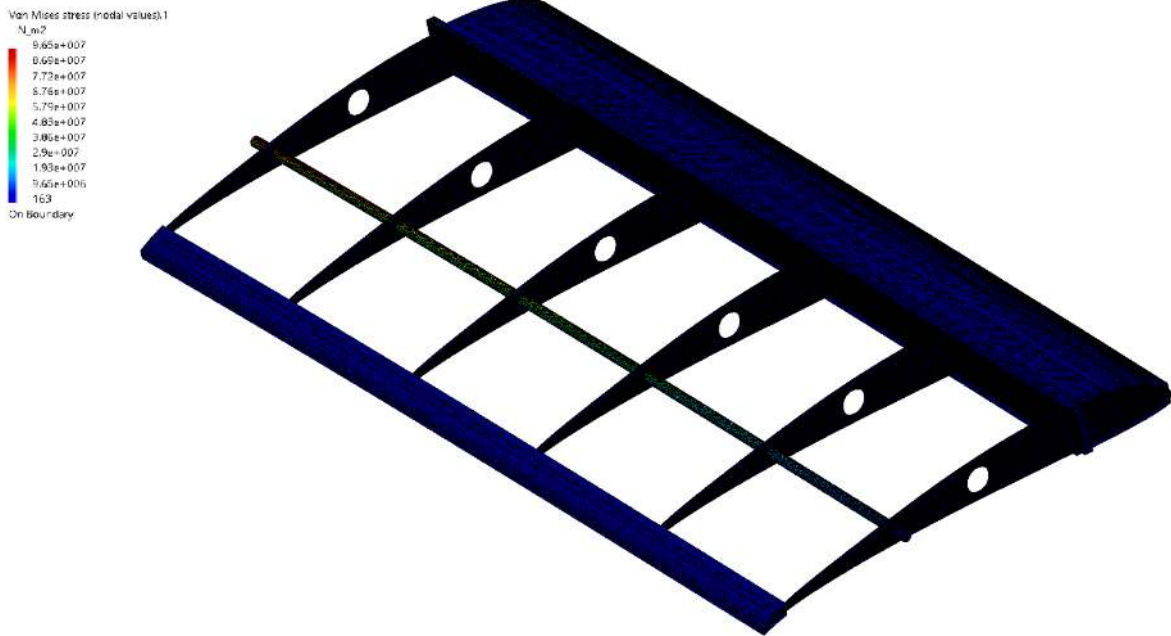Figure A.3: Deformation of the prototype under an applied load of 5.38 N.

Figure A.4: Von Mises stress distribution on the prototype under an applied load of 5.38 N.